

**Resolution Characterization and Nanofabrication
for Soft X-ray Zone Plate Microscopy**

by

Weilun Chao

B.S. (State University of New York at Stony Brook) 1999
B.Eng. (State University of New York at Stony Brook) 1999

A dissertation submitted in partial satisfaction of the
requirements for the degree of
Doctor of Philosophy

in

Engineering-Electrical Engineering and Computer Sciences

in the

GRADUATE DIVISION

of the

UNIVERSITY of CALIFORNIA, BERKELEY

Committee in charge:

Professor David Attwood, Chair
Dr. Erik H. Anderson
Professor Raymond Y. Chiao
Professor Andrew Neureuther

Spring 2005

Resolution Characterization and Nanofabrication
for Soft X-ray Zone Plate Microscopy

Copyright © 2005

by

Weilun Chao

Abstract

Resolution Characterization and Nanofabrication for Soft X-ray Zone Plate Microscopy

by

Weilun Chao

Doctor of Philosophy in Engineering - Electrical Engineering and Computer Sciences

University of California, Berkeley

Professor David Attwood, Chair

Soft x-ray microcopy is a valuable nano-imaging technique in a wide variety of scientific disciplines. It complements other nano-imaging techniques, such as electron and scanning probe microscopy, by offering a unique set of capabilities including elemental and chemical specificity, magnetization sensitivity, as well as in-situ imaging with applied fields, overcoatings, and wet environments. By combining these advantages with high spatial resolution, the full-field transmission microscope, XM-1, operating at wavelengths in the 1 nm to 3 nm range, has yielded valuable knowledge in many areas of the physical and life sciences. A key to optimizing its performance for nanoscale studies is quantitatively determining and maximizing the spatial resolution. In this dissertation, new methods are demonstrated which permit accurate characterization and significant improvement of the spatial resolution. Based on both theoretical and experimental studies of the existing measurement techniques (using test objects such as knife edge, e-beam fabricated test structures, etc.), a new technique that uses multilayer coatings in cross section has been developed, which was shown to provide a more accurate means in

quantifying resolution. By imaging this multilayer test object, systematic measurement of the microscope's modulation response as a function of feature periods is demonstrated. The measurement results show that, for the microscope with an objective micro zone plate fabricated using conventional single exposure electron beam lithography, the resolution is near-diffraction-limited at 20 nm. This resolution is limited by the smallest zone width of the micro zone plate, which was limited by the electron beam lithography used for fabricating the zone plate. To obtain better resolution, a new overlay nanofabrication technique has been developed by the nanofabrication team at Lawrence Berkeley National Laboratory (LBNL). This technique, based on sequential fabrication of alternating zone structures, significantly reduces the smallest feature sizes e-beam lithography is capable of fabricating in dense patterns. Using this technique with the LBNL's Nanowriter electron beam writer, zone plates of 15 nm outermost zone width have been fabricated for the first time, with excellent zone placement accuracy of 1.7 nm. Characterization of the microscope using the multilayer test object indicates that sub-15 nm spatial resolution has been achieved with these zone plates.

Table of Contents

Acknowledgements	iv
Chapter 1. Introduction: Soft X-Ray Microscopy	
1.1 Motivation of Soft X-Ray Microscopy	1
1.2 Imaging Optics for X-Rays	5
1.3 Soft X-Ray Microscopes Based on Fresnel Zone Plate Lenses	11
1.3.1 Full-field Transmission Soft X-Ray Microscopes	12
1.3.2 Scanning Transmission Soft X-Ray Microscopes	14
1.4 Overview	16
Chapter 2. Soft X-Ray Microscope XM-1 and Fresnel Zone Plate	
2.1 Overview	18
2.2 Capabilities and Applications of the Soft X-Ray Microscope XM-1	18
2.3 Design of the Transmission Soft X-Ray Microscope XM-1	24
2.4 Fresnel Zone Plates	28
2.5 Zone plate Fabrication with the Nanowriter Electron Beam Lithography System	34
2.6 Conclusion	44
Chapter 3. Theory of Image Formation and Partial Coherence	
3.1 Introduction	45
3.2 Spatial Coherence in Imaging	45
3.3 Image Formation with Partially Coherent Illumination	52
3.4 Mutual Intensity in the Object Plane with Critical Illumination and van Cittert-Zernike Theorem	55

3.5 Image Formation in the Spatial Frequency Domain and Transmission Cross Coefficient	61
3.6 Degree of Partial Coherence	67
3.7 Modulation Response and Resolution of the Microscope	70
3.7.1 Periodic Lines and Spaces	71
3.7.2 “Knife Edge”	73
3.8 Conclusion	77

Chapter 4. Test Objects for Resolution Measurement

4.1 Introduction	79
4.2 Test objects and specifications	79
4.3 Test Object designs and fabrication	80
4.3.1 Dense test objects with discrete feature sizes using electron beam fabrication	81
4.3.2 Multilayer test objects	84
4.3.3 A test object possessing a broad, continuous spatial frequency range: Knife edge	89
4.3.4 Gold “islands” as test objects	91
4.4 Conclusion	93

Chapter 5. XM-1 Microscope Resolution Measurement

5.1 Introduction	94
5.2 Resolution measurement of a 35 nm micro zone plates using knife edge test objects	95
5.3 Qualification of micro zone plates with 25 nm outer zone width using gold-island objects	99
5.4 XM-1 Resolution measurement with line test patterns	104
5.5 Resolution measurement using multilayer test objects	110
5.6 Conclusion	115

Chapter 6. Breakthrough in Resolution using New Overlay Nanofabrication Technique

6.1 Introduction	117
6.2 Micro zone plate improvement: challenges for fabrication of high-resolution zone plates	118
6.3 Solution for the fabrication challenges: overlay nanofabrication technique	120
6.4 Fabrication of 15 nm micro zone plates using the overlay nanofabrication technique	122
6.5 The first ever 15 nm zone plates	126
6.6 Condenser zone plate with 40 nm zone widths	127
6.7 Testing with multilayer test objects	128
6.8 Conclusions	132

Chapter 7. Conclusions

References

Appendix A. The Mutual Intensity of Broadband Illumination in the Object Plane

Appendix B. Zone Plate and Test Object Fabrication Processes

B.1 Micro zone plate fabrication	157
B.2 Condenser zone plate fabrication	166
B.3 Test object fabrication	174

Appendix C. Knife Edge Intensity Ranges for Resolution Measurement

Acknowledgements

First and foremost, I would like to express my deepest gratitude and appreciation to my advisor/mentor, Professor David Attwood. I benefited not only from his tremendous depth of knowledge in many sciences, but also from his kindness of sharing this valuable knowledge. His guidance and support throughout my graduate career made this dissertation fruitful. His determination, enthusiasm for science, and kindness to others sets me an excellent example of a scientist.

I would also like to thank Professor Andrew Neureuther and Professor Raymond Chiao for serving on my thesis committee. I would also like to thank Dr. Erik Anderson, who in addition to serve on my thesis committee, share numerous insights on zone plate fabrication and image analysis.

None of this work could be possible without the guidance and support from the XM-1 microscope team, and of the CXRO's nanofabrication team: Gregory Denbeaux and Angelic Pearson; Deirdre Olynick, Bruce Harterneck, J. Alexander Liddle and Farhad Salmassi. In particular, I would like to thank Deirdre Olynick for her kind words and continuous support in my graduate career, and to Bruce Harteneck and J. Alexander Liddle for their novel idea of the overlay fabrication technique.

I would also like to thank my parents for providing me such a valuable opportunity for studying in the United States, allowing me to fulfill my dream. I would

also like to thank Sandra Yu and my sister for their encouragement and support throughout my graduate studies.

Last but not least, I would like to thank Kristine Rosfjord, Anne Sakdinawat, Chang Chang, Yanwei Liu, Göran Johansson, Andrew Aquila, Holly Barth and Ryan Miyakawa for their significant contributions in enhancing my graduate school experience.

Chapter 1

Introduction: Soft X-ray Microscopy

1.1 Motivation of Soft X-Ray Microscopy

Nanoscience and nanotechnology require analytic tools with spatial resolution at the nanoscale. For many studies in the life and physical sciences it is desirable, if not critical, that these tools also permit elemental and chemical identification, on a spatial scale of order 10 nm or better. In-situ studies in various environments are also often desired. One of the commonly used nano-analytic tools is electron microscopy (transmission (TEM), scanning (SEM) and their variances). These microscopes provide spatial resolutions from a few nanometers to a few angstroms. For transmission electron microscopes, the samples must be thinned to thicknesses of 100 to 200 nm, depending on the resolution to be achieved. Special sample preparations are required to obtain such thicknesses. In addition, high vacuum requirements and permissible sample environments, such as no external magnetic fields and no overcoating, impose restrictions making many studies impossible to conduct. Scanning probe microscopes, such as STM, AFM and MFM, a second class of commonly utilized nano-analytic tools, permit acquisition of topographic information with angstrom level spatial resolution in both lateral and vertical (height) directions. These techniques, however, impose restrictions on the permissible sample environments (such as no external magnetic field in magnetic force microscopes) and conditions (e.g. no overcoatings), limiting the applicability of the microscopy to many scientific studies. Neither electron or scanning probe microscopies

provide direct elemental or chemical sensitivity, nor do they provide orientation (polarization) sensitivity.

Some of the desirable capabilities lacked by the two techniques above can be found in visible and ultraviolet light microscopy. This commonly available imaging technique permits thick samples (tens to hundreds of microns) and a wide variety of sample conditions. Visible light/UV microscopy, however, has relatively poor spatial resolution, typically of order 200 nm, due to the wavelengths, of 250 to 650 nm, and thus is inadequate for truly nanoscale studies. As resolution is proportional to the wavelength (λ) divided by numerical aperture (NA) of the imaging optics ($\text{Res} \propto \lambda/\text{NA}$), reduction of the wavelength offers a natural path to improved resolution. High energy x-rays, commonly known as “hard x-rays,” with wavelengths of a few angstrom or less [Fig. 1-1], offers very short wavelengths, but unfortunately achieve resolution similar to that of visible light microscopy, due to the limitations of available x-ray optics technologies. For hard x-rays the small numerical aperture of available optics, and insufficient optical quality, undercut the benefit of the short wavelength. X-rays of lower energy, known as “soft x-rays,” which have wavelengths from a few nanometers to a few angstroms, however, have achieved spatial resolutions of a few tens of nanometers in microscopes around the world. Nanofabrication technology has permitted the fabrication of high quality Fresnel zone plate optics, with modest numerical aperture, in the soft x-ray region. In this thesis, we report the achievement of a spatial resolution better than 15 nm with the full-field soft x-ray microscope, XM-1, at the Lawrence Berkeley Laboratory’s

Advanced Light Source. This resolution represents a factor of three improvement over previous achievements with photon-based imaging microscopes.

A great advantage of soft x-rays is that the photon energies, extending from a few hundreds eV to a few keV, encompass the primary absorption edges of many elements, including C, O, N, Al, Ti, Fe, Co, and Ni, to name a few, enabling both elemental and chemical identifications. Magnetization sensitivity, an important feature for the fast-growing field of magnetic nanostructures, can also be obtained in soft x-ray microscopy, by use of circularly polarized radiation and spin-sensitive absorption¹. These capabilities

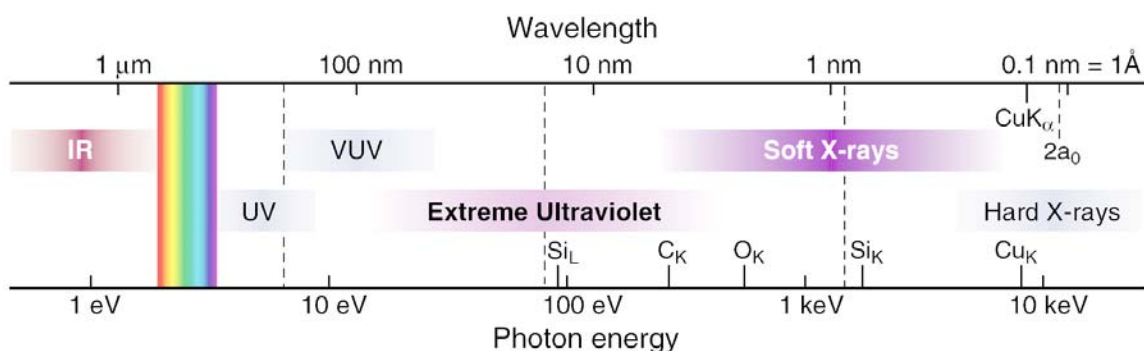


Figure 1-1. Radiation spectrum from infrared to x-rays, with photon energies from less than 1 eV to more than 10 keV. For x-rays, two sub-areas are commonly recognized: soft x-rays and hard x-rays. The soft x-ray region spans from 0.2 keV to a few keV, while the hard x-ray region ranges from a few keV to a few tens of keV. These two regions cover most elemental absorption edges. The soft x-rays offer various scientific opportunities for elemental and chemical analyses of high spatial resolution. (Following reference ²)

can be applied to samples of 1-10 μm thickness, depending on the material composition and photon energy used*. Typically, the samples are in air, and the use of photons permits in-situ studies in numerous sample environments and conditions, including hydration, cryogenic temperature, applied electric and magnetic fields, and use of thin windows, overcoatings or substrates. These capabilities, combined with the high spatial resolution described above, complement those of electron and scanning probe microscopies. With this combination of high spatial resolution, elemental sensitivity, and widely variable sample environments, soft x-ray microscopy has been utilized in a wide range of applications in both the physical and life sciences, yielding considerable knowledge³⁻⁹. The use of soft x-ray microscopy, often when combined with other analytic techniques, allows researchers to acquire a broad, in-depth understanding of sample composition, structure, and in some cases dynamics. In this dissertation, spatial resolution characterization of the versatile XM-1 soft x-ray microscope, and its resolution improvement, are presented. These new techniques can easily be transferred to other soft x-ray microscopes around the world.

Before further discussion of soft x-ray microscopy, a brief review of available optics in the x-ray region, their advantages and disadvantages, is presented in the next section.

* For magnetic imaging, where materials studied are relatively absorptive, sample thickness is limited to 1 μm or less.

1.2 Imaging Optics for X-Rays

In general, imaging optics can be based on reflection, refraction or diffraction. For visible light, reflection or refraction are most common, mostly notably refractive lenses. Examples of visible light imaging optics utilizing these mechanisms include eyeglasses, car mirrors, make-up mirrors, etc. X-ray imaging optics, on the other hand, are quite different from those for visible light. The main reason is that in the x-ray region the refractive index, n , expressed as $1-\delta+i\beta$, is very close to unity, where δ and β are typically very small, and gradually decrease for increasing photon energy. β/δ , a measure of absorptive effects, varies from near unity for extreme ultraviolet (EUV) [Fig. 1-1] and soft x-rays to much less than unity for hard x-rays. The proximity of β/δ to unity in the EUV, soft x-ray, and low energy portion of the hard x-ray region, implies that refractive lenses cannot create sufficient ray bending within an absorption length. For most parts of the x-ray region, δ is positive, such that the real part of refractive index is slightly less than unity. This permits total external reflection¹⁰, in which x-rays in vacuum can be reflected off a material surface at glancing incidence. These special properties form the basis of a unique set of optics based on reflection. The strengths and weaknesses of these optics, for the various x-ray regions (including EUV), are examined in this section.

For hard x-rays, the most commonly utilized imaging optics are glancing incidence optics¹¹, based on total external reflection. For imaging extended objects, these optics utilize at least two mirrors. A common form of such optics is known as a Kirkpatrick-Baez (K-B) mirror systems¹², in which a pair of curved mirrors is placed orthogonal to each other, focusing light in both horizontal and vertical directions.

Glancing incidence optics sometimes employ elliptically bent surfaces, or other conic sections, to minimize spherical aberrations. It is, however, difficult to fabricate non-spherical surfaces to accurate shape, with good polish[†] (low scattering). Furthermore, these glancing incidence reflective optics typically suffer from a small collection solid angle. Typically achieved spatial resolutions¹³ are of order 1 μm .

In addition to glancing incidence optics, Fresnel zone plates¹⁴⁻¹⁷, circular (diffractive) gratings (zones) with radially decreasing periods, have also been utilized for hard x-rays. In a zone plate, zones of various periods diffract some of the incident light to a focused point behind the zone plate lens, much like a conventional lens focusing visible light based on refraction. Diffractive focusing is obtained either by opaque zones (amplitude zone plates), or by π phase-shifting using phase reversal techniques (phase-reversal zone plates). Because of their diffractive nature, zone plates are highly chromatic, with focal lengths wavelength dependent. For high resolution and minimal aberrations, small outermost zone widths and accurate zone placement are required. Zonal materials providing sufficient absorption and/or phase shifting are needed for reasonable efficiency. Specialized electron beam lithography can achieve the desired zone widths and zone placement accuracy, but not the requisite zone thicknesses. For hard x-rays, where δ and β are particularly small, these thicknesses are not adequate for achieving sufficient absorption and thus reasonable diffraction efficiency. Zone thickness on the order of microns is generally required for hard x-rays. As thick zones of narrow widths are difficult to achieve, efficient, high resolution, hard x-ray zone plates have not

[†] Surface shapes are commonly referred as “figure”, and surface roughness (polish) is referred as “finish”.

yet been achieved. For harder x-rays, in the 10 keV or more energy range, achieved resolutions are order 1 μm . For multi-keV x-rays, where absorption is somewhat more favorable, zone plate lenses have yielded resolutions¹⁸ of order 120 nm. This field could advance significantly with the development of new methods for achieving thick, high aspect ratio[‡], zone plates for use with mid to high energy x-rays (few keV to 20 keV).

For soft x-rays, glancing incidence optics are again frequently utilized, but here the diffractive zone plates are especially effective. As described above, small zone with widths of order 20 nm, and with a thicknesses of 100 nm to 200 nm, can be fabricated using electron beam lithography, with high zone placement accuracy. For soft x-rays, materials that provide sufficient absorption at this thickness are readily available, thus permitting near theoretical efficiencies ($\sim 10\%$). This has permitted Fresnel zone plates utilized at soft x-ray wavelengths to achieve high-resolution. As described later in this thesis, spatial resolution better than 15 nm has recently been achieved, marking a significant advancement in the ability of soft x-ray microscopy to emerge as a variable tool for nanoscience, and nanotechnology.

In addition to soft and hard x-ray optics, it is worth discussing optics in the extreme ultraviolet (EUV) region, where photon energies are lower than soft x-rays, with wavelengths of a few to a few tens of nanometers. Significant advances have been made on the commonly used EUV optics, multilayer coatings¹⁹⁻²¹. These optics, composed of alternating layers of high and low Z (atomic number) materials, reflect radiation of

[‡] The aspect ratio is the zone thickness divided by its width.

particular wavelengths through scattering/diffraction by the periodic layered structures (Bragg's law). These optics[§] are particularly useful as near-normal incidence mirrors in the EUV region, with typically 20% reflectivity. One special example of multilayer mirrors is the Mo/Si multilayer coating, designed for use below Si L₃ absorption edge at 99.4 eV, with typical use at 13.5 nm wavelength (91.8 eV), where this coating combination has achieved a very high efficiency of 70%²². Proper control of figure and finish for curved (graded) multilayer optics has been achieved to minimize aberrations and scattering, yielding a spatial resolution of about 30 nm²³, with 0.3 NA optics at 13.5 wavelength²⁴.

In addition to multilayer optics, zone plate lenses are also utilized in the EUV region. At EUV wavelengths, where material absorption is stronger than in the soft x-ray region, zone plates with narrow zones and reasonable efficiency can be obtained. However, in order to obtain the proper diffraction by the zones, zone widths need to be larger than the operating wavelengths. For the EUV, where wavelengths extend from about 4 nm to a few tens of nanometers, zone widths are limited to the order of 40 nm. Therefore, in contrast to soft x-ray zone plate lenses, the resolution of EUV zone plates, which is mostly determined by outer (smallest) zone widths, is limited to about 50 nm.

In addition to the common optics discussed above, there are other optics used for the x-ray and EUV regions considered here. Examples are crystal optics, compound refractive lenses, Schwarzschild objectives, and pinholes. They all suffer various

[§] Depending on the optic design, multilayer mirrors can be used to perform spectral filtration, yielding reflected radiation with a bandwidth of a few percent. Glancing incidence optics, such as K-B mirrors, are sometimes coated with multilayers to achieve both imaging and monochromatization at the same time.

shortcomings that limit their uses. Crystals are frequently utilized as Bragg's diffracting monochromators in the hard x-ray region, where wavelengths are comparable to the crystals' lattice spacings. To use crystals²⁵ as imaging optics, crystals can be bent to obtain focusing. It is not possible, however, to significantly bend the crystals while maintaining inter-atomic lattice positions. This difficulty greatly limits the achievable optics' curvature, yielding very small numerical aperture (NA) and thus quite modest resolution (of order a few microns). Another type of optic, known as a compound refractive lens²⁶, is being developed. This optic is composed of multiple refractive lenses. As discussed above, refractive lenses are not practical for EUV soft x-ray wavelengths due to the small bending power and relatively high absorption of all materials. For very hard x-rays, in excess of 20 keV, however, where δ is quite small, but β is yet smaller ($\beta/\delta \ll 1$), modest light focusing can be obtained with multiple refractive lenses used in series. The individual lenses have concave shape profiles, due to the slightly positive δ . However, to avoid aberrations, in particular spherical aberration, the optic surfaces need elliptical profiles, which are difficult to fabricate. Furthermore, the small but finite absorption of the lens materials also limits the use of concave lenses to the optics' central areas near the optical axis, where the lenses are thinnest. This results in very modest effective numerical aperture. As a result the best resolution to date²⁷ are of order of 0.3 μm .

Quite common in the EUV region are Schwarzschild objectives²⁸, constructed by two near-normal incidence multilayer coated mirrors, frequently utilized for in scientific laboratory applications, for EUV lithography developments, and for EUV astronomy²⁹. In

contrast to glancing incident optics, aberrations are not as problematic for the near-normal incidence optics, especially at small NA^{30} (~ 0.1). It is, however, difficult to fabricate the optics with proper figure and finish for larger NA (~ 0.3) where aspherical surfaces are required.

In addition to the above optics, small apertures, or pinholes, are frequently utilized for imaging. Unlike the optics above, pinholes of varying opening sizes can be used at all x-ray and EUV wavelengths (as well as visible light). These optics are simple for fabrication and for use. The resolution achieved by these optics is about the opening size, on the order of microns or less. The major downside of the optics, however, is low throughput, due to the small opening dimension.

In summary, due to a combination of material characteristics in the x-ray region and optics technology, various soft and hard x-ray optics based on reflection, refraction, and diffraction permit modest resolution performance. The notable exception is Fresnel zone plates at soft x-ray wavelengths, which achieve high spatial resolution due in part to the short wavelength and the ability to fabricate small zone widths with high placement accuracy. Zone plate lenses allow the extension of visible light microscopy to x-ray capabilities, with additional attributes, e.g. elemental sensitivity, large permissible sample thickness, applied fields, viewing through overcoatings, etc., thus making soft x-ray microscopy a valuable analytic tool for nanoscale studies. The principles and design of Fresnel zone plates, and their fabrication using specialized e-beam lithography are discussed further in the next chapter.

1.3 Soft X-Ray Microscopes Based on Fresnel Zone Plate Lenses

There are two common types of soft x-ray microscopes – scanning transmission microscope and full-field transmission microscope – both of which use photon transmission throughout the system. Figure 1-1 shows partial schematics of the two complementary microscopes. General characteristics of these microscopes are described below.

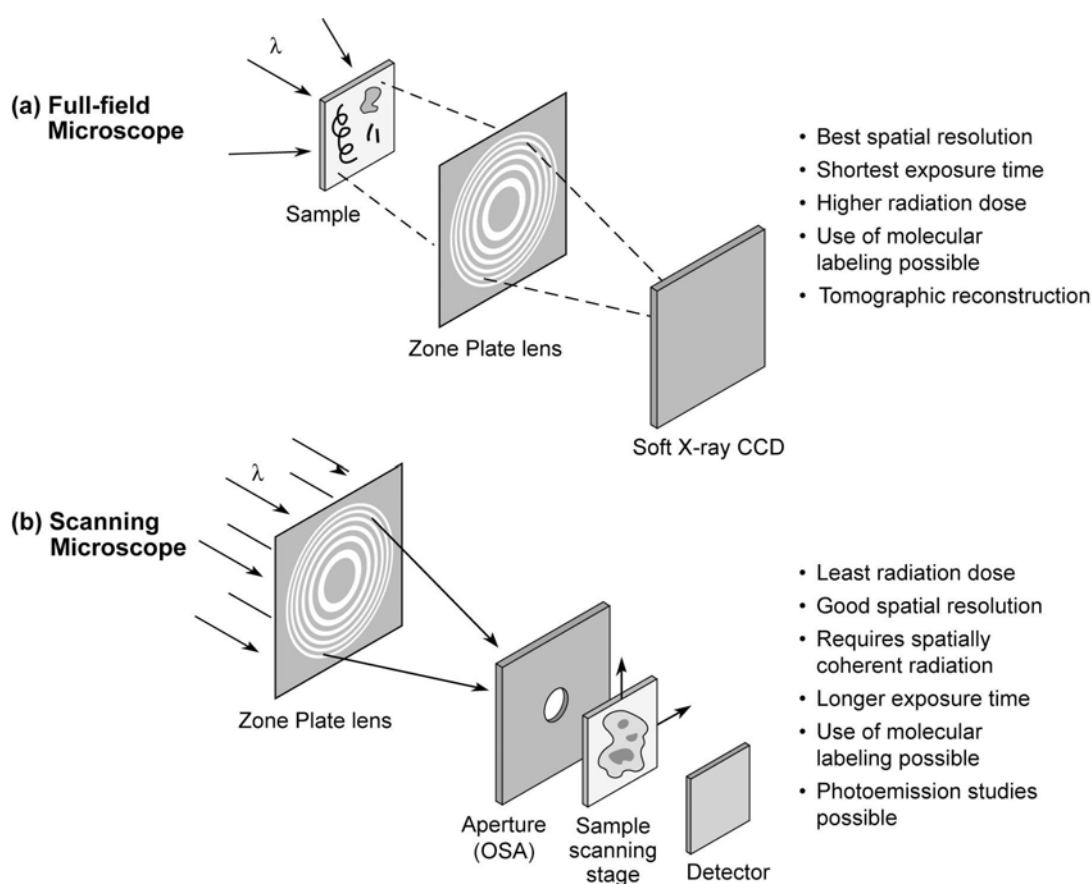


Figure 1-2. The two common soft x-ray microscopes: (a) a full-field microscope in which a complete image of the sample is formed by a Fresnel zone plate lens onto a CCD detector in a single exposure and (b) a scanning microscope in which a sample is mechanically scanned by a focused spot and the image is constructed pixel by pixel by computer. Their main features, listed next to the diagrams, are complementary to each other. (Following reference 2)

1.3.1 Full-field Transmission Soft X-Ray Microscopes

Development of the full-field soft x-ray microscope has been pioneered by Schmahl, Rudolph, Niemann, and their colleagues³¹⁻³⁶ at George-August University in Göttingen, at first using bending magnet radiation at LURE in France, and later at BESSY synchrotron facility in Berlin. This microscope is the x-ray analog of a conventional visible light microscope. It uses a Fresnel zone plate as an objective lens to project a full-field image onto an x-ray sensitive CCD detector [Fig. 1-2(a)]. A spatially *incoherent* x-ray source, combined with a large condenser zone plate, provides critical illumination for the imaging [Fig 1-3]. Broadband, spatially incoherent bending magnet³⁷ radiation from a synchrotron is typically used for supporting a large operating spectral range, short exposure time (seconds), and high spatial resolution for the microscope. As we shall see in Chapter 2, Fresnel zone plates, like other diffractive optics are highly chromatic, and have relatively modest efficiency (typically 10%) and various diffraction orders. In order to obtain optimal imaging performance from the objective zone plate, sample illumination requires a narrow spectral bandwidth. Towards this end, the microscope requires monochromatization and control of diffractive orders. This is accomplished by combination of the condenser zone plate, a central stop, and a pinhole close to the sample [Fig. 1-3]. The relative spectral bandwidth achieved is modest, about one part in 500-700, which is sufficient to minimize chromatic aberration, as well as permit elemental and spin-orbit selectivity.

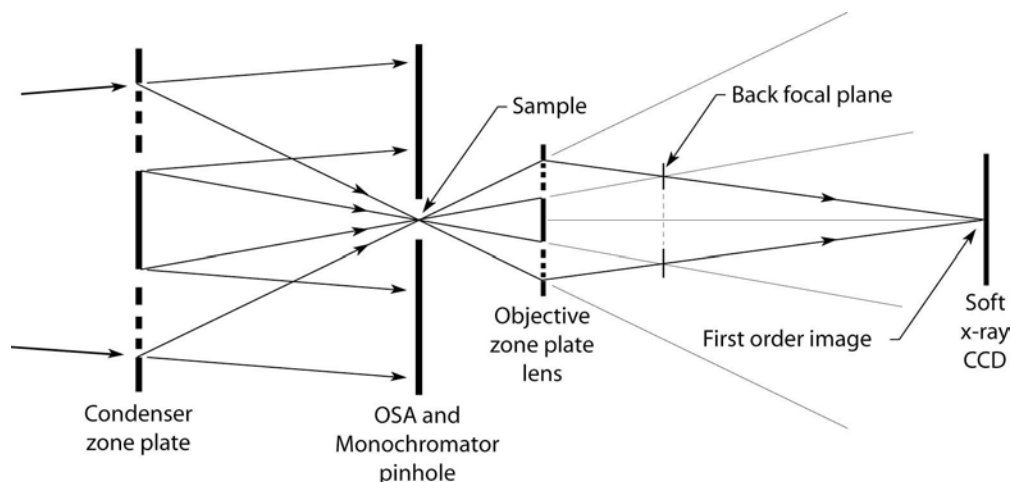


Figure 1-3. Schematic of the condenser and imaging parts of the full-field transmission soft x-ray microscope. A condenser zone plate with a central stop in conjunction with a pinhole form a monochromator, and illuminate the sample with first order radiation. The pinhole also serves as an order sorting aperture to block all but the first order from reaching the sample. An objective zone plate projects a high resolution, highly magnified full-field image onto a soft x-ray CCD detector. With the use of an annulus phase plate in the back focal plane of the objective zone plate, the microscope can also provide phase contrast imaging. (Following reference 2)

The main features of this microscope are its simplicity and excellent imaging performance. Various images are shown later in chapter 2, in figure 2-2 and 2-3. As we shall see in chapter 2 and 3, the spatial resolution depends on the outermost zone widths of the object zone plate and the sample illumination. By use of state-of-the-art Fresnel zone plate fabrication and optimized angular illumination, the microscope can provide the highest spatial resolution. Images of sub-20 nm resolution are reported here, with typical exposure time of a few seconds, and as many as 1000 images per day. Phase contrast imaging is also possible, with the use of a phase annulus in the back focal plane of the objective zone plate^{38,39} [Fig. 1-3]. Due to the modest zone plate efficiency, typically

10% to 20%, radiation dose to the sample is relatively high. Radiation damage to sensitive samples, however, can be obviated at the 10 nm structural scale by the use of cryogenic fixation^{36,39}. At the molecular level, in fibers, biological samples, and other soft materials, the radiation damage, which results in the breaking of molecular bonds, can be observed at high spectral resolution. In such cases use of a scanning microscope, with reduced sample dose has an advantage.

1.3.2 Scanning Transmission Soft X-Ray Microscopes

Development of the scanning transmission soft x-ray microscope has been pioneered by Kirz, Rarback, Jacobsen, and their colleagues at SUNY Stony Brook and Brookhaven National Laboratory⁴⁰⁻⁴⁴, first using bending magnet radiation and later undulator radiation at Brookhaven's National Synchrotron Light Source (NSLS). In this microscope, spatially *coherent* soft x-rays illuminate a zone plate, which forms a first order focal spot on the sample [Fig. 1-2(b)]. The sample features illuminated by the spot transmit and scatter the radiation, which is then collected by a fast x-ray detector downstream. The sample is raster-scanned in front of the focal spot and the transmitted signal is detected and correlated with sample position to construct an image. The microscope is typically used with high-brightness undulator radiation³⁷, of relative bandwidth in one part of a few thousands as set by the upstream monochromator (not shown in Fig. 1-2(b)). Spatial filtering of the undulator radiation is required to obtain the requisite spatially coherent illumination of the focusing zone plate. Typically this reduces available flux by several thousands. Although spatial resolution is often affected by the

scanning stage accuracy, recent progress with interferometric position control has led to an improvement of spatial resolution⁴⁵ approaching the diffraction limit of 30 nm.

For this microscope, the resolution mainly depends on the focal spot size formed by the zone plate. In order to obtain the smallest spot, radiation in all but the first order is prevented from reaching the sample by use of a central stop on the zone plate in conjunction with an order sorting aperture (OSA), as illustrated by Fig. 1-4. Use of spatially coherent radiation, aberration-free zone plates, and high precision sample stages

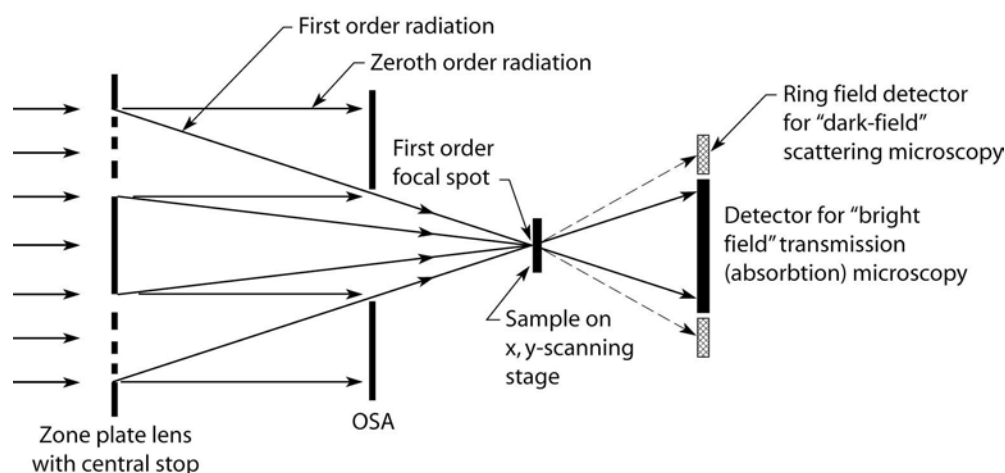


Figure 1-4. Illustration of suppression of all but the first order radiation by means of a central stop and order sorting aperture (OSA) in the scanning transmission x-ray microscope. Also shown is acquisition of the sample's absorption and scattering profile using a segmented x-ray detector and raster-scanning of the sample by the first order focal spot. With different detector geometry or detection mechanisms, the scanning microscope can be used in various imaging mode: differential phase contrast^{46,47}, fluorescence or luminescence⁴⁸, and photoelectron emission^{49,50}. (Following reference 2)

are important for achieving diffraction-limited resolution in this microscope. Note that due to the absence of optics between the sample and detector, the combination of central stop and order sorting aperture minimizes the radiation dose to the sample.

The features of the scanning soft x-ray microscope, as described earlier, complement those of the full-field microscopes. While the full-field microscope is best suited for high resolution imaging over a large area, the scanning microscope is best used for spectromicroscopic studies (a combination of spectroscopy and microscopy), such as chemical analyses, which require high spectral and spatial resolution. Using radiation of small bandwidth, the elemental and chemical composition of the sample can be obtained using this microscope, by either direct detection of x-rays transmitted or scattered^{46,47} by the sample, as discussed above, or detection of fluorescent/luminescent radiation⁴⁸ or photoelectrons^{49,50} excited by the incident x-rays using other types of detectors. The numerous detection mechanisms permitted by the microscope enable this instrument to be a powerful spectromicroscopic tool in many scientific areas including biology, chemistry and polymer science³⁻⁹.

1.4 Overview of the thesis

The full-field transmission soft x-ray microscope, XM-1, is a powerful, high-performance nano-imaging tool. Located at Lawrence Berkeley National Laboratory's (LBNL) Advanced Light Source (ALS), this microscope has been extensively utilized in a broad range of sciences and technology. In this dissertation, improvement and characterization of this microscope's spatial resolution, one of the principal features of

this instrument, are presented. These results represent a significant advancement in soft x-ray microscopy, enabling the versatile microscopic capabilities elemental specificity, applied fields, overcoatings) to be further utilized in today's nanoscience and nanotechnology.

This dissertation is divided into seven chapters. In the first chapter, general features of soft x-ray microscopy have been presented. In chapter 2, the design, capabilities, and applications of the microscope, as well as conventional zone plate fabrication, are described. Fundamental image formation principles used in the microscope, which are useful in understanding the resolution performance of the instrument, are presented in chapter 3. In chapter 4, various resolution measurement techniques are described. The results of resolution characterization obtained with these techniques are presented and discussed in chapter 5. In chapter 6, a new overlay technique is described that enables nanofabrication of zone plates with the world's finest zone structures. With this new technique, zone plates of 15 nm outer zone width have been successfully fabricated for the first time. The significant improvement in resolution achieved with these zone plates is also presented and discussed in chapter 6. The conclusion and final thoughts on progress in soft x-ray zone plate microscopy is presented in chapter 7.

Chapter 2

Soft X-Ray Microscope XM-1 and Fresnel Zone Plate

2.1 Overview

The full-field, transmission soft x-ray microscope XM-1, at the Advance Light Source (ALS), is one of the main subjects in the work here, and is discussed in this chapter. The chapter starts with a survey of the microscope's capabilities and applications. The design of the microscope, and the fundamental properties, advantages and trade-offs of Fresnel zone plate lenses – essential optics of the microscope, are next presented.

2.2 Capabilities and Applications of the Soft X-Ray Microscope XM-1

The full-field transmission soft x-ray microscope XM-1^{51,52} has a unique combination of capabilities. One of the most important capabilities is its high spatial resolution. Using high-quality Fresnel zone plate lenses with the smallest zone widths ever fabricated, the microscope has achieved a *spatial resolution between 12nm and 15 nm*, which is a factor of 3-8 better than the competing photon-based imaging techniques, and is currently the best in the world. Details of the zone plate fabrication for achieving the spatial resolution and the measurement are presented in chapter 6. This property, combined with the others below, makes this microscope a unique nano-analytic tool complementary to instruments of other microscopy.

Use of the soft x-rays also allows the microscope for providing *elemental identification*. The operating energy range of the microscope is from 0.3 keV to 2 keV (λ

= 4 nm to 0.6 nm), encompassing primary K and L atomic resonance of many low-Z elements, including C, N, O, Al, Ti, Fe, Co, Ni, and Si [Fig. 1-1]. Combined with *good penetration*, the microscope provides natural absorption contrast for a variety of specimen. Wet biological and environmental specimens, of up to 10 μm thick, can be imaged without staining in the “water window” [Fig. 2-1], a spectral range extending from the carbon K edge (284 eV, $\lambda = 4.37$ nm) to the oxygen K edge (543 eV, $\lambda = 2.28$ nm), in which water is more than an order magnitude transmissive than organic cell organelles. Many other elements, such as iron and calcium, also possess absorption lengths comparable to carbon in the water window, and can be imaged and identified in hydrated samples. Furthermore, interconnects in operating integrated circuit boards, with silicon substrates thinned to 10 μm thick, can be imaged at a photon energy of 1.8 keV ($\lambda = 0.69$ nm). In addition to elemental identification, elliptically polarized radiation emitted off the electron orbit plane of the bend magnet (next section) allow the microscope for providing *magnetization sensitivity* through circular dichroism⁵³, an effect based on spin-orbit coupling. Magnetic nanostructures, composed of elements such as Fe, Co, Ni, or Gd, to name a few, can be studied using the microscope.

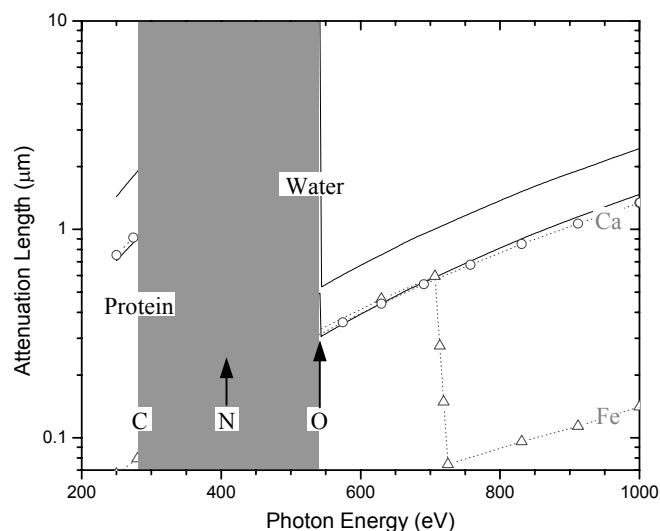


Figure 2-1. Attenuation lengths of a typical protein and water. The shaded energy region, called the “water window,” extending from the carbon K edge (284 eV, $\lambda = 4.37$ nm) to the oxygen K edge (543 eV, $\lambda = 2.28$ nm), allows imaging by natural absorption contrast of whole hydrated biological cells, with thickness up to 10 μm . In addition, by subtraction of images taken above and below absorption edges, one can identify the elemental content of the sample. The L edges and attenuation lengths of two commonly studied elements at the microscope, calcium and iron, are shown in gray color for reference.

Moreover, the photon-based microscope allows *in-situ application of various imposed sample conditions*, including elevated or cryogenic temperature, applied magnetic fields or electric currents. Synchronization of magnetic field pulses with the electron bunches in the synchrotron facility enables time-resolved pump-probe experiments for magnetization dynamical studies.

All of the above capabilities can be obtained in an *exposure of a few seconds*. Combined with *user-friendly operation*, the microscope provides a *throughput up to 1000 images a day*. Biological imaging with protein specific labeling⁵⁴, humic substances with elemental sensitivity, and cement studies in hydrated environments^{55,56} have acquired valuable knowledge through the use of the microscope. Cryogenic computed tomography of whole, hydrated biological cells has been successfully employed to provide 3D imaging with natural contrast^{57,58}. Nano-magnetism, including spin inhomogeneity and domain movements^{53,59}, and dynamics⁶⁰, are studied in-situ in applied magnetic fields. Tomographic reconstruction of interconnect stacks in operational electronic devices has been performed for understanding electromigration at high current density⁶¹. The unique combination of microscope's capabilities is opening many opportunities to better understand the physical and life sciences^{62,63}, proving the microscope as an important feature nano-analytical tool. Examples of the various applications are shown in Fig. 2-2 and Fig. 2-3.

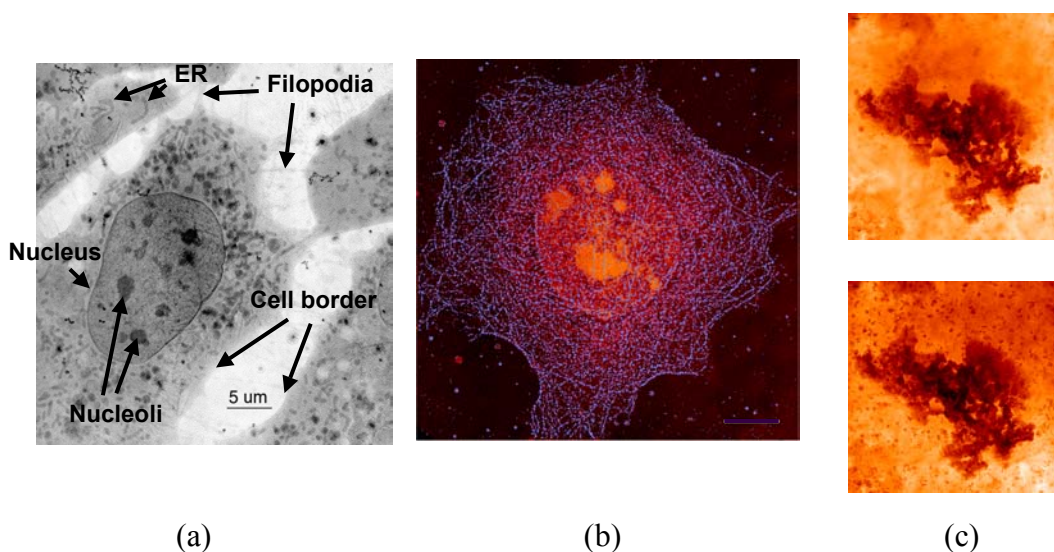


Figure 2-2. A short survey of various hydrated applications of the microscope. (a). A montage assembly of a cryogenic fixed hydrated mouse 3T3 fibroblast cell, imaged at 517 eV ($\lambda = 2.40$ nm). The nucleus contains several nucleoli, surrounded by a distinct nuclear membrane. Numerous vesicles and organelles such as mitochondria are seen in the cytoplasm. The cell was initially living, then rapidly frozen and imaged in a cryo-stage while cooled at liquid nitrogen temperature. No chemical fixation or contrast enhancement was used. The montage was formed by tilting a series of 144 images in software. (Courtesy of C.A. Larabell, D. Yager, and W. Meyer-Ilse, LBNL⁶⁴.) (b) A microtubule network of a whole hydrated mouse epithelial cell (Eph4), imaged at 517 eV ($\lambda = 2.40$ nm). A double-labeling technique was used to locate the distribution of the protein network (colored in blue), extending throughout the cell. The nucleus is colored in orange, with its absorption scaled to the color. The image was a composite montage of 144 individual, 10- μm -in-diameter images. The montage image had a total size of 32 μm by 32 μm . (Courtesy of C.A. Larabell, W. Meyer-Ilse, D. Hamamoto, A. Nair, S.A. Lelièvre, D. Yager, and colleagues, LBNL.⁵⁴) (c) Hydration of CaAl_2O_4 , at 7 hour 35 min. (top) and at 8 hour and 45 min. (bottom) (Courtesy of V.H.R. Lamour and P.J.M. Monteiro *et. al.*⁶⁵).

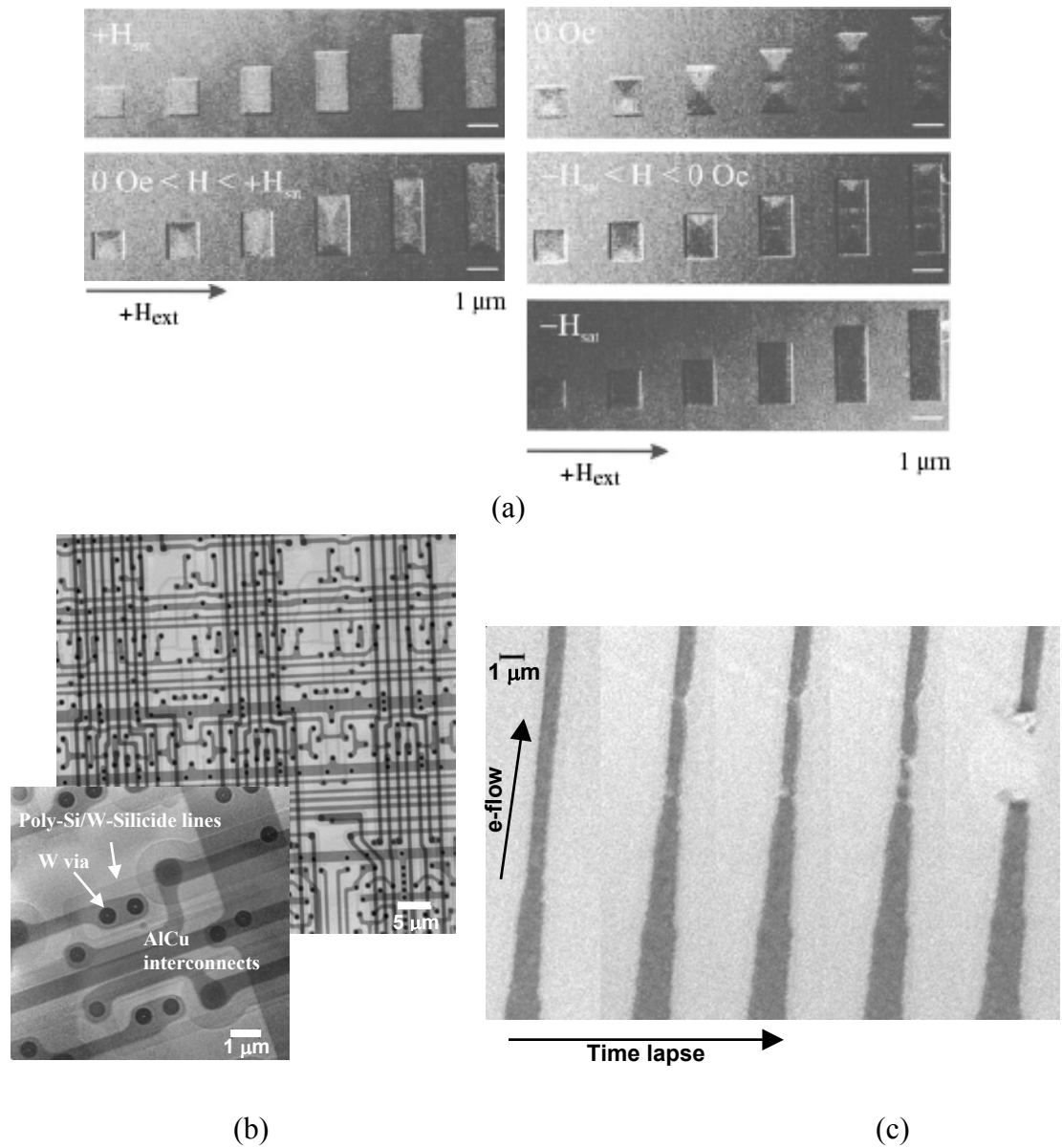


Figure 2-3. Material science studies through the use of the microscope. (a) Studies of distribution and reversal of magnetization in 50 nm thick permalloy (a NiFe alloy) rectangular elements at the Ni L_3 edge (853 eV, $\lambda = 1.45$ nm), in-situ with applied magnetic fields along the short edge. The aspect ratios (width: height) of the patterns vary from 1:1 to 1:3. The in-plane magnetization in the light domains is pointing to the right, dark to the left. (Courtesy of P. Fischer *et. al.*⁵³) (b) An x-ray image shows a top-down overview of an intact IC. Interconnects and vias are shown clearly. The image is obtained by imaging through three composite metallic layers. A photon

energy of 1.8keV ($\lambda = 0.69$ nm) is used for deep penetration and good material contrast. Structures of an AlCu metallization layer, and Si/WSi lines, which have lower contrast than AlCu interconnects at the photon energy, are also seen clearly. The complete structures are supported by the circuit's silicon substrate thinned to a thickness of 10 μm . (c) X-ray images showing time sequence of a wire which broke due to the mass transport by electromigration in a passivated copper interconnect. During the 30 minute observation, the time sequence of images, each with an exposure of about 1 second, recorded the interconnect under application of a DC current of 49.8 mA. The current density was increased up to 10^7 A/cm² due to the decreasing interconnect cross section caused by the mass transport. The thickness of the copper layer is 350 nm and its linewidth is 600 nm. The silicon wafer was thinned to a thickness of about 5 μm . (Courtesy of G. Schneider and colleagues, LBNL, D. Hambach, Universität Göttingen, N. Hoffmann and colleagues, Universität Hannover, and K. Hoffmann, Micronas GmbH⁶⁶.)

2.3 Design of the Transmission Soft X-Ray Microscope XM-1

The soft x-ray microscope XM-1 is composed of four parts: source, condenser, imaging optics, and a CCD detector [Fig. 2-4]. Situated at beamline 6.1.2 of the Advanced Light Source⁶⁷ (ALS), the full-field, transmission microscope uses bend magnet radiation for imaging. With a typical 1.9 GeV electron energy, the bend magnet³⁷ forces highly relativistic electrons to accelerate in an arc, emitting broadband (from infrared to hard x-rays) incoherent radiation. The critical photon energy³⁷, E_c , a characteristic of the radiation spectrum, is 3.05 keV ($\lambda_c = 0.407$ nm). The photon flux of an ALS bend magnet is shown in Fig. 2-5.

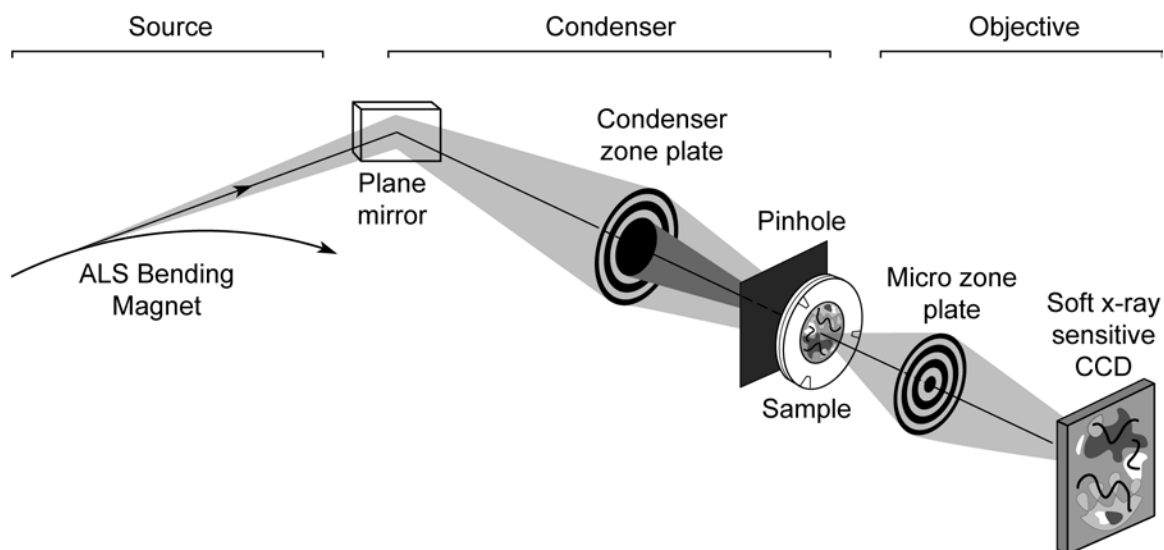


Figure 2-4. A schematic of the full-field, transmission soft x-ray microscope, XM-1, at the Advanced Light Source (ALS).

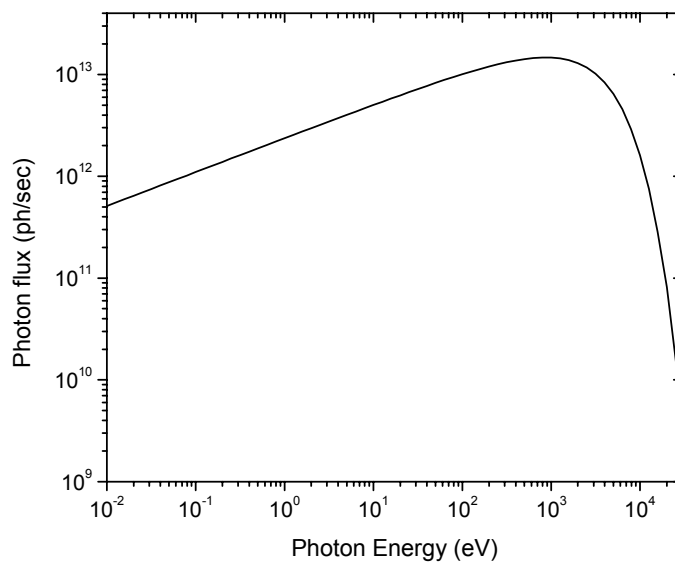


Figure 2-5. The calculated photon flux, photons per second, of an ALS bend magnet is shown. The curve is calculated for a 1/700 bandwidth and a horizontal acceptance angle of 0.6 mrad, which are the usual microscope's conditions. The typical ALS operating parameters are also used: 400 mA beam current, 1.9 GeV electron energy, and $E_c = 3.05$ keV.

The broadband radiation is incident upon a plane mirror at a grazing angle of 3° , which blocks high energy photons which are detrimental to the CCD camera lifetime. The current mirror has two areas, one coated with nickel, the other with 50 bilayers of 6 nm ruthenium/9 nm silicon⁶⁸. The nickel mirror reflects radiation below the nickel L_3 absorption edge, 852 eV, to the microscope, but absorbs the photons above. The mirror is optimal for imaging at energy below 800 eV, including the water window. Most of the work in this dissertation was conducted with the multilayer coating, which was designed and fabricated in-house primarily for electromigration studies at 1.8 keV. The multilayer reflects mainly photons below 2 keV, with a small reflection for photons of higher energy. With this coating, the microscope has an operating range from 0.3 to 2 keV ($\lambda = 4$ nm to 0.6 nm).

Following the mirror, the remaining radiation is then collected by a condenser zone plate (CZP). The condenser zone plate images the bend magnet source onto the sample plane, i.e. critical illumination is used. This zone plate [Fig. 2-6], typically of 9 – 10 mm diameter, has two paramount functions. It captures most of the radiation, and provides a proper illumination angle to enhance the microscope's spatial resolution. Used with a pinhole aperture near the sample plane, it also functions as a linear monochromator, selecting a particular wavelength suitable for studying certain properties of the samples. The monochromaticity of the condenser, in combination with the pinhole, typically achieves 700 over a 4- μ m-diameter area at the center of the field of view⁶⁹. Furthermore, to block undiffracted light from reaching the sample plane, a central stop made of a circular metal plate with a diameter of 4 – 5 mm is installed at the center of the

condenser zone plate. Undiffracted light passing through the condenser's region outside the central stop is blocked by the pinhole aperture. The illumination formed by the condenser with the stop and pinhole is thus *hollow-coned* [Fig. 2-4]. The effect of illumination angle on imaging is discussed thoroughly in chapter 3. The principle of zone plate monochromatization is described in the next section.

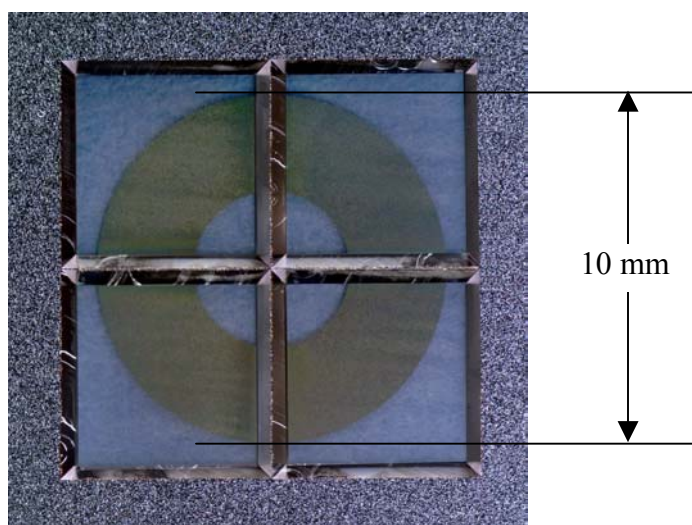


Figure 2-6. Photograph of a 10-mm-diameter condenser zone plate. The outermost zone width, Δr_{CZP} , is 60 nm. The zones at the center are replaced by the central stop. The zone plate is fabricated on a 100-nm-thick, low-stress, silicon nitride membrane window. The condenser, combined with the pinhole and the central stop, provides a hollow-coned illumination.

The radiation illuminates the sample, which is in air, or in a water bag if desired. The radiation transmitted and diffracted by the sample passes a vacuum window, and is collected by the micro zone plate (MZP) [Fig. 2-4], which projects an image of the sample onto a soft x-ray sensitive, back-thinned CCD detector (2048 x 2048, model NTE, Roper Scientific, Trenton, NJ). The field of view is 10 μm in diameter at 2400X magnification, and varies for different magnification. The detector has a quantum

efficiency above 70% for soft x-rays. Placed on a movable platform, it traverses from 1 to 2 meters from the micro zone plate for variable magnification. The magnification ranges from 2000X to 10,000X, depending on the wavelength, MZP focal length, and CCD position.

2.4 Fresnel Zone Plates

Fresnel zone plates, circular gratings with radially decreasing periods, have been employed as high-resolution soft x-ray lenses [chapter 1]. They perform point-to-point imaging, like conventional lenses^{17,*}. For amplitude zone plates, opaque zones (rings) block the light that would otherwise destructively interfere in the image plane with the light passing through the clear zones. Optical paths from an object point to its image point through the opaque zones are half a wavelength different from those through the adjacent clear zones [Fig. 2-7]. Using the notation in Fig. 2-7, the zone placement must satisfy

$$s_n + t_n = s_{n-1} + t_{n-1} + \lambda/2 \quad (2-1)$$

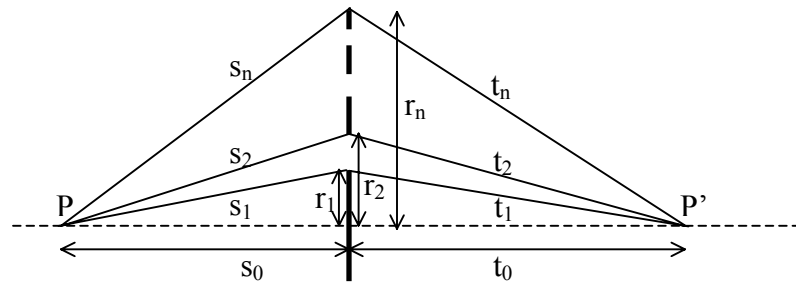


Figure 2-7. Illustration of light propagation through a zone plate from an object point P to an image point P'.

* The point spread function (PSF) of a zone plate is somewhat different from the PSF of a conventional lens, which is an Airy pattern. The difference, however, becomes negligible as the number of zones approaches 100 or larger¹⁷, which is easily satisfied in typical zone plate designs.

where λ is the wavelength, and the subscript n represents passage through the n th zone from the center. Assuming the total number of zones, N , is larger than 100, which can be easily satisfied by soft x-ray zone plates, Eq. (2-1) can be simplified to^{70,71}

$$r_n^2 \approx n\lambda f + \frac{n^2\lambda^2}{4} \quad (2-2)$$

Furthermore, if the numerical aperture (NA) is small (<0.1), the quadratic term, which is the correction to spherical aberration, is negligible compared to the first two terms. Thus,

$$r_n^2 \approx n\lambda f \quad (2-3)$$

For a focal length, f , the zone plate obeys the thin lens equation, $s_0^{-1} + t_0^{-1} = f^{-1}$, where the magnification $M = t_0/s_0$. With a few manipulations, one can show that for $M \gg 1$:

$$\begin{aligned} NA &\cong \frac{\lambda}{2\Delta r} \\ f &\cong \frac{D\Delta r}{\lambda} \cong \frac{4N(\Delta r)^2}{\lambda} \\ D &\cong 4N\Delta r \\ F^\# &\cong \frac{\Delta r}{\lambda} \\ \text{Depth of focus} &= \pm \frac{1}{2} \frac{\lambda}{(NA)^2} \cong \pm \frac{2(\Delta r)^2}{\lambda} \end{aligned} \quad (2-4)$$

where Δr is the outermost zone width, D is the diameter, and N is the total number of zones (clear and opaque). Note that as a diffractive optic, a zone plate's focal length is

dependent on the wavelength[†]. In order to minimize the strong chromatic aberration, it is necessary that the number of zones, N , be limited to⁷⁰

$$N \leq \frac{\lambda}{\Delta\lambda}. \quad (2-5)$$

$\Delta\lambda/\lambda$ is the normalized spectral bandwidth of the illumination. For an experimentally required bandwidth, the above dictates the maximum number of zones. More importantly, spatial resolution, referred to below as Res, depends to a large extent only on the outermost zone width. For $M \gg 1$, the spatial resolution is equal to

$$\text{Res} = k_1 \frac{\lambda}{\text{NA}} \cong 2k_1 \Delta r \quad \begin{cases} \sigma = 0 & k_1 = 0.61 \\ \sigma > 0 & 0.25 \leq k_1 < 0.61 \end{cases} \quad (2-6)$$

where k_1 is an illumination dependent constant, and σ , equal to the condenser's NA divided by the imaging optic's NA , is a parameter known as the partial coherence factor, which characterizes the spatial coherence of the illumination. Thus the prevalent method of resolution improvement is to reduce the outermost zone width of the micro zone plate. Fundamental properties and subtleties of the σ -dependent resolution and Eq. (2-6) are discussed in chapter 3. As a note, one can use Eq. (2-3) to show that each zone occupies the same area and thus contributes almost equally, within the obliquity factor⁷², to the image intensity.

[†] Using to the dependence of a zone plate's focal length on wavelength, one can spectrally filter radiation by placing a small pinhole close to the focal plane at the desired wavelength. The pinhole size is somewhat larger than the expected illumination spot in the focal plane. A monochromator composed of a linear grating and a slit shares the very same working principle. In the case here, the zone plate is a circular grating with radially decreasing periods.

In the amplitude zone plate design above, abrupt change in absorption occurs at zone boundaries, i.e., the cross section profile is rectangular. This leads to higher order diffraction, of both positive and negative orders in which light converges or diverges, respectively, from the lens [Fig. 2-8]. For the cross section profile depicted by Fig. 2-7, diffraction efficiency to various orders is given by,

$$\eta_m = \begin{cases} 1/4 & m = 0 \\ 1/(m\pi)^2 & m \text{ odd} \\ 0 & m \text{ even} \end{cases} \quad (2-7)$$

where m represents the diffraction order^{70,73}. The first order diffraction, which is commonly used in zone plate imaging, has an efficiency of about 10%. In addition, the zone plate absorbs 50% of the incident light. More efficient designs use phase-reversal zone plates^{14,16,74,70}, in which alternate zones are not absorbent, but rather composed of

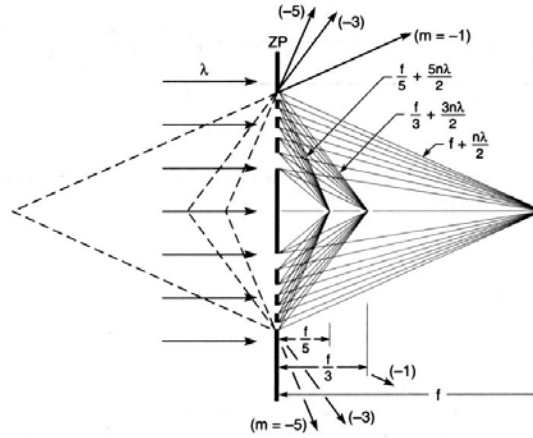


Figure 2-8. Zone plate diffractive focusing is illustrated for the first three positive orders ($m=1,3,5$), in which radiation converges in back focal planes. The first three negative orders ($m=-1,-3,-5$), which appear to diverge from virtual foci, are also shown.

phase-shifting material which converts the destructive light to constructive light. If accomplished without absorption, this doubles the electric field at focus, or in the image plane, thus quadrupling the diffraction efficiencies, i.e., first order efficiency is 40%.

In practice, materials both phase-shift and absorb. Kirz⁷⁴ has calculated efficiencies for varying degrees of absorptive materials and showed that materials with minimum β/δ will yield the highest diffraction efficiency [Fig. 2-9]. Thus, preferred zone plate materials should satisfy the following criteria:

- the material has small β/δ in wavelength range of interest.
- The ratio of the thickness t required for optimal efficiency to the given zone widths needs to be smaller than the highest aspect ratio[‡] achievable by zone plate fabrication. (a nanofabrication challenge).
- the material has to be compatible with zone plate fabrication.

In the water window, between the carbon (284 eV) and oxygen (543 eV) K edges, nickel is a relatively good material for this purpose. It has δ almost three times of β , and a modest thickness of 240 nm yields a first order efficiency of 23% at 2.4 nm (516 eV)[§]. Because nickel electroplating can be incorporated into zone plate fabrication, it is the

[‡] Aspect ratio is the ratio of zone thickness to its width.

[§] Because phase effect strongly depends on the material thickness and wavelength, the desired high efficiency of nickel zone plates, which use phase effect for efficiency improvement, can be only be obtained with zone thickness close to the optimal value at the wavelength of interest. Otherwise, other materials may yield better efficiency than nickel. For instance, at 2.4-nm wavelength, gold, which is another commonly used material, is a better choice of material for zones thinner than 80 nm.

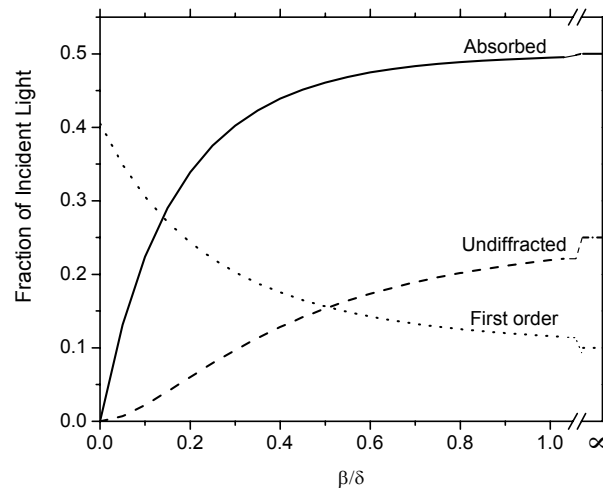


Figure 2-9. The amount of absorbed, zero order (undiffracted), and first order radiation optimized in zone thickness for various β/δ values⁷⁴.

preferred material for water-window zone plates. In the following section, zone plate fabrication using electron beam lithography will be described further.

To end this section, characteristics of soft x-ray zone plates are summarized as follows:

Advantages

- best resolution among all focusing elements;
- perform point-to-point imaging like a refractive lens;
- zone plate dimensions for soft x-ray focusing and material thickness needed for acceptable efficiency are within fabrication capability.

Disadvantages

- multiple diffraction orders, in particular strong zero order background^{**};
- low efficiency = 10-40%.

2.5 Zone Plate Fabrication with the Nanowriter Electron Beam Lithography System

All condenser and micro zone plates characterized in the work here have been fabricated in-house using a 100 keV, vector-scan electron beam lithography tool⁷⁵, the Nanowriter, in the Nanofabrication Laboratory of LBNL's Center for X-ray Optics. The tool has excellent resolution, and accurate pattern placement and overlay alignment. It was designed with particular attention to curved structures (e.g., zone plates) writing. The Nanowriter uses the electron optical column, stage and auxiliary subsystems of the Leica Microsystem VB6-HR system⁷⁶, which are controlled by an internally developed digital pattern generator⁷⁷ (DPG), software, and electronics. The high performance of the Leica Microsystem, the unique DPG, and the effective algorithms (exposure, alignment and calibration) produces placement and alignment accuracy of about 3 nm and 2 nm, respectively.

The Leica electron optical column consists of a tungsten thermal field emission source for high brightness, giving small probe sizes and high current. The accelerating voltage can be varied between 20 and 100 keV, with the best lithography results and the smallest beam diameter⁷⁸, 6.5 nm, obtained at 100 keV. The stage travel range is approximately a 150 mm by 150 mm area and incorporates a three-axis (x, y, θ), $\lambda/1024$ (0.6 nm) resolution interferometer for positional measurement, feedback, and control. A

^{**} For small β/δ , zeroth order background is very small. See Fig. 2-9.

transmitted electron detector is mounted directly under the stage for on-axis alignment and calibration.

Much of the critical and sophisticated operations during exposure are performed by the DPG, which directly drives the deflection and blanking of the electron optics. The DPG delivers X and Y analog beam deflection signals for both the major-field (slow-speed, large and somewhat coarse deflection) and minor-field (high-speed, small and fine deflection) amplifiers, which are used collectively to control beam position for patterning. The writing strategy of the Nanowriter is vector placement with spiral fill, in which the electron beam spirals inwards to fill the patterns, for full utilization of DPG's bandwidth. Corrections to the field distortion and beam profile (i.e. the fine focus and X and Y stigmatism), exposure mapping, and proximity dose correction are also implemented dynamically during exposure by the DPG.

For the best writing performance, especially for diffractive optics, alignment and calibration of the Nanowriter are crucial. A window wafer made of a 100 nm thick silicon nitride membrane with gold "islands," is used as test objects for on-axis alignment. These test objects are also used for characterizing the x-ray microscope [section 4.3.4]. The on-axis alignment begins with collection of a series of gold island images for various focus/stigmatism settings. The size and ellipticity of the images' autocorrelation functions are measured and fitted with a second order polynomial using singular value decomposition⁷⁹, yielding the optimal electron optic setting which has minimal size and ellipticity. The complete process is automated. Nonlinear distortion, which is important to

large major fields such as those used for the condenser zone plates, is next corrected. The first step involves calibration of the laser feedback control of the stage. An image of a reference mark (e.g., dirt) is first taken and the stage is then moved a short distance within the feedback range. A new image is taken and the process is repeated for four different positions of the stage. Cross-correlation functions are used to determine the positional change between the images taken at the initial mark position and four subsequent measured positions. Again singular value decomposition is used to determine the proper feedback linear terms. When the laser feedback is properly calibrated the reference mark will appear to be stationary with the stage moving to different positions. After laser feedback calibration, the nonlinear distortions of the major field are measured and corrected assuming proper laser feedback calibration. Similar to the feedback calibration, an image of a reference mark is first recorded in the center of the field. The stage and deflection are then moved together in a two-dimensional array throughout the field and subsequent images of the mark are taken at each point. The displacement at each point is determined by cross-correlation calculation between the reference image and mark image. When the field distortion is properly calibrated, the displacement at each point should be zero. Finally, the minor field deflection is calibrated against the major field. A reference image is taken of a mark and compared with a set of four images taken with the minor field set to its boundary limits and the major field set to an equal and opposite deflection. When properly aligned the reference mark remains stationary and deviations from the reference location are analyzed to apply corrections to the minor field scaling and rotation terms.

For zone plate exposure, an in-house designed program uses desired zone plate parameters to generate a zone plate pattern in the form of a series of arcs. The arcs are described by their geometric parameters, i.e. by the center and radius of curvature, subtended angle, and the line width. Exposure of the zone plate starts with a transfer of the dataset to C40 parallel array processors^{††}, an essential hardware component in addition to the DPG. The C40s calculate the coefficients a_0 , a_1 , a_2 , b_0 , b_1 , and b_2 in the following pair of parametrized second-order equations:

$$\begin{aligned} x(n) &= a_0 + a_1 n + a_2 n^2 \\ y(n) &= b_0 + b_1 n + b_2 n^2 \end{aligned} \tag{2-8}$$

which are used by the Nanowriter to approximate the desired pattern. In the equations, x and y represent the coordinates of points in the pattern, and n is a non-negative indexing integer for generation of the object. For the zone plate exposure here, the C40s calculate the coefficients by using the mid- and end-points of the arcs. In the process, the C40s keep tracks of various parameters to ensure sufficiently accurate approximation to the arcs by Eq. (2-8). The algorithm, under normal conditions, produces a_2 and b_2 such that the errors from the approximations are smaller than the quantization noise of the electronic circuits⁷⁷. After the computation, the coefficients are sent to the DPG, where they are adjusted for linear scaling, rotation, and orthogonality corrections to the beam deflectors (obtained in the field calibration mentioned above). The DPG next uses a double accumulator circuit⁷⁷ to implement Eq. (2-8) with the adjusted coefficients, in order to define the required beam movement for writing the arcs. Analog signals of the

^{††} The array processors are named after the model name of the digital signal processor modules, TIM-40 TMS320C40, used in the processors.

beam positional values and timing are subsequently sent to the beam deflector and blanker to realize the zone plate exposure.

For zone plate fabrication, we use specially designed micro-zone-plate and condenser-zone-plate substrates. The micro-zone-plate substrate is a 3-inch diameter, 100- μm thick silicon wafer, with a 7x7 array of open windows covered with a low-stress silicon nitride membrane (on the wafer front side). The membrane thickness is 100 nm^{††}, and the window is 70 μm in square. For the condenser zone plates, the substrate is a 4-inch diameter, 500- μm thick silicon wafer, with a single 10 mm square silicon nitride membrane window (on its front side). The window is divided into four quadrants by a silicon cross support frame for robustness [Fig. 2-6]. The silicon nitride membrane has the same thickness as for the micro-zone-plate substrate. These zone plate substrates use a conventional silicon nitride membrane process⁸⁰ for membrane window fabrication.

One of the fabrication processes used for the zone plates studied in the work here [chapter 5] is illustrated in Fig. 2-10. First, a 5 nm thick chromium adhesion layer and a 12 nm thick gold plating base^{§§} are evaporated onto a zone plate wafer [Fig. 2-10 (a)]. An electron-sensitive resist layer is then spin-coated onto the wafer [Fig. 2-10 (a)]. Both positive-tone and negative-tone resists, and chemically amplified resists, have been utilized in various zone plate fabrications [appendix B].

^{††} The membrane absorbs from a few percent to 50% of radiation in the microscope's operating photon range (from 0.3 keV to 2 keV). At 2.4-nm wavelength, where many of the resolution measurements were conducted, the silicon nitride has absorption of 30%.

^{§§} The absorption of the Cr/Au plating base varies from a few percent to 30% in the microscope's operating range.

After the resist coating, the wafer is baked to drive off the resist's solvents. The wafer is then loaded into the Nanowriter, and exposed with 100 keV electrons for zone plate pattern writing [Fig. 2-10 (b)]. The typical beam current is 500 pA. After exposure, the wafer is removed from the Nanowriter. If the resist is chemically amplified, the wafer may then be baked ("post-exposure bake") to activate the chemical reactions necessary for altering the exposed resist. The wafer is then developed and the remaining resist topography exhibits either the exposed zone plate pattern (negative resist) or the pattern's negative (positive resist) [Fig. 2-10 (c)]. In Fig. 2-10, a positive resist is assumed. The wafer may then undergo a "de-scum" process for removing any resist residue in the exposed area (or unexposed area for negative resists). Typically an isotropic low-power dry etch with an oxygen gas mixture is used. The fabricated resist structure is then used as an electroplating mold for forming the final metal zone plate structure. The metal is typically nickel or gold, and the plating is performed to yield a sufficient thickness [Fig. 2-10 (d)]. Pulse plating is used along with proper plating bath temperature in order to obtain low stress metal films with small grains. After plating, the resist structure is removed using a combination of wet and dry etch to yield the final zone plate [Fig. 2-10 (e)].

The single-layer (resist) process was used for fabrication of the micro zone plate, as well as of the condenser zone plates. The resists used for the two types of zone plates are somewhat different, to satisfy different requirements. For the micro zone plates, because the microscope's resolution is determined in large extent by the smallest zone

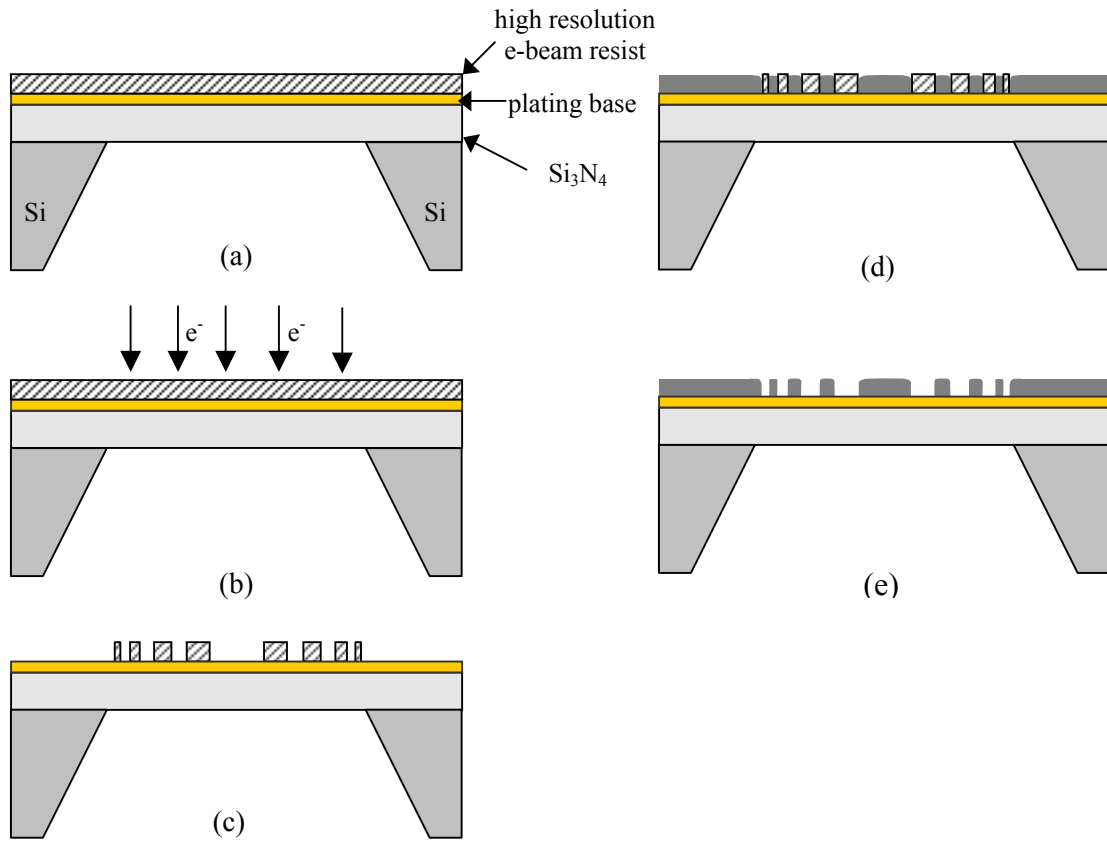


Figure 2-10. One of several common electron beam lithographical processes used for zone plate fabrication used in the work here. This single-layer process was used for the condenser zone plates and early micro zone plates. (a) A plating base and e-beam sensitive resist are coated on top of a 100 nm thick low stress silicon nitride membrane window. In this illustration, positive tone resist is assumed. (b) A zone plate pattern is exposed using the Nanowriter, and (c) the wafer is developed. (d) The pattern is electroplated with gold or nickel, and (e) the resist is removed, leaving the final metal zone plate lens.

widths of the lenses ($\text{Res} = 0.8 \Delta r_{MZP}$), high-resolution e-beam resists are required for obtaining the narrowest achievable zones. It is also required that the high resolution be achieved with a large resist thickness (a few hundred micrometers), in order to obtain

high zone plate efficiency [section 2.4]. However high resolution and large thickness are generally in opposition, due in part to electron scattering and secondary electron generation in the resist, thus limiting the smallest achievable feature sizes. For the fabrication process in Fig. 2-10 for micro zone plates, a thin resist (30-60 nm) is usually chosen for high spatial resolution. Furthermore, sensitivity of high resolution resists is in general modest, but this is acceptable as the micro zone plate lenses are small, generally having diameters of a few tens of micrometers. Typical resists used for the zone plates here include calixarene and hydrogen silsesquioxane [appendix B].

For the condenser zone plates, which are typically 10 mm in diameter, the resist employed needs to have high sensitivity, so that the exposure can be completed in a reasonable time. The required resist resolution, however, is not as demanding as for the micro zone plates, because of the use of partially coherent imaging, with the partial coherence factor, σ , less than 1^{***} . In this σ range, the numerical apertures of the condenser zone plates ($NA = \lambda/2\Delta r$) are smaller than those of the micro zone plates. Thus, the outermost zone widths of the condensers are larger than the ones of the micro zone plate lenses. A commonly used resist is KRS-XE [appendix B].

As discussed above, a high-resolution performance is difficult to achieve with thick resist layers. Aspect ratios^{†††} of 4:1 or larger cannot be easily obtained. This difficulty, however, can be overcome by use of a bi-layer resist process. In this process, instead of using a single resist layer as in the previous zone plate process [Fig. 2-10],

*** The use of partially coherent imaging at the microscope is discussed in chapter 3.

††† Aspect ratio is the ratio of zone thickness to its width.

high-resolution e-beam resist is used in conjunction with a thick polymer layer (a few hundred nanometers) [Fig. 2-11]. The resist, which is above the polymer, continues to act as a recording medium for the electron beam (zone plate) exposure. After development, the resist structure exhibiting a zone plate pattern is transferred into the polymer using a cryogenic plasma etch process [Fig. 2-11 (d)], forming a relatively high aspect-ratio electroplating mold for the formation of the metal zone structure. The bi-layer process enables separation of the e-beam resist thickness from the desired zone thickness, allowing fabrication of high resolution, high aspect-ratio zone plate lenses. The use of a cryogenic plasma etch, in which the zone plate substrate maintained at cold temperature is etched by gases, is significant, because the cold temperature (cryogenic) and gaseous etch chemicals (dry etching) reduce lateral sidewall etching, allowing accurate transfer of the resist pattern into the polymer layer. The bi-layer process has yielded 25 nm zone plates with a 170 nm plating thickness, and was used to fabricate recent micro zone plates, as reported in Appendix B.

Both single and bilayer resist processes described above have been used to successfully fabricate 25 nm micro zone plates. Fabrication of still narrower zones (< 25 nm) is, however, challenging, because of the proximity effect of electron scattering and the resist's resolution. To overcome this limit, an innovative overlay technique that uses semi-isolated lines to realize 15 nm zone plates and smaller has been developed. Details of this new technique are described in chapter 6.

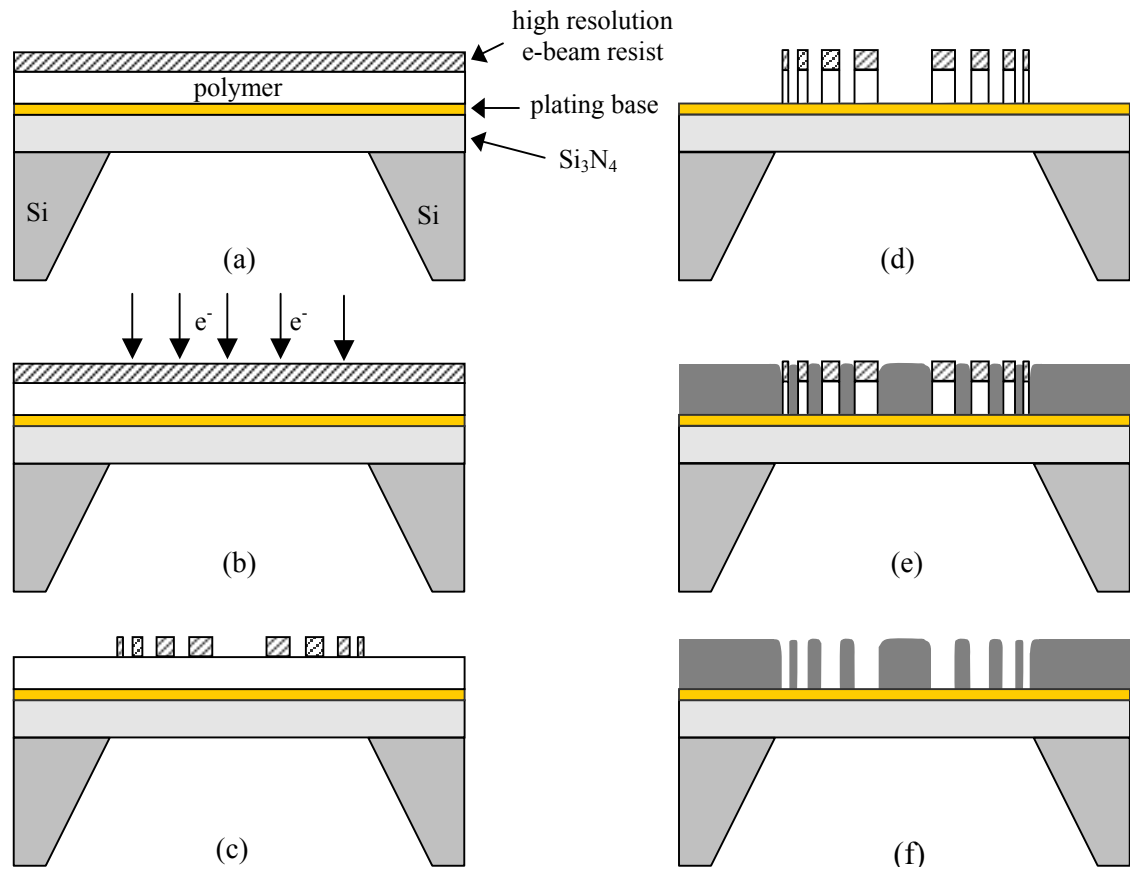


Figure 2-11. Bi-layer zone plate fabrication process. This process separates the e-beam resist thickness from the desired zone thickness, allowing fabrication of high resolution, high aspect-ratio zone plates. The process is similar to the single-layer process in Fig. 2-10, except for the use of a thick polymer layer. (a) A plating base, polymer, and resist are coated on a zone plate substrate. (b) The resist layer is exposed with a zone plate pattern and (c) developed. (d) The exposed pattern is transferred to the underlying polymer layer using cryogenic dry etch processes. (e) The relatively high aspect-ratio plating mold formed by the polymer and resist is used for the formation of the metal zone structure. (f) The resist and polymer are removed using wet and/or dry etch processes, leaving the final metal zone plate lens.

2.6 Conclusion

To conclude this chapter, a unique combination of capabilities of the soft x-ray microscope XM-1, complementary to the ones offered by optical and electron microscopy, are summarized as follows:

1. the highest spatial resolution among all photon based imaging tools;
2. large elemental and magnetic sensitivity, yielding natural imaging contrast;
3. large permissible thickness for nanometer scale objects;
4. in-situ imaging in various conditions (hydration, air, magnetic and electric fields, etc.);
5. exposure time of a few seconds;
6. user friendly operation
7. throughput up to 1000 images per day.

Basic characteristics of zone plates, and the zone plate fabrication used in the work here, have been described. In the next chapter, we will discuss the imaging principle used by the microscope, and in particular, the partially coherent illumination.

Chapter 3

Theory of Image Formation and Partial Coherence

3.1 Introduction

One of the main goals of imaging is to form an image with the highest possible fidelity. In order to understand the limiting factors in meeting this goal at the microscope, fundamental principles of partially coherent imaging, used by the microscope XM-1, is presented in this chapter. As we shall see, the image quality depends on the wavelength, the optical characteristics of the microscope, as well as the object imaged. In comparison to coherent and incoherent imaging, partially coherent imaging can yield the best overall image quality, with the achievable spatial resolution somewhat better than the outermost zone width of the micro zone plate. The effect of partial coherence to the imaging depends on both sample illumination and imaging, and thus in this case on the outermost zone widths of both the condenser and micro zone plates, and is described by the partial coherence factor, σ .

To start the theoretical analysis of the microscope, let us first discuss the importance of spatial coherence to imaging.

3.2 Spatial Coherence in Imaging

For simple illustration of the importance of spatial coherence to imaging, let us consider a single lens imaging setup for a self-luminous object, as depicted by Fig. 3-1.

An object composed of two quasi-monochromatic* point sources is imaged on a screen by imaging optics. Point source A produces a corresponding field disturbance on the screen centered at location Q_A , while source B, situated at a distance d from source A, produces a field disturbance centered at location Q_B .

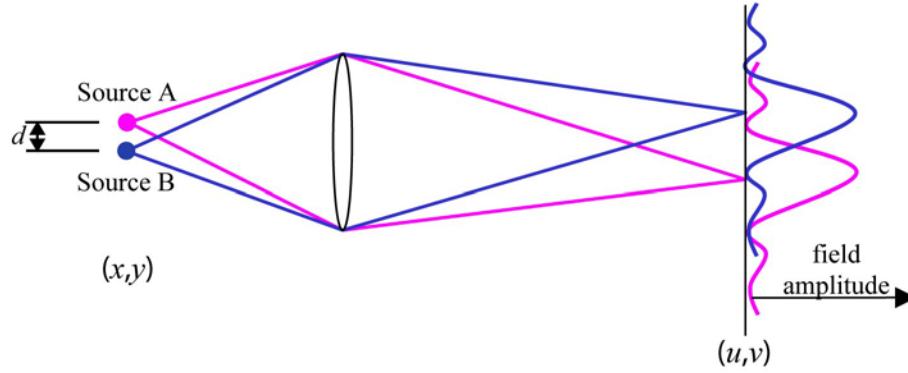


Figure 3-1. A simple single lens imaging setup for self-luminous objects. An image of two quasi-monochromatic point sources is projected by a lens onto a screen. Because of diffraction at the apertures of the optic, each point source has a corresponding field disturbance of a finite spatial extent in the conjugate plane. The diagram assumes circularly symmetry.

Following conventional nomenclature in scalar diffraction theory⁸¹, the field disturbances of quasi-monochromatic point sources A and B are described by the time-dependent phasor amplitude[†] $U^{(A)}(x,y,t) = U(x,y,t)\delta(x-d/2,y)$ and $U^{(B)}(x,y,t) = U(x,y,t)\delta$

* In the quasi-monochromatic condition, the radiation is narrowband, and the coherence length, inversely proportional to the bandwidth, is much greater than the maximum path length difference encountered in passage from the source to the screen. In this chapter, the quasi-monochromatic condition is assumed.

† Complex notation and phasors are commonly used for expressing electromagnetic waves. In the conventional notation, a real-time monochromatic field of frequency ω , $U^{(r)}(P,t)$ is expressed as $A(P)\cos[2\pi\omega t - \phi(P)]$, where $A(P)$ is the field amplitude at position P , $\phi(P)$ is the spatial varying phase, and t is the time. The field can be re-expressed in the complex notation: $U^{(r)}(P,t) = \text{Re}\{A(P)e^{[-2\pi\omega t + \phi(P)]}\} = \text{Re}\{U(P)e^{-2\pi\omega t}\}$, where $U(P) = A(P)e^{\phi(P)}$ is the phasor representation of the field. In the expression, $\text{Re}\{\}$ represents the real part of its parameter. Similarly, a quasi-monochromatic (or polychromatic in general) field, $U^{(r)}(P,t)$, which is the sum of fields in a small bandwidth, can be expressed as:

$(x+d/2, y)$, respectively. In this representation, (x, y) are the coordinates of the object plane, δ is the two-dimensional Dirac delta function, and $U(x, y, t)$ is the general phasor amplitude specifying the field amplitude and phase in the object plane. The two point sources, with combined field disturbance of $U^{(A)}(x, y, t) + U^{(B)}(x, y, t)$, induce a field distribution $U(u, v, t)$ in the image plane (the screen), which is equal to

$$U(u, v, t) = \int_{-\infty}^{\infty} \int_{-\infty}^{\infty} [U^{(A)}(x, y, t) + U^{(B)}(x, y, t)] K(u - x, v - y) dx dy \quad (3-1)$$

where the function $K(x, y)$ is the impulse response, or amplitude spread function, of the imaging optics. For the two point sources here, Eq. (3-1) becomes

$$\begin{aligned} U(u, v, t) &= \int_{-\infty}^{\infty} \int_{-\infty}^{\infty} U(x, y, t) \left[\delta\left(x - \frac{d}{2}, y\right) + \delta\left(x + \frac{d}{2}, y\right) \right] K(u - x, v - y) dx dy \\ &= U\left(\frac{d}{2}, 0, t\right) K\left(u - \frac{d}{2}, v\right) + U\left(-\frac{d}{2}, 0, t\right) K\left(u + \frac{d}{2}, v\right) \\ &= U^{(A)}(u, v, t) + U^{(B)}(u, v, t) \end{aligned} \quad (3-2)$$

where $U^{(A)}(u, v, t) = U(d/2, 0, t)K(u-d/2, v)$, and $U^{(B)}(u, v, t) = U(-d/2, 0, t)K(u+d/2, v)$, are the field disturbances in the image plane produced individually by $U^{(A)}(x, y, t)$ and $U^{(B)}(x, y, t)$, respectively.

$$\begin{aligned} U^{(r)}(P, t) &= \int A(P, w) \cos(-2\pi w t + \phi(P)) dw \\ &= \text{Re} \left\{ \int A(P, w) e^{-2\pi w t + \phi(P)} dw \right\} \\ &= \text{Re} \left\{ \int A(P, w) e^{-2\pi(w - \bar{w})t + \phi(P)} dw e^{-2\pi \bar{w} t} \right\} = \text{Re} \left\{ U(P, t) e^{-2\pi \bar{w} t} \right\} \end{aligned}$$

where $U(P, t) = \int A(P, w) e^{-2\pi(w - \bar{w})t + \phi(P)} dw$ is the phasor representation of the quasi-monochromatic field, with a spectral band centered at frequency \bar{w} .

Since in the scalar theory that intensity $I = \langle UU^* \rangle$, where $\langle \rangle$ and $*$ signify the time average and complex conjugate, respectively, using Eq. (3-2), the resultant image intensity $I(u, v)$ in the image plane is equal to

$$\begin{aligned}
 I(u, v) &= \langle U(u, v, t) U^*(u, v, t) \rangle \\
 &= \langle [U^{(A)}(u, v, t) + U^{(B)}(u, v, t)] [U^{(A)}(u, v, t) + U^{(B)}(u, v, t)]^* \rangle \\
 &= \langle |U^{(A)}(u, v, t)|^2 \rangle + \langle |U^{(B)}(u, v, t)|^2 \rangle + 2 \operatorname{Re} \{ U^{(A)}(u, v, t) (U^{(B)}(u, v, t))^* \} \\
 &= \langle |U^{(A)}(u, v, t)|^2 \rangle + \langle |U^{(B)}(u, v, t)|^2 \rangle \\
 &\quad + 2 \operatorname{Re} \left\{ \left\langle U \left(\frac{d}{2}, 0, t \right) U^* \left(-\frac{d}{2}, 0, t \right) \right\rangle K \left(u - \frac{d}{2}, v \right) K^* \left(u + \frac{d}{2}, v \right) \right\} \quad (3-3)
 \end{aligned}$$

where $\operatorname{Re} \{ \}$ represents the “real part of” its parameter. The first and second terms are, respectively, the intensity from source A and B *individually*. The last term, reduced from the expansion cross terms, is the real part of the product formed by the correlation of the sources’ field disturbances, and the amplitude spread functions at the image positions Q_A and Q_B . The correlation function, referred as the mutual intensity, J_{AB} :

$$J_{AB} = \left\langle U \left(\frac{d}{2}, 0, t \right) U^* \left(-\frac{d}{2}, 0, t \right) \right\rangle \quad (3-4)$$

measures the spatial coherence^{82,83}, of field disturbances from two sources. It, or more precisely the normalized mutual intensity, equal to

$$\mu_{AB} = \frac{\langle U(\frac{d}{2}, 0, t) U^*(-\frac{d}{2}, 0, t) \rangle}{\langle |U(\frac{d}{2}, 0, t)| \rangle \langle |U(-\frac{d}{2}, 0, t)| \rangle} \quad (3-5)$$

describes the definiteness of phase relationship between the fields at the two sources. As we shall see, the mutual intensity and its normalized form, known as the complex coherence factor, play an important role in image formation.

Returning to the intensity calculation, if the point sources are mutually coherent, the mutual intensity J_{AB} can be found by expressing the field disturbance $U(d/2,0,t)$ and $U(-d/2,0,t)$ in terms of the field disturbance $U(x,y,t)$ at the pre-chosen reference point of coordinates (x_0, y_0) . If $U(d/2,0)$ and $U(-d/2,0)$ are defined as the time-invariant phasor amplitudes with respect to $U(x_0, y_0, 0)$, such that

$$U\left(\frac{d}{2}, 0, t\right) = U\left(\frac{d}{2}, 0\right) \frac{U(x_0, y_0, t)}{\langle |U(x_0, y_0, t)| \rangle} \quad (3-6a)$$

$$U\left(-\frac{d}{2}, 0, t\right) = U\left(-\frac{d}{2}, 0\right) \frac{U(x_0, y_0, t)}{\langle |U(x_0, y_0, t)| \rangle} \quad (3-6b)$$

the mutual intensity J_{AB} is equal to

$$J_{AB} = \left\langle U\left(\frac{d}{2}, 0, t\right) U^*\left(-\frac{d}{2}, 0, t\right) \right\rangle = U\left(\frac{d}{2}, 0\right) U^*\left(-\frac{d}{2}, 0\right) \quad (3-7)$$

Hence, the image intensity Eq. (3-3) is equal to

$$\begin{aligned}
I(u, v) &= \left\langle \left| U^{(A)}(u, v, t) \right|^2 \right\rangle + \left\langle \left| U^{(B)}(u, v, t) \right|^2 \right\rangle + 2 \operatorname{Re} \left\{ J_{AB} K \left(u - \frac{d}{2}, v \right) K^* \left(u + \frac{d}{2}, v \right) \right\} \\
&= \left\langle \left| U^{(A)}(u, v, t) \right|^2 \right\rangle + \left\langle \left| U^{(B)}(u, v, t) \right|^2 \right\rangle + U \left(\frac{d}{2}, 0 \right) K \left(u - \frac{d}{2}, v \right) U^* \left(-\frac{d}{2}, 0 \right) K^* \left(u + \frac{d}{2}, v \right) \\
&\quad + U^* \left(\frac{d}{2}, 0 \right) K^* \left(u - \frac{d}{2}, v \right) U \left(-\frac{d}{2}, 0 \right) K \left(u + \frac{d}{2}, v \right) \\
&= \left| U \left(\frac{d}{2}, 0 \right) K \left(u - \frac{d}{2}, v \right) + U \left(-\frac{d}{2}, 0 \right) K \left(u + \frac{d}{2}, v \right) \right|^2 \\
&= \left| U^{(A)}(u, v) + U^{(B)}(u, v) \right|^2 \\
&= \left| U(u, v) \right|^2
\end{aligned} \tag{3-8}$$

where $U^{(A)}(u, v)$, $U^{(B)}(u, v)$ and $U(u, v)$ are the time-invariant phasor amplitudes of $U^{(A)}(u, v, t)$, $U^{(B)}(u, v, t)$ and $U(u, v, t)$, respectively, as defined in a similar manner as for $U(d/2, 0)$ and $U(-d/2, 0)$. Eq. (3-8) states that, the intensity is the modulus square of the resultant phasor amplitude $U(u, v)$ in the image plane induced by the sources, a well known result for coherent imaging. For mutually incoherent point sources, which have fields perfectly uncorrelated,

$$J_{AB} = \left\langle U \left(\frac{d}{2}, 0, t \right) U^* \left(-\frac{d}{2}, 0, t \right) \right\rangle = 0 \tag{3-9}$$

and Eq. (3-3) is equal to

$$\begin{aligned}
I(u, v) &= \left\langle \left| U^{(A)}(u, v, t) \right|^2 \right\rangle + \left\langle \left| U^{(B)}(u, v, t) \right|^2 \right\rangle \\
&= \left| U^{(A)}(u, v) \right|^2 + \left| U^{(B)}(u, v) \right|^2 \\
&= I^{(A)}(u, v) + I^{(B)}(u, v)
\end{aligned} \tag{3-10}$$

The image intensity distribution for mutually incoherent point sources is the sum of the individual intensities from the two sources, $I^{(A)}(u,v)$ and $I^{(B)}(u,v)$.

Fig. 3-2 shows the moduli of individual image (phasor) amplitudes, $|U^{(A)}(u,v)|$ and $|U^{(B)}(u,v)|$, and the resultant normalized intensity, $I(u,v)/I_{\max}$, for the two cases – mutually coherent and incoherent point sources – calculated using Eq. (3-8) and (3-10). In the figure, I_{\max} is the peak intensity in each case, and a circularly symmetric, perfect optical system is assumed.

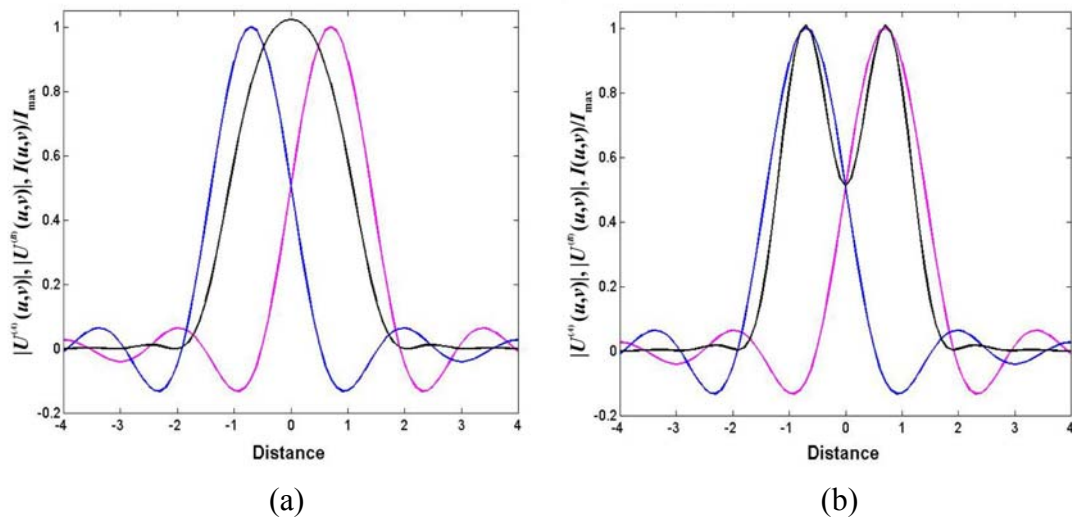


Figure 3-2. Moduli of individual image phasor amplitudes and the resultant normalized intensity in the case of (a) mutually coherent and (b) mutually incoherent sources. The blue and magenta curves are the individual image field amplitudes from the point sources, formed by a circularly symmetry optic. The black line is the resultant intensity. The calculation here assumes separation of the two sources such that the first null of one field amplitude coincides with the peak of the other. In the coherent case, the two point sources are assumed to be in phase.

For the two sources separated by a distance d^\ddagger , such that the first null of $|U^{(A)}(u,v)|$ coincides with the peak of $|U^{(B)}(u,v)|$, as in the case for Fig. 3-2, the resultant intensity distribution in the mutually coherent case shows a single broad peak, while the intensity in the incoherent case exhibits two peaks separated by a trough, with an intensity value at the dip equal to 0.735 of the peak intensity. From the imaging perspective, the two point sources are distinguished in the mutually incoherent case, but clearly not in the coherent one. The drastic difference in the intensity profiles of these cases is resulted from the effect of object's spatial coherence. In the next section, the effect of spatial coherence to the microscope imaging is described.

3.3 Image Formation with Partially Coherent Illumination

In the previous section, the image intensity is calculated for two luminous points, for varying degrees of spatial coherence in the object plane [Eq. (3-3)]. In general, for a transmission imaging system such as the microscope XM-1, the object is illuminated from the back side by a “condenser” optical system (trans-illuminated). In such a case, the image field amplitude, for an object with a transmission profile $F(x,y)$, is given by

$$U(u,v,t) = \int_{-\infty}^{\infty} \int_{-\infty}^{\infty} U(x,y,t) F(x,y) K(u-x, v-y) dx dy \quad (3-11)$$

where $U(x,y,t)$ is the illumination (phasor) amplitude in the object plane, and the coordinates (x,y) and (u,v) refer to the object and image plane, respectively [Fig. 3-1].

Using this expression, the image intensity is found to be equal to

[‡] This distance corresponds to the separation required for two mutually incoherent point objects to be “just resolved” according to the Rayleigh criterion. For details of the Rayleigh criterion, see Ref. 90.

$$\begin{aligned}
I(u, v) &= \left\langle U(u, v, t) U^*(u, v, t) \right\rangle \\
&= \left\langle \int_{-\infty}^{\infty} \int_{-\infty}^{\infty} U(x_1, y_1, t) F(x_1, y_1) K(u - x_1, v - y_1) dx_1 dy_1 \right. \\
&\quad \left. \int_{-\infty}^{\infty} \int_{-\infty}^{\infty} (U(x_2, y_2, t) F(x_2, y_2) K(u - x_2, v - y_2))^* dx_2 dy_2 \right\rangle \\
&= \int_{-\infty}^{\infty} \int_{-\infty}^{\infty} \int_{-\infty}^{\infty} \int_{-\infty}^{\infty} \left\langle U(x_1, y_1, t) U^*(x_2, y_2, t) \right\rangle F(x_1, y_1) F^*(x_2, y_2) \\
&\quad K(u - x_1, v - y_1) K^*(u - x_2, v - y_2) dx_1 dy_1 dx_2 dy_2
\end{aligned} \tag{3-12}$$

where the subscripts 1 and 2 represent two different points in a plane. In the equation, the first term inside the time average is the mutual intensity of the object illumination[§] J_o^- :

$$J_o^-(x_1, y_1; x_2, y_2) = \left\langle U(x_1, y_1, t) U^*(x_2, y_2, t) \right\rangle \tag{3-13}$$

Thus, Eq. (3-12) can be expressed as

$$\begin{aligned}
I(u, v) &= \int_{-\infty}^{\infty} \int_{-\infty}^{\infty} \int_{-\infty}^{\infty} \int_{-\infty}^{\infty} J_o^-(x_1, y_1; x_2, y_2) F(x_1, y_1) F^*(x_2, y_2) \\
&\quad \times K(u - x_1, v - y_1) K^*(u - x_2, v - y_2) dx_1 dy_1 dx_2 dy_2
\end{aligned} \tag{3-14}$$

This is the generalized image intensity formula for an arbitrary degree of illumination coherence. For the special case of fully coherent illumination, $J_o^-(x_1, y_1; x_2, y_2) = U(x_1, y_1) U^*(x_2, y_2)$, as in the previous section, with $U(x_{1,2}, y_{1,2})$ is the time-invariant phasor amplitude of $U(x, y, t)$. Following the same calculation for the coherent case in the previous section, Eq. (3-14) is reduced to [cf. Eq. (3-8)]

[§] The minus sign superscript stresses that the mutual intensity is evaluated in front of the object, which does not include the object transmission function.

$$\begin{aligned}
I(u, v) &= \int_{-\infty}^{\infty} \int_{-\infty}^{\infty} U(x_1, y_1) F(x_1, y_1) K(u - x_1, v - y_1) dx_1 dy_1 \\
&\quad \times \left[\int_{-\infty}^{\infty} \int_{-\infty}^{\infty} U(x_2, y_2) F(x_2, y_2) K(u - x_2, v - y_2) dx_2 dy_2 \right]^* \\
&= \left| \int_{-\infty}^{\infty} \int_{-\infty}^{\infty} U(x_1, y_1) F(x_1, y_1) K(u - x_1, v - y_1) dx_1 dy_1 \right|^2 = |U(u, v)|^2
\end{aligned} \tag{3-15}$$

which is the same conclusion as for the two-point-source object. Eq. (3-15) shows that the coherent imaging is linear in phasor amplitude.

In the case of incoherent illumination, the mutual intensity $J_o^-(x_1, y_1; x_2, y_2)$ can be modeled⁸⁴ by the Dirac delta function, i.e.,

$$J_o^-(x_1, y_1; x_2, y_2) = \kappa U(x_1, y_1) U(x_2, y_2) \delta(x_1 - x_2, y_1 - y_2) \tag{3-16}$$

where κ is a real constant. Substituting Eq. (3-16) into Eq. (3-14) yields

$$\begin{aligned}
I(u, v) &= \kappa \int_{-\infty}^{\infty} \int_{-\infty}^{\infty} U(x_1, y_1) U^*(x_1, y_1) F(x_1, y_1) F^*(x_1, y_1) \\
&\quad \times K(u - x_1, v - y_1) K^*(u - x_1, v - y_1) dx_1 dy_1 \\
&= \kappa \int_{-\infty}^{\infty} \int_{-\infty}^{\infty} |U(x_1, y_1) F(x_1, y_1) K(u - x_1, v - y_1)|^2 dx_1 dy_1
\end{aligned} \tag{3-17}$$

The resultant image intensity, apart from a constant factor, is the sum of intensities from the individual points in the object plane. Eq. (3-17) indicates that (as opposed to the coherent case), the incoherent imaging is linear in intensity.

For partially coherent imaging, such as for the XM-1 microscope, the mutual intensity J_o^- does not take a definite form, and Eq. (3-14) describes the image formation mechanism. Since J_o^- is in general nonzero over some finite region, the imaging mechanism is neither linear in amplitude nor in intensity. Analysis of such imaging is more complicated than that of the coherent and incoherent cases. Before further discussion on this subject, evaluation of the microscope's mutual intensity is described in the next section, and Eq. (3-14), in the context of the microscope, is then analyzed.

3.4 Mutual Intensity in the Object Plane with Critical Illumination and van Cittert-Zernike

Theorem

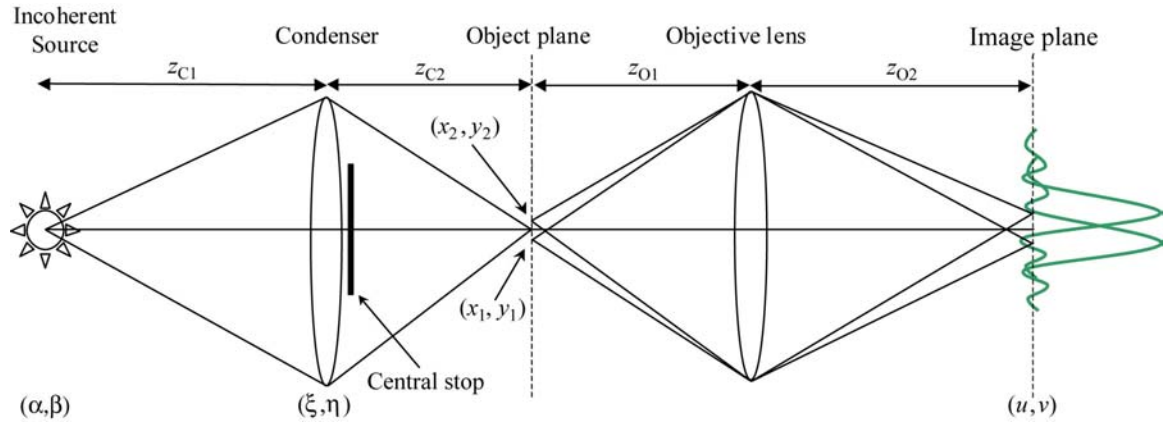


Figure 3-3. Optical setup of the XM-1 microscope. The central stop on the condenser zone plate blocks the radiation from the condenser's central region, making the object illumination hollow-coned. Notations used here are used throughout the remaining sections of the chapter.

Fig. 3-3 shows the optical setup of the XM-1 microscope. The illumination system is mainly composed of a condenser zone plate, which collects relatively spatially incoherent radiation from a bend magnet and projects an image of the source to the object plane. The illumination formed is hollow-coned, with the central illumination blocked by

a central stop [section 2.3]. To determine the mutual intensity at the sample, one can utilize the van Cittert-Zernike theorem^{85,86,82,83}, which states that the mutual intensity J , propagated from a *perfectly incoherent source* with a mutual intensity equal to $\kappa I_s(\alpha, \beta)$ $\delta(\alpha_1 - \alpha_2, \beta_1 - \beta_2)$ [section 3.3], is equal to the Fourier transform of the source intensity profile I_s :

$$J(\xi_1, \eta_1; \xi_2, \eta_2) = \frac{\kappa e^{-j\psi}}{(\lambda z)^2} \int_{-\infty}^{\infty} \int_{-\infty}^{\infty} I_s(\alpha, \beta) e^{j\frac{2\pi}{\lambda z}[(\xi_2 - \xi_1)\alpha + (\eta_2 - \eta_1)\beta]} d\alpha d\beta \quad (3-18)$$

In the equation, $\psi = \frac{\pi}{\lambda z}[(\xi_2^2 + \eta_2^2) - (\xi_1^2 + \eta_1^2)]$, (α, β) is a point in the source plane, and (ξ, η) is a point in the plane where the mutual intensity is evaluated. The separation from the α - β plane to the ξ - η plane is z . The van Cittert-Zernike theorem, if expressed in terms of the complex coherence factor, takes the form of:

$$\mu(\xi_1, \eta_1; \xi_2, \eta_2) = \frac{J(\xi_1, \eta_1; \xi_2, \eta_2)}{J(\xi_1, \eta_1; \xi_1, \eta_1)} = \frac{e^{-j\frac{2\pi}{\lambda z}(\bar{\xi}\Delta\xi + \bar{\eta}\Delta\eta)} \int_{-\infty}^{\infty} \int_{-\infty}^{\infty} I_s(\alpha, \beta) e^{j\frac{2\pi}{\lambda z}(\Delta\xi\alpha + \Delta\eta\beta)} d\alpha d\beta}{\int_{-\infty}^{\infty} \int_{-\infty}^{\infty} I_s(\alpha, \beta) d\alpha d\beta} \quad (3-19)$$

where $\bar{\xi} = (\xi_1 + \xi_2)/2$, $\bar{\eta} = (\eta_1 + \eta_2)/2$, $\Delta\xi = \xi_2 - \xi_1$, $\Delta\eta = \eta_2 - \eta_1$.

For the microscope, where the bend magnet radiation is relatively incoherent, and the paraxial approximation used for yielding Eq. (3-18) is valid, the mutual intensity incident on the condenser zone plate is given by the van Cittert-Zernike theorem, with $z = z_{C1}$ [Fig. 3-3], i.e.,

$$J_c^-(\xi_1, \eta_1; \xi_2, \eta_2) = \frac{\kappa e^{-j\frac{2\pi}{\lambda z_{C1}}(\bar{\xi}\Delta\xi + \bar{\eta}\Delta\eta)}}{(\bar{\lambda}z_{C1})^2} \int_{-\infty}^{\infty} \int_{-\infty}^{\infty} I_s(\alpha, \beta) e^{j\frac{2\pi}{\lambda z_{C1}}(\Delta\xi\alpha + \Delta\eta\beta)} d\alpha d\beta \quad (3-20)$$

with the corresponding complex coherence factor equal to

$$\mu_c^-(\xi_1, \eta_1; \xi_2, \eta_2) = \frac{e^{-j\frac{2\pi}{\lambda z_{C1}}(\bar{\xi}\Delta\xi + \bar{\eta}\Delta\eta)} \int_{-\infty}^{\infty} \int_{-\infty}^{\infty} I_s(\alpha, \beta) e^{j\frac{2\pi}{\lambda z_{C1}}(\Delta\xi\alpha + \Delta\eta\beta)} d\alpha d\beta}{\int_{-\infty}^{\infty} \int_{-\infty}^{\infty} I_s(\alpha, \beta) d\alpha d\beta} \quad (3-21)$$

The mutual intensity J_c , after propagating through the condenser, is found to be equal to

$$J_c(\xi_1, \eta_1; \xi_2, \eta_2) = \check{P}_c(\xi_1, \eta_1) \check{P}_c^*(\xi_2, \eta_2) t_l(\xi_1, \eta_1) t_l^*(\xi_2, \eta_2) J_c^-(\xi_1, \eta_1; \xi_2, \eta_2) \quad (3-22)$$

where $t_l(\xi, \eta) = \exp[-j\pi(\xi^2 + \eta^2)/(\lambda f_{CZP})]$ represents the condenser lens' quadratic phase function, f_{CZP} is the wavelength dependent focal length of the optic, and $\check{P}_c(\xi, \eta) = P_c(\xi, \eta) \exp(-jW(\xi, \eta))$ is the complex pupil function of the lens. The quantity P_c in the complex pupil function \check{P}_c is the condenser's pupil function, which is equal to

$$P_c(\xi, \eta) = \begin{cases} 1 & D_{stop} < 2\sqrt{\xi^2 + \eta^2} < D_{CZP} \\ 0 & elsewhere \end{cases} \quad (3-23)$$

where D_{CZP} and D_{stop} are the diameter of the condenser zone plate and of its central stop, respectively. The quantity $W(\xi, \eta)$ in \check{P}_c represents a slowly varying aberration phase⁸⁷ of the condenser. Substituting these quantities and Eq. (3-20) into Eq. (3-22), J_c becomes

$$J_c(\xi_1, \eta_1; \xi_2, \eta_2) = \frac{\kappa}{(\bar{\lambda} z_{C1})^2} \check{P}_c(\xi_1, \eta_1) \check{P}_c^*(\xi_2, \eta_2) e^{j \frac{2\pi}{\bar{\lambda} z_{C2}} [\bar{\xi} \Delta \xi + \bar{\eta} \Delta \eta]} \times \int_{-\infty}^{\infty} \int_{-\infty}^{\infty} I(\alpha, \beta) e^{j \frac{2\pi}{\bar{\lambda} z_{C1}} (\Delta \xi \alpha + \Delta \eta \beta)} d\alpha d\beta \quad (3-24)$$

where $\frac{1}{z_{C1}} + \frac{1}{z_{C2}} = \frac{1}{f_{CZP}}$ is used [Fig. (3-3)].

In order to obtain the mutual intensity at the sample plane, J_c needs to be propagated from the condenser plane to the object plane. For selecting the proper operation for such propagation, it is useful to estimate the spatial extent of nearly perfect coherence in the condenser plane. For this, we calculate the coherence area⁸⁸, A_c , defined as $A_c \equiv \int_{-\infty}^{\infty} \int_{-\infty}^{\infty} |\mu(\xi_1, \eta_1; \xi_2, \eta_2)|^2 d\Delta \xi d\Delta \eta$. It can be shown that the coherence area of the mutual intensity obtained from the van Cittert-Zernike theorem, is approximately equal to⁸⁸

$$A_c \cong \frac{(\bar{\lambda} z)^2}{A_s} \quad (3-25)$$

where A_s is the source area, z is the distance from the source to the plane of interest, and $\bar{\lambda}$ is the center wavelength of the quasi-monochromatic light. For the coherence area

behind the condenser zone plate, Eq. (3-25) still applies, as spatial coherence cannot be affected by the time-invariant phase transformation induced by the condenser (described by t_l and $\tilde{P}_c(\xi, \eta)$). Thus, for the XM-1 microscope, where the mutually incoherent radiation source has a diameter of 0.10 mm $(3\sigma)^{**}$, and z_{C2} is approximately equal to 17 m, the coherence area on the condenser zone plate is 0.07 mm^2 . This calculation assumes a center wavelength^{††} of 2 nm, which is the common operating wavelength of microscope. The area obtained, corresponding to a diameter of 0.3 mm, represents a small area on a 10 mm diameter condenser zone plate.

Under this condition, illumination from the condenser zone plate can be approximated by a mutually incoherent light source. The intensity distribution of such a “source,” I_c , can be found by setting $\xi_1 = \xi_2$ and $\eta_1 = \eta_2$ in Eq. (3-24), yielding $I_c(\xi, \eta) = \kappa |P_c(\xi, \eta)|^2$. The mutual intensity in the object plane can be calculated using the Van Cittert-Zernike theorem again, which lead to

$$J_o^-(x_1, y_1; x_2, y_2) = \frac{\kappa' e^{-j\frac{2\pi}{\lambda z_{C2}}[\bar{x}\Delta x + \bar{y}\Delta y]}}{(\bar{\lambda} z_{C2})^2} \int_{-\infty}^{\infty} \int_{-\infty}^{\infty} |P_c(\xi, \eta)|^2 e^{j\frac{2\pi}{\lambda z_{C2}}(\Delta x \xi + \Delta y \eta)} d\xi d\eta \quad (3-26)$$

where $\bar{x} = (x_1 + x_2)/2$, $\bar{y} = (y_1 + y_2)/2$, $\Delta x = x_2 - x_1$, $\Delta y = y_2 - y_1$, and κ' is a real constant. Eq. (3-26) shows that the mutual intensity in the object plane is proportional to

^{**} The full width at half maximum of the bend magnet radiation is about 0.05 mm. Assuming the intensity profile of a Gaussian shape, the corresponding standard deviation is 0.02 mm.

^{††} In reality, the radiation in that part of the microscope has a very wide spectrum. However, the bandwidth of radiation reaching the sample plane, after monochromization by the condenser and pinhole, is narrow, with a monochromaticity of 500 to 700 [section 2.2]. Thus, for calculation of the mutual intensity in the object plane, it is reasonable to assume narrowband radiation.

the Fourier transform of the modulus square of condenser pupil function, and is *independent* of any aberrations of the condenser zone plate. The coherence area in the object plane can be found by using Eq. (3-25), with A_s being the area of the condenser pupil function P_c . For a 10-mm-diameter condenser zone plate^{††}, placed 305 mm from the sample plane, with a 5-mm-diameter central stop, A_c is equal to $6 \times 10^3 \text{ nm}^2$ at 2 nm wavelength, corresponding to a diameter of approximately 50 nm at the sample. Thus J_o^- , similar to J_c , is a narrowly peaked function. Note that for a typical z_{c2} value of tens of centimeters, a wavelength of 1 to 2 nm, and a typical field of view of 10 μm diameter, the phase factor $\exp\left[j \frac{2\pi}{\lambda z_{c2}} (\bar{x}\Delta x + \bar{y}\Delta y)\right]$ is close to unity. Hence, J_o^- depends in a large extent on the coordinate difference Δx and Δy .

As a closing remark to this section, it is worth discussing the validity of Eq. (3-26), and the influence of condenser zone plate aberrations on the mutual intensity J_o^- and on the microscope's image formation. In the derivation of Eq. (3-26), the condenser is approximated as a secondary incoherent source, i.e., $J_c(\xi_1, \eta_1, \xi_2, \eta_2) \propto \delta(\xi_2 - \xi_1, \eta_2 - \eta_1)$. While the coherence area in that plane is shown to be small compared to the condenser's dimension, it is not equal to zero as described by the Dirac delta function. Furthermore, even though the illumination bandwidth in the object plane is narrow, broadband radiation propagates from the source to the condenser, and subsequently to the pinhole, just in front of the object plane, where radiation in much narrower band is allowed to pass. A more rigorous calculation [Appendix A] shows that J_o^- is equal to

^{††} These are the parameters for a 60 nm outer-zone-width condenser zone plate used at a wavelength of 2 nm.

$$\begin{aligned}
J_o^-(x_1, y_1, x_2, y_2) = & \int_{-\infty}^{\infty} \int_{-\infty}^{\infty} \int_{-\infty}^{\infty} \int_{-\infty}^{\infty} d\xi_1 d\eta_1 d\xi_2 d\eta_2 \int_{\bar{w}-\Delta w/2}^{\bar{w}+\Delta w/2} \left(\frac{w}{cz_{C2}} \right)^2 G_c^-(\xi_1, \eta_1, \xi_2, \eta_2; w) \tilde{P}_c(\xi_1, \eta_1; w) \tilde{P}_c^*(\xi_2, \eta_2; w) \\
& \times t_l(\xi_1, \eta_1; w) t_l^*(\xi_2, \eta_2; w) e^{-j2\pi \frac{w}{cz_{C2}} (\bar{x}\Delta x + \bar{y}\Delta y)} e^{-j2\pi \frac{w}{cz_{C1}} (\bar{\xi}\Delta \xi + \bar{\eta}\Delta \eta)} \\
& \times e^{j2\pi \frac{w}{cz_{C2}} [\bar{\xi}\Delta x + \bar{\eta}\Delta y + \bar{x}\Delta \xi + \bar{y}\Delta \eta]} dw
\end{aligned} \tag{3-27}$$

where

$$G_c^-(\xi_1, \eta_1, \xi_2, \eta_2; w) = \left(\frac{w}{cz_{C1}} \right)^2 e^{-j2\pi \frac{w}{cz_{C1}} (\bar{\xi}\Delta \xi + \bar{\eta}\Delta \eta)} \int_{-\infty}^{\infty} \int_{-\infty}^{\infty} S_s(\alpha, \beta, w) e^{j2\pi \frac{w}{cz_{C1}} (\Delta \xi \alpha + \Delta \eta \beta)} d\alpha d\beta \tag{3-28}$$

is the cross spectral density⁸² in the condenser plane, S_s is the spectral distribution of source intensity, and \bar{w} and Δw are, respectively, the center optical frequency and bandwidth of the monochromization passband formed by the condenser and pinhole. In Eq. (3-27), the dependence of \tilde{P}_c and t_l on the wavelength, and thus on the optical frequency, is explicitly shown. Note that the condenser's aberrations, included in \tilde{P}_c , play a role in determining the mutual intensity J_o^- .

In addition, because of the highly chromatic nature of zone plate lenses, radiation at undesired wavelengths can be cast into the field of view by the condenser's aberrations, and then captured by the micro zone plate, resulting in out-of-focus radiation at the CCD detector and thus reduced image contrast. Depending on the aberrations of the condenser zone plate, this can have a strong effect on image quality achieved by the microscope.

3.5 Image Formation in the Spatial Frequency Domain and Transmission Cross Coefficient

The partially coherent imaging formula in Eq. (3-14), in combination with the mutual intensity calculation expressed by Eq. (3-26), or more precisely by Eq. (3-27), describes image formation in the microscope. To better understand the microscope's response to various object spatial frequencies, including the effects of mutual intensity and amplitude spread functions, we find it useful to decompose Eq. (3-14) in the frequency domain.

We define the Fourier transform of mutual intensity J_o^- , object transmission function F , and amplitude spread function K as follows:

$$J_o^-(x, y) = \int_{-\infty}^{\infty} \int_{-\infty}^{\infty} \tilde{J}_o^-(f, g) e^{-2\pi j(fx + gy)} df dg \quad (3-29a)$$

$$F(x, y) = \int_{-\infty}^{\infty} \int_{-\infty}^{\infty} \tilde{F}(f, g) e^{-2\pi j(fx + gy)} df dg \quad (3-29b)$$

$$K(x, y) = \int_{-\infty}^{\infty} \int_{-\infty}^{\infty} \tilde{K}(f, g) e^{-2\pi j(fx + gy)} df dg \quad (3-29c)$$

where \tilde{J}_o^- , \tilde{F} , and \tilde{K} , are the transform of J_o^- , F , and K , respectively, and f and g are the spatial frequencies in x and y directions, respectively. For simplicity, we consider the mutual intensity to be given by Eq. (3-26), and J_o^- depends on the coordinate differences as discussed in the previous section. Eq. (3-14), which is then equal to

$$I(u, v) = \int_{-\infty}^{\infty} \int_{-\infty}^{\infty} \int_{-\infty}^{\infty} \int_{-\infty}^{\infty} J^-(x_2 - x_1, y_2 - y_1) F(x_1, y_1) F^*(x_2, y_2) \\ \times K(u - x_1, v - y_1) K^*(u - x_2, v - y_2) dx_1 dy_1 dx_2 dy_2$$

can be expressed using the above definitions as

$$I(u, v) = \iiint \tilde{T}(f', g'; f'', g'') \tilde{F}(f', g') \tilde{F}^*(f'', g'') \\ \times e^{-2\pi j[(f' - f'')u + (g' - g'')v]} df' dg' df'' dg'' \quad (3-30)$$

where

$$\tilde{T}(f', g'; f'', g'') = \int_{-\infty}^{\infty} \int_{-\infty}^{\infty} \tilde{J}_o^-(f, g) \tilde{K}(f + f', g + g') \tilde{K}^*(f + f'', g + g'') df dg \quad (3-31)$$

Eq. (3-30) states that the image intensity is the combined contribution of all spatial frequency components of the object, with each component pairs, $\tilde{F}(f', g') \tilde{F}^*(f'', g'')$, modified by the imaging system function at those particular frequencies. In Eq. (3-30), the object's influence, characterized by F , and the combined effects of illumination (J_o^-) and the projection optic system (K), are separated. The imaging system function, \tilde{T} , referred as the transmission cross coefficient (TCC), represents the system capability in transmitting information regarding particular spatial frequencies of the object. Were the imaging *perfect*, the system function \tilde{T} would be a constant for *all* frequencies, and the image intensity of a uniformly illuminated object (sample) would be given (apart from the constant) by

$$\begin{aligned}
I(u, v) &= \iiint \tilde{F}(f', g') \tilde{F}^*(f'', g'') e^{-2\pi j[(f' - f'')u + (g' - g'')v]} df' dg' df'' dg'' \\
&= F(u, v) F^*(u, v) = |F(u, v)|^2
\end{aligned}$$

which is the intensity in the *object* plane transmitted by the sample. We note that this could also be obtained from both Eq. (3-15) and (3-17) with $K(u - x_1, v - y_1) = \delta(u - x_1, v - y_1)$.

However, no real system of finite wavelength is perfect. For a diffraction-limited system, \tilde{T} is equal to zero at sufficiently high object frequencies. To elaborate on this, we consider a circularly symmetric optical system. As we shall see in the next section, for such a system, $|\tilde{J}_o^-|$ and $|\tilde{K}|$ are equal to (apart from insignificant factors)

$$|\tilde{J}_o^-(f, g)| = |P_c(\bar{\lambda} z_{c2} f, \bar{\lambda} z_{c2} g)| \quad (3-32)$$

$$|\tilde{K}(f, g)| = |P_o(\bar{\lambda} z_{o1} f, \bar{\lambda} z_{o1} g)| \quad (3-33)$$

where P_c and P_o are the pupil functions of the condenser and micro zone plate, respectively. The three functions, $\tilde{J}_o^-(f, g)$, $\tilde{K}(f + f', g + g')$, and $\tilde{K}^*(f + f'', g + g'')$, in Eq. (3-31), are then given by the corresponding scaled pupil functions centered at (0,0), $(-f', -g')$ and $(-f'', -g'')$, in the f - g spatial frequency coordinates, respectively. If the extents of these functions are drawn in the f - g plane, as marked by the three solid circles and a dotted circle^{§§} [Fig. 3-4], the transmission cross coefficient, according to Eq. (3-

^{§§} Note that the pupil function of the condenser P_c is an annulus, with the center blocked by the central stop [Fig. 3-3].

31), is given by the superposition of the three functions in the shaded area, where all the three functions overlap [Fig. 3-4]. For the high spatial frequency components of the object, where f', g', f'' , and g'' are large [Eq. (3-30)], the circles for \tilde{K} and \tilde{K}^* move away from the origin, where \tilde{J}_o^- is centered, and the overlapping area is reduced. This results in a smaller amplitude for \tilde{T} . At sufficiently high frequencies, where \tilde{J}_o^- , \tilde{K} and \tilde{K}^* have no overlapping, \tilde{T} vanishes, and the microscope ceases to transmit any object information to the image.

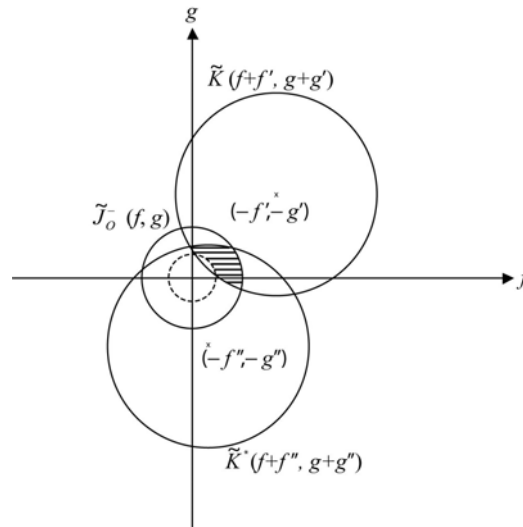


Figure 3-4. Diagram of the frequency extent of the three functions \tilde{J}_o^- , \tilde{K} and \tilde{K}^* in Eq. (3-30).

In the f - g frequency plane, $\tilde{J}_o^-(f,g)$ is given by the scaled pupil function of the condenser, with the center at the origin, while $\tilde{K}(f+g',g+g')$ and $\tilde{K}^*(f+f'',g+g'')$ are given by the scaled pupil function of the micro zone plate, with the centers at $(-f',-g')$ and $(-f'',-g'')$, respectively. According to Eq. (3-29), the transmission cross coefficient is given by the superposition of these three functions in the shaded area, where the functions are nonzero and overlap. As the object frequencies $-f', -g'$ and $-f'', -g''$ increase, the shaded area diminishes,

thus reducing the amplitude of the transmission cross coefficient. Note that the shaded area excludes the area inside the dotted circle, which corresponds to the central stop in the condenser's (scaled) pupil function.

Fig. 3-4 provides an effective means for understanding the microscope's response to various object frequencies, and the roles of the micro zone plate and condenser in determining that response. For a direct view of the microscope's frequency response, we can express the image intensity in Eq. (3-30) by its Fourier transform, i.e.,

$$I(u, v) = \int_{-\infty}^{\infty} \int_{-\infty}^{\infty} \tilde{I}(f, g) e^{-2\pi j(fu + gv)} df dg$$

where from Eq. (3-30)

$$\tilde{I}(f, g) = \iint \tilde{T}(f' + f, g' + g, f', g') \tilde{F}(f' + f, g' + g) \tilde{F}^*(f', g') df' dg' \quad (3-34)$$

Eq. (3-34) shows that the image intensity spectrum is a nonlinear convolution of the transmission cross coefficient and object transmission spectrum.

To end this section, note that the separation of the imaging system function and object function in Eq. (3-30) and (3-34) provides an efficient way for calculating the image intensity for a fixed system configuration, for instance, a particular combination of condenser and micro zone plate. Once the transmission cross coefficient is calculated, the image intensity profiles for different objects can be obtained by use of Eq. (3-30) or (3-34). This advantage is utilized in the computer program SPLAT⁸⁹, developed by

Professor Neureuther's group at UC Berkeley, which numerically evaluates Eq. (3-31) using an adaptive quadrature method and calculates the two-dimensional image intensity profiles for the objects of interest. This program provides accurate simulation of imaging systems with varying degrees of partial coherence and other optical properties, such as objective lens aberrations, at a single wavelength. All calculations of the microscope's response described in this dissertation were obtained with this program.

3.6 Degree of Partial Coherence

As mentioned in section 3.5, \tilde{J}_o^- and \tilde{K} are scaled pupil functions of the condenser and micro zone plates. In the spatial domain, J_o^- is found from Eq. (3-26) to be equal to (apart from a phase factor)

$$J_o^-(\Delta x, \Delta y) = \frac{2}{1 - \varepsilon^2} \left[\frac{J_1(\rho)}{\rho} - \frac{\varepsilon J_1(\varepsilon \rho)}{\rho} \right] \quad (3-35)$$

where J_1 is a Bessel function of first kind, first order, $\rho = 2\pi NA_{CZP} \sqrt{(\Delta x)^2 + (\Delta y)^2} / \bar{\lambda}$, $\varepsilon = D_{stop} / D_{CZP}$, and $NA_{CZP} = D_{CZP} / (2z_{C2})$ is the numerical aperture of condenser zone plate seen from the object side. For the amplitude spread function K , it can be shown, using scalar diffraction theory, that the function K is equal to (apart from a phase factor) the Fourier transform of the object pupil function⁸¹. For the microscope, which uses the micro zone plate as objective, K is equal to

$$K(u - x, v - y) = 2 \frac{J_1(q)}{q} \quad (3-36)$$

where $q = 2\pi NA_{MZO} \sqrt{(u-x)^2 + (v-y)^2} / \lambda$, and $NA_{MZO} = D_{MZO} / (2z_{O1})$ is the numerical aperture of the micro zone plate with diameter of D_{CZO} .

If we suppose that the amplitude spread function K has a linear spatial extent of l . For an arbitrary point, A, in the object plane [Fig. 3-5], the corresponding field disturbance in the image plane have overlapping only with the fields produced by the other object points that are within a distance of about l from point A (for instance, point B

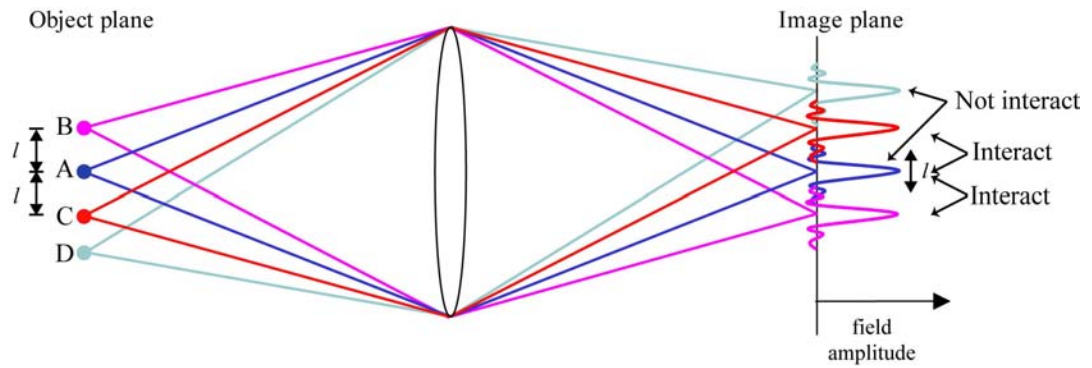


Figure 3-5. Illustration of the significance of the relative extent of J_o^- to the extent of K . If the amplitude spread function K has a spatial extent equal to l , as indicated by the width of the blue peak in the image plane, the field disturbance produced by an arbitrary object point A (blue) can interact with the fields produced by neighboring points that are approximately a distance l from A, such as B and C, but not D. The nature of interaction depends on the spatial extent of the mutual intensity J_o^- . If J_o^- has a distribution much broader than l , the field interaction is coherent. In the case where J_o^- has a distribution much narrower than l , the field interaction may be incoherent. For simplicity this argument assumes a magnification of unity.

and C in Fig. 3-5). In this case, the field from A can only interact with those fields, but not with the fields from farther object points (such as point D in Fig. 3-5). If the mutual intensity J_o^- in the object plane has a spatial extent much broader than l , the interaction of the field disturbances from those points is coherent. On the other hand, if J_o^- is a narrowly peaked function, with the spread much smaller than l , the field disturbances may interact incoherently. Therefore, the relative extent of J_o^- to the extent of K indicates the coherent nature of the imaging.

To be precise, if we define a parameter, σ , as

$$\sigma = \frac{NA_{CZP}}{NA_{MZP}} \quad (3-37)$$

Eq. (3-35) can be expressed as

$$J_o(\Delta x, \Delta y) = \frac{2}{1 - \varepsilon^2} \left[\frac{J_1(\sigma q_{12})}{\sigma q_{12}} - \frac{\varepsilon J_1(\sigma \varepsilon q_{12})}{\sigma q_{12}} \right] \quad (3-38)$$

where $q_{12} = 2\pi NA_{MZP} \sqrt{(\Delta x)^2 + (\Delta y)^2} / \lambda$. Apart from the different definitions of the independent variables q_{12} and the multiplicative factor ε , the two terms in parenthesis are equal to the scaled amplitude spread function. If σ is equal to zero, J_o^- is then reduced to a *nonzero* constant, which corresponds to perfectly coherent illumination. If σ approaches infinity, J_o^- becomes the Dirac delta function, and the illumination becomes incoherent. Therefore, σ represents the degree of partial coherence in an imaging system, and is

referred to the partial coherence factor. For the XM-1 microscope, where zone plates are used at high magnification, σ can be approximated by the ratio of the outermost zone width of the condenser (Δr_{CZP}) to that of the micro zone plate (Δr_{MZIP}).

$$\sigma = \frac{D_{CZP}}{2z_{C2}} \frac{2z_{O1}}{D_{MZIP}} \cong \frac{D_{CZP}}{2f_{CZP}} \frac{2f_{MZIP}}{D_{MZIP}} = \frac{\Delta r_{MZIP}}{\Delta r_{CZP}} \quad (3-39)$$

Before ending this section, it is worth revisiting Fig. 3-4 and applying the definition of σ to the figure. Based on Eq. (3-36) and (3-38), $|\tilde{J}_o^-|$ and $|\tilde{K}|$ can be shown to be equal to

$$\begin{aligned} |J_o^-(f, g)| &= |P_c(\bar{\lambda} z_{C2} f, \bar{\lambda} z_{C2} g)| \\ &= \left| P_o(\bar{\lambda} \sigma \frac{D_{CZP}}{D_{MZIP}} z_{O1} f, \bar{\lambda} \sigma \frac{D_{CZP}}{D_{MZIP}} z_{O1} g) \right| \end{aligned} \quad (3-40)$$

$$\tilde{K}(f, g) = |P_c(\bar{\lambda} z_{O2} f, \bar{\lambda} z_{O2} g)| \quad (3-41)$$

where P_c and P_o are the pupil functions of the condenser and micro zone plates. In Fig. 3-4, the circle^{***} corresponding to extent of \tilde{J}_o^- , has a radius equal to $\sigma NA_{MZIP} / \bar{\lambda}$, while the circles corresponding to \tilde{K} and \tilde{K}^* have radii equal to $NA_{MZIP} / \bar{\lambda}$. Therefore, the partial coherence factor represents the relative extent of \tilde{J}_o^- to those of \tilde{K} and \tilde{K}^* . In Fig. 3-6, σ is assumed to be smaller than unity.

^{***} The dotted inner circle, corresponding to the hollow cone in the illumination, has a radius equal to $\sigma \bar{\epsilon} NA_{MZIP} / \bar{\lambda}$.

3.7 Modulation Response and Resolution of the Microscope

By means of the computer program SPLAT⁸⁹, the microscope's responses to two types of objects – lines and spaces, and sharp edges – are calculated. These patterns are chosen, as they represent two major feature types – periodic patterns and large, isolated features – both often used for testing the microscope. In this thesis we define spatial resolution, to be the half-period of a periodic pattern of lines and spaces that exhibits a 26.5% modulation in its image. This 26.5% modulation is chosen to be equal to that of the Rayleigh criterion⁹⁰, which involves imaging two mutually incoherent point sources with a circular objective (as for the case in Fig. 3-2(b)). Resolution is often expressed^{91,92} as $k_1\lambda/(NA_{MZP})$, which for zone plate imaging at high magnification is equal to $2k_1\Delta r_{MZP}$ [section 2.4]. The microscope's resolution under varying degrees of partial coherence is also discussed below

3.7.1 Periodic Lines and Spaces

Fig. 3-6 shows the microscope's modulation response, under varying degrees of coherence, to equal lines and spaces of different periods. The objects are one directional amplitude gratings, with a square transmission profile varying between zero and one. The calculated image modulation is given by the intensity variation normalized by the maximum intensity, i.e., $(I_{max} - I_{min})/I_{max}$, where I_{min} and I_{max} are the minimum and maximum intensity in the image. The calculations assume a monochromatic radiation at 2.4 nm wavelength uniformly illuminating the object. The illumination is hollow-cone, with ε equal to 0.5 [Eq. (3-35)]. A diffraction-limited micro zone plate of 25 nm outer

zones is assumed in these calculations. Various σ values reflect variations in condenser outer zone widths as given by Eq. (3-39).

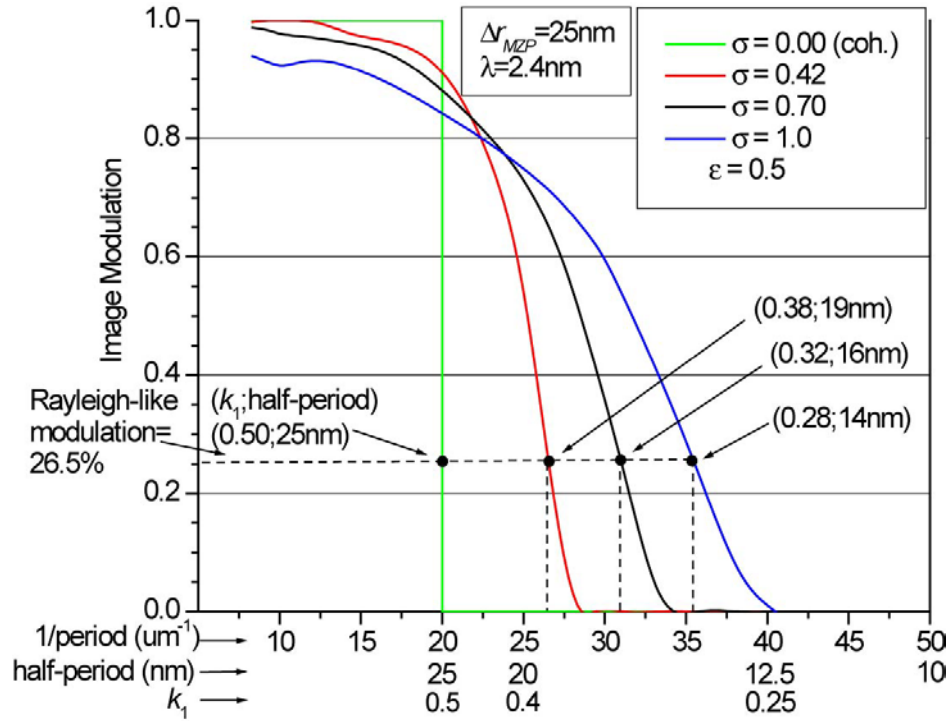


Figure 3-6. Modulation response of the microscope, in varying degrees of partial coherence, to equal line and space patterns. For each partially coherent case, the modulation response equal to the Rayleigh-like modulation of 26.5% is marked by a black dot. The corresponding half-periods, which are defined as the microscope resolutions for those σ values, are expressed in two forms: k_1 values ($\text{Res} = 2k_1\Delta r_{\text{MZP}}$) and half-periods in nanometers. The results here are calculated using the computer program SPLAT, at a wavelength of 2.4 nm. A micro zone plate of 25 nm outermost zone width is assumed for all cases, and condenser outer zone width varies for different σ values according to Eq. (3-37). The calculation assumes a condenser's central stop with a diameter half of that of the condenser zone plate. For the red curve, for instance, with $\sigma = 0.42$, the condenser outer zone width is 60 nm, the theoretical limit to k_1 is 0.38, permitting a periodic pattern of 19 nm lines and spaces to be resolved with 26.5% (Rayleigh-like) modulation.

As seen in Fig. 3-6, for the case of perfectly coherent illumination ($\sigma = 0$), the image modulation of decreasing half-periods is unity until the half-period reaches a value just smaller than Δr_{MZO} , where the modulation abruptly drops to zero (the coherent cutoff). As the illumination becomes less coherent (finite σ), the modulation response extends to higher spatial frequencies (smaller half-periods), with somewhat reduced response for larger features. For σ equal to one, the modulation is reduced but extends to twice that of the coherent ($\sigma = 0$) case.

For equal lines and spaces, values of k_1 , and the corresponding resolution, obtained with various σ values, are indicated in Fig. 3-6. As seen in the figure, for σ equal to zero, the resolution is 25 nm, with a corresponding k_1 value of 0.50. The resolution improves with finite σ values. For σ equal to one, the resolution is 14 nm, with a corresponding k_1 value of 0.28. Hence, with the partially coherent illumination, the resolution^{†††} can be enhanced. For $\Delta r_{MZO} = 15$ as reported in this thesis, coherent illumination permits a resolution of 15 nm, while partially coherent illumination with σ equal to unity (with $\Delta r_{CZO} = 15$ nm) can yield a resolution of $2 \times 0.28 \times 15 \text{ nm} = 8.4 \text{ nm}$.

3.7.2 “Knife Edge”

Another common type of test object is a sharp-edged object, a so-called “knife edge.” Such a test object has the advantages of allowing simple resolution

^{†††} Better resolvability with partially coherent illumination is not only true for lines and spaces, but also for other dense patterns, including two-point objects, which have a similar k_1 dependence on σ .

“quantification” based on a single image (as compared to a series of line and space pattern images for varying periods). Using the computer program SPLAT, the image intensity profiles of a knife edge for varying degrees of partial coherence are calculated

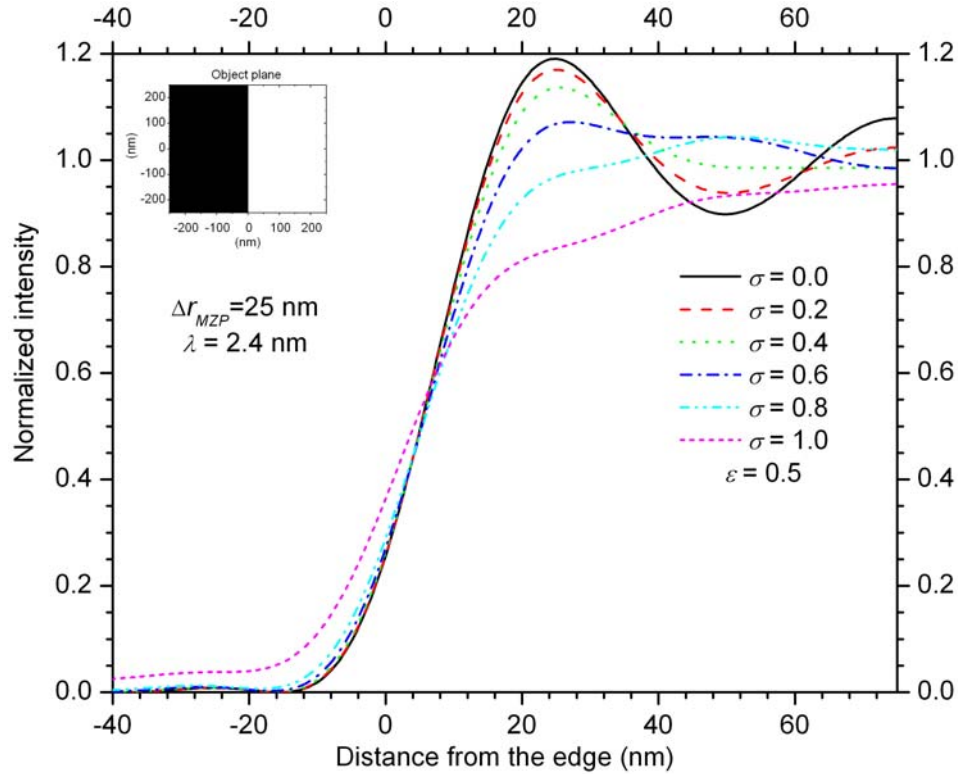


Figure 3-7. Intensity profiles of knife edge images for varying degrees of partial coherence. The calculation assumes a knife edge blocking the left side of the object plane, as illustrated in the inset. For coherent illumination ($\sigma = 0$), the intensity profile has a steep slope and large amplitude of ringing. As the illumination becomes less coherent (finite σ), the edge becomes blurry and ringing reduces. The intensity shown here is normalized to the incident intensity. For all partial coherent cases the intensity converges to unity in the bright region of the image (right side in the figure). The calculations were performed at 2.4 nm wavelength, with the assumption of a 25 nm micro zone plate and a central stop of ε equal to 0.5.

and shown in Fig. 3-7. The calculations assume a knife edge on the left side of the object plane, as shown in the inset of Fig. 3-7. Hollow-cone, monochromatic illumination at 2.4 nm wavelength with ε equal to 0.5 is assumed. In these calculations, a 25 nm micro zone plate is assumed. As seen in the figure, for coherent illumination ($\sigma = 0$), the intensity curve has a steep slope at the edge (the zero position of the horizontal axis), and large amplitude of ringing can be observed at the bright region of the image near the edge. As the illumination becomes less coherent^{†††} (finite σ), the slope decreases slightly, and the ringing reduces and eventually vanishes for $\sigma \geq 0.8$.

As shown in Fig. 3-7, steepness of the slope describes the edge sharpness in the image. The distance^{§§§} over which the image intensity varies from 10% to 90% of its full value (equal to unity in Fig. 3-7) is commonly used to quantify the image quality. This distance, denoted as $d_{10/90}$, depends on the wavelength divided by the numerical aperture of the objective lens (λ/NA_{MZP}), the partial coherence factor (σ), and the objective lens' aberrations. For zone plate imaging at high magnification λ/NA_{MZP} is equal to $2\Delta r_{MZP}$. The dependence of $d_{10/90}$ on the partial coherence factor, calculated for the same optical setup assumed in Fig. 3-7, is shown in Fig. 3-8. The distance is shown in the unit of Δr_{MZP} . For coherent illumination, where the slope is steep [Fig. 3-7], $d_{10/90}$ has the smallest value, $0.71 \Delta r_{MZP}$. As the illumination becomes less coherent (finite σ), $d_{10/90}$ increases, and its value reaches two for σ equal to unity. The curve indicates that

^{†††} As σ increases, the intensity at the bottom (foot) of the intensity curve increases slightly [Fig. 3-7]. The increment, however, is relatively modest, and has insignificant effects to image quality.

^{§§§} In a circularly symmetric system where the illumination is incoherent ($\sigma = \infty$), this distance is equal to the Rayleigh resolution.

relatively coherent illumination (small σ) is best for imaging knife edges, *however* the ringing effect, which can complicate image analysis and is in general undesirable, is severe [Fig. 3-7]. The optimal σ value for sharp-edge objects is between 0.5 and 0.7, depending on the acceptable ringing effect and loss of edge sharpness in the image.

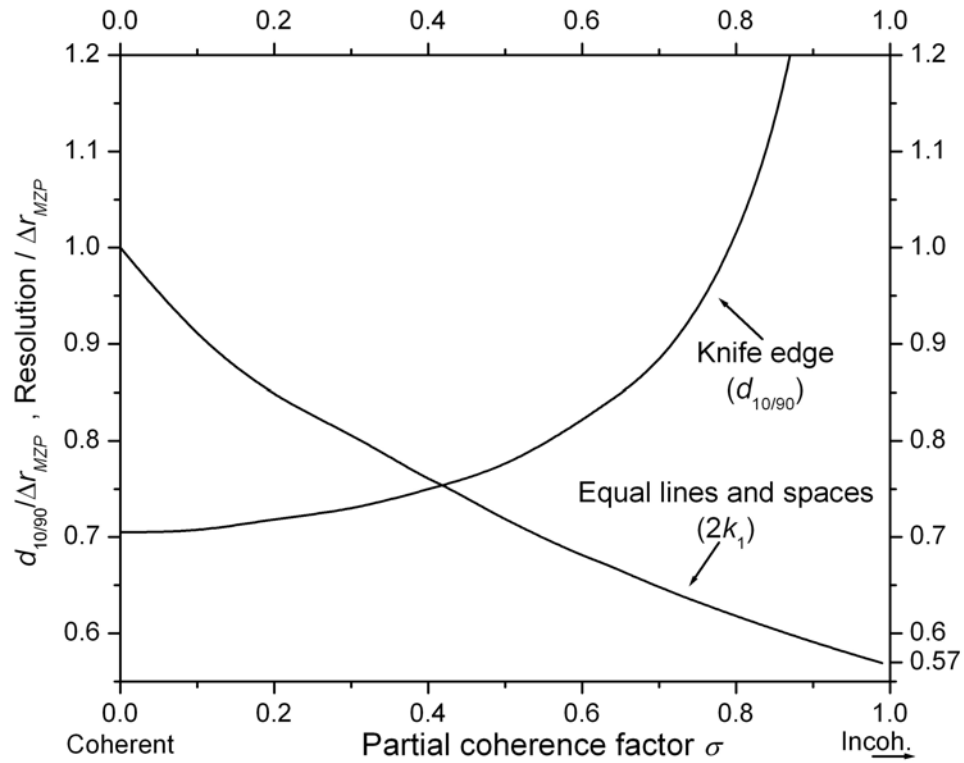


Figure 3-8. The distance for 10% to 90% intensity variation in a knife-edge image, $d_{10/90}$, and the resolution, as a function of σ . Both of the quantities are plotted in the unit of Δr_{MZF} . The graph shows the contrary dependence of $d_{10/90}$ and resolution on the partial coherence factor. Both curves are calculated for a 2.4 nm wavelength, 25 nm outer zone width MZP, and an ε value of 0.5. Note that the resolution in the figure, in the unit of Δr_{MZF} here, is equal to $2k_1$ ($\text{Res} = 2k_1 \Delta r_{MZF}$). Also note that significant ringing near the edge, which is generally undesirable, can be observed in relatively coherent illumination ($\sigma < 0.5$).

Also shown in Fig. 3-8 is the microscope's resolution, calculated^{****} for the same optic, wavelength and ε value as for the knife edge curve. The curve shows that the resolution, in the unit of Δr_{MZP} , which is equal to $2k_1$ ($\text{Res} = 2 k_1 \Delta r_{MZP}$), is equal to unity for σ equal to zero, and it gradually decreases for increasing σ . For the partially coherent illumination of σ equal to unity, $2k_1$ is equal to 0.57 [see Fig. 3-7]. As seen clearly in Fig. 3-8, the dependence of resolution and $d_{10/90}$ on σ is in contrary. Neither coherent nor incoherent illumination can yield better image quality for both line patterns and knife-edge objects. In general, no particular σ value can give the optimal image quality for *all* objects. For an aberration free system, the image quality is a function of the resolving power of the objective lens, illumination coherence, *and* the object characteristics (e.g., geometry and phase distribution). As seen here, the illumination can be optimized for specific types of patterns (such as is done in the semiconductor industry with primary interest in particular types of patterns⁹³). For overall imaging performance, however, σ values from 0.5 to 0.7 should be used⁹⁴.

The object dependence nature of imaging performance has another consequence: besides the arbitrariness in definition, the resolution defined here, or other resolution criteria, such as Rayleigh or Sparrow⁹¹, *cannot* provide an absolute benchmark for imaging systems. A system may yield excellent image quality for a particular object structure, but not for other objects, as seen above. For fair comparison of imaging

^{****} It is the same calculation as for Fig. 3-6.

systems, one should consider, besides the resolution, the nature of the objects and the illumination partial coherence used for obtaining the resolution result.

3.8 Conclusion

In this chapter, the fundamental theory of image formation by a zone plate microscope is reviewed. Image quality is observed to depend on the characteristics of the micro zone plate, the partial coherence factor, σ , which is determined by the CZP and MZP, and the object itself. Partially coherent imaging can yield higher resolution, and in general better image quality with a full-field microscope as considered here. With such imaging, the resolution of the microscope can be better than the outer zone width by about 20%, e.g. $0.8\Delta r_{MZP}$.

In the following two chapters, test objects for characterizing the microscope resolution, and resolution measurement results, are compared with the theoretical calculations as presented here.

Chapter 4

Test Objects for Resolution Measurement

4.1 Introduction

In order to measure the modulation transfer function, or MTF (described in chapter 3), test objects possessing various feature sizes and other desired characteristics are needed. In the first section of this chapter, we will discuss the required and desired test object properties for full characterization of the imaging properties of the soft x-ray microscope, particularly its spatial resolution. The subsequent sections detail the different test object designs, their strengths and weaknesses, and their fabrication.

4.2 Test objects and specifications

As discussed in chapter 3, modulation transfer function, or MTF, describes the spatial frequency response of an imaging system to an object. The goal in quantifying MTF is to measure the imaging system's response to dense or periodic features. One measurement technique collects *individual* MTF data points at various spatial frequencies, by contrast measurement from images of different *discrete, dense* feature sizes. For this methodology applied to the microscope, dense (1:1 lines and spaces) periodic test objects with (1) *well-defined* transparent ("lines") and opaque ("spaces") stripe patterns, and (2) negligible line-edge roughness, are highly desired. This greatly simplifies the image analysis, and reduces uncertainties in actual spatial periods and line-to-space ratios (duty cycle), in forming the MTF. Features with (3) half-periods smaller than the resolution of the microscope are required to quantify the MTF cutoff. In

addition, limited by the CCD detector's dynamic range, the transparent and opaque materials in the objects need to yield (4) acceptably good contrast (e.g. absorption) at the wavelength of interest, to ensure large image contrast between the lines and spaces, the signal, relative to image noise. The objects should also be (5) stable under radiation, and (6) able to be examined or calibrated using high resolution instruments, such as electron microscopes (SEM or TEM).

As the objects above may contain only several discrete spatial frequencies, many test objects may be needed to fully characterize the MTF. A more efficient measurement uses a single (dense) object containing a large range of spatial frequencies^{*}. The objects share similar criteria with those above: possession of a wide range of spatial frequencies including some above the theoretical cutoff, good material contrast, radiation resistance, capable of examination/calibration by other imaging techniques.

In the next section we will describe both types of test objects and compare them against the “ideal” characteristics.

4.3 Test Object designs and fabrication

For the XM-1 microscope with partially coherent illumination, the theoretical spatial resolution and cutoff half-period are slightly less than the outermost zone width of

^{*} At times, one assesses spatial resolution of an optical system based on detection of a blurred signal (such as a faint round peak) from a small isolated object. This inference is misleading, as an object smaller than an MTF's cutoff will cause such a signal in the image, provided that the object spans more than a wavelength and noise in the optical system is low. A proper way to make an inference is to analyze the signal in the frequency domain. For instance, the transfer function of an incoherent system can be measured by the image's power spectrum normalized to the object's. This analytic method will be discussed further in the gold island experiment in chapter 5.

the micro zone plate, about $0.5\Delta r$ to $0.8\Delta r$ depending on the degree of partial coherence and feature geometry in the sample [section 3.7]. For the microscope of interest in this dissertation, features with half-periods from 10 nm to around 60 nm are needed to span a range which goes from nearly 100% modulation to unresolvable (no modulation).

4.3.1. Dense test objects with discrete feature sizes using electron beam fabrication

Fig. 4-1 shows a design drawing of an array of line and space patterns, “elbow” patterns, and isolated lines. Called “XM1TEST,” the test object comprises two sets of lines and spaces, one with a line-to-space ratio of 1:1 (“dense lines”), another with 1:2. Each set has a wide range of spatial periods, in both horizontal and vertical directions.

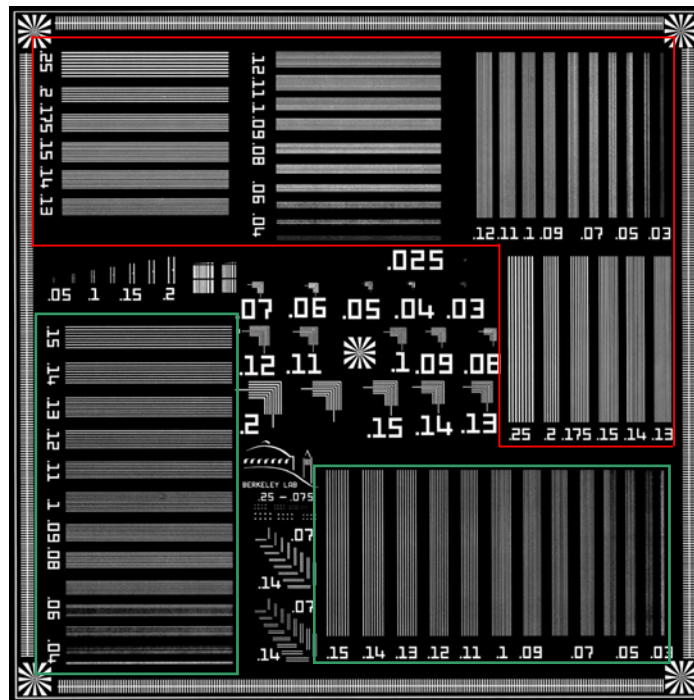


Figure 4-1. A design drawing of the XM1TEST test object. The patterns enclosed by red lines and green lines have line-to-space ratios of 1:1 and 1:2, respectively. The elbows have equal lines and spaces. The numbers adjacent to the patterns represent line widths in microns. The smallest feature has 25 nm equal lines and spaces. The total dimension of the test structure is 120 μm x 120 μm.

Also included are “elbow” patterns, which are sets of lines at right angles separated by different spacings. These patterns are especially useful for recognizing astigmatism in the optics. The finest elbows, which are also the finest patterns in XM1TEST, have 25 nm (equal) lines and spaces.

Test objects of this design were fabricated with the electron beam lithography tool, Nanowriter [section 2.5], in the Center for X-ray Optics’ Nanofabrication Laboratory, the same tool for zone plate fabrication in this dissertation work. The fabrication process is as follows: (1) a plating base of 5 nm Cr / 12 nm Au is formed by evaporation on a 5-mm nonstoichiometric silicon nitride square window. The low-stress nitride membrane is 100 nm thick; (2) 2.5% by wt. 4-Methyl-1-acetoxycalix[6]arene, or Calixarene (TCI America, Portland, OR), is spin-coated on the plating base at 3000 rpm for 45 seconds, and the wafer is baked at 170 °C for 30 min. The resulted resist layer has a thickness of 30 nm; (3) The test object pattern is exposed at 100 keV electron energy, with the Nanowriter; (4) The wafer is developed at room temperature in xylenes for a 30 seconds, followed by 30 second isopropanol (IPA) rinse; (5) The final pattern is formed by electroplating in gold plating solution, BDT 510 (Enthone-OMI Inc., West Haven, CT), at 40 °C, to approximately the resist full thickness; (6) The resist is striped in acetone for 10 minutes, followed by IPA rinse; (7) the wafer is further cleaned by reactive ion etch in oxygen for 3 minutes.

Fig. 4-2 shows an x-ray image of a 30 nm half-period line and space pattern, obtained by a 35 nm micro zone plate at 2.4 nm wavelength. The high pattern quality

achieved by the Nanowriter electron beam lithography tool can be seen clearly in the figure. The pattern quality, however, deteriorates, as the feature size approaches the e-beam lithographic limit. Shown in Fig. 4-3 is an x-ray image of a 25 nm half-period elbow, taken with a 25 nm micro zone plate at 2.4 nm wavelength. Various parts of

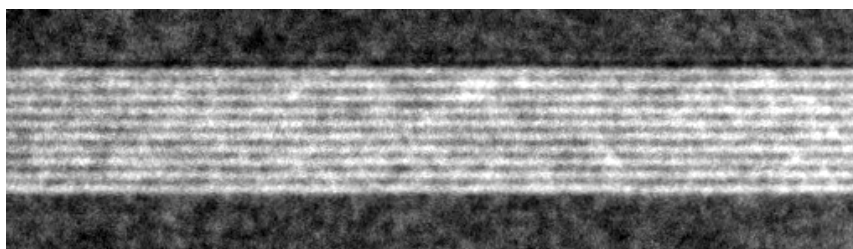


Figure 4-2. An x-ray image of a 30 nm half-period lines and spaces, taken with a 35 nm micro zone plate at 2.4 nm wavelength. It illustrates the high pattern quality achieved by the Nanowriter electron beam lithography tool.

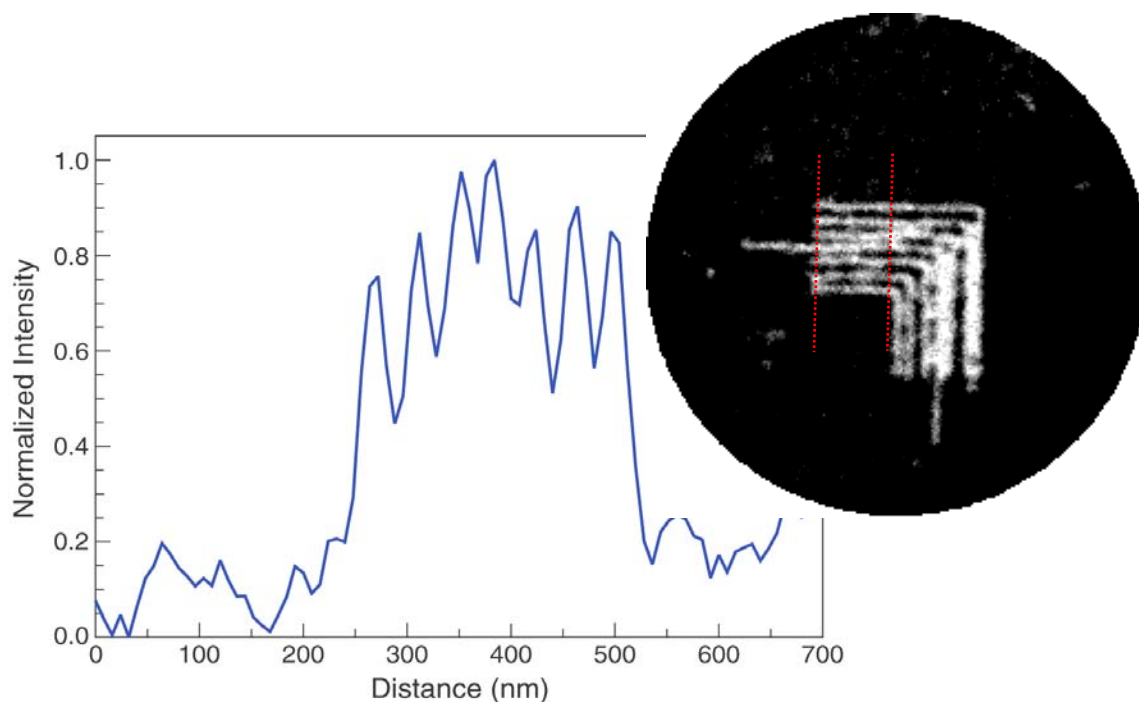


Figure 4-3. An x-ray image of a 25 nm half-period elbow, taken with a 25 nm micro zone plate at 2.4 nm wavelength, is shown at top right. The lineout averaged between the dotted red lines, is plotted.

spaces are broken and line-edge roughness is severe. A lineout plot of the relatively good region, between the two red lines in Fig. 4-3, indicates uncertainty of the contrast measurement. The modulation may be limited by the pattern quality. For accurate contrast quantification in the vicinity of the microscope's resolution, test objects with well-defined, high-quality fine structures, satisfying criterion (1), are highly desired. As the MZP is fabricated with the finest achievable e-beam lithographic lines for the highest possible resolution, high-quality test pattern features made with the same lithographic technique cannot, in general, be smaller than Δr_{MZP} . Furthermore, limited by finite aspect ratio, the ratio of feature height to feature width, in e-beam lithography, test patterns with acceptable material contrast are more difficult to fabricate as Δr_{MZP} shrinks. An alternate test object fabrication is required for contrast measurement around the resolution of the microscope.

4.3.2 Multilayer test objects

Multilayer coatings, alternating layers of two materials of differing refractive indices, have been used extensively as extreme ultraviolet (EUV), and to some extent soft x-ray, reflective mirrors^{19-21,95}. Well-defined bilayer pairs, layer pairs of two materials, with angstrom-scaled roughness and bilayer period control, can be fabricated with magnetron sputtering⁹⁶ with half-periods as small as 5 nm⁹⁷. A variety of multilayer material pairs are also available for sputtering. Test objects made of multilayer coatings in cross section, satisfy criteria (1), (2) and (3) as ideal test objects, with a wide range of materials available to meet the specific needs of resolution tests, such as criteria (4) and

(5) – desired material contrast at a given photon energy and stability to radiation. For instance, test objects used at 600 eV can be composed of two compatible materials, chromium, which is quite opaque above its L_3 absorption edge, and silicon, a fairly transparent element at the energy. Multilayer test objects also satisfy criteria (6) – several inspection techniques, such as angular reflectometry and transmission electron microscopy (TEM), can be used to examine and quantify the layer parameters including bilayer period (d-spacing) and duty cycle.

Using sample preparation techniques developed for transmission electron microscopy⁹⁸, we have created sufficiently thin (10's to 100's nanometers) multilayer test objects for soft x-ray penetration and optimal material contrast. Fig. 4-4 depicts the thinning process. Two narrow strips of multilayer coated wafers, approximately 5 mm by 3 mm, are bonded to each other at the (alcohol-cleaned) multilayer surfaces, using M-BOND 610 adhesive (Measurement Group, Raleigh, NC) [Fig. 4-4(a)]. The strips are clamped tightly and baked at 130 °C for 1 hour. Two silicon blocks, approximately 5 mm by 3 mm by 5 mm thick, are glued on the backsides of bonded strips, using the same process [Fig. 4-4(a)].

The complete structure is secured on a glass slide, with the normal of the multilayer coatings parallel to the glass slide surface, by application of a low melting-point polymer, Crystalbond 509. A low speed wheel saw with a 3" diamond blade (3"x.006"), cuts a slice of 0.5 mm thick [Fig. 4-4(b)], from which a 3-mm-diameter circular disk, with the multilayer at the center, is extracted by a slurry disc cutter (South

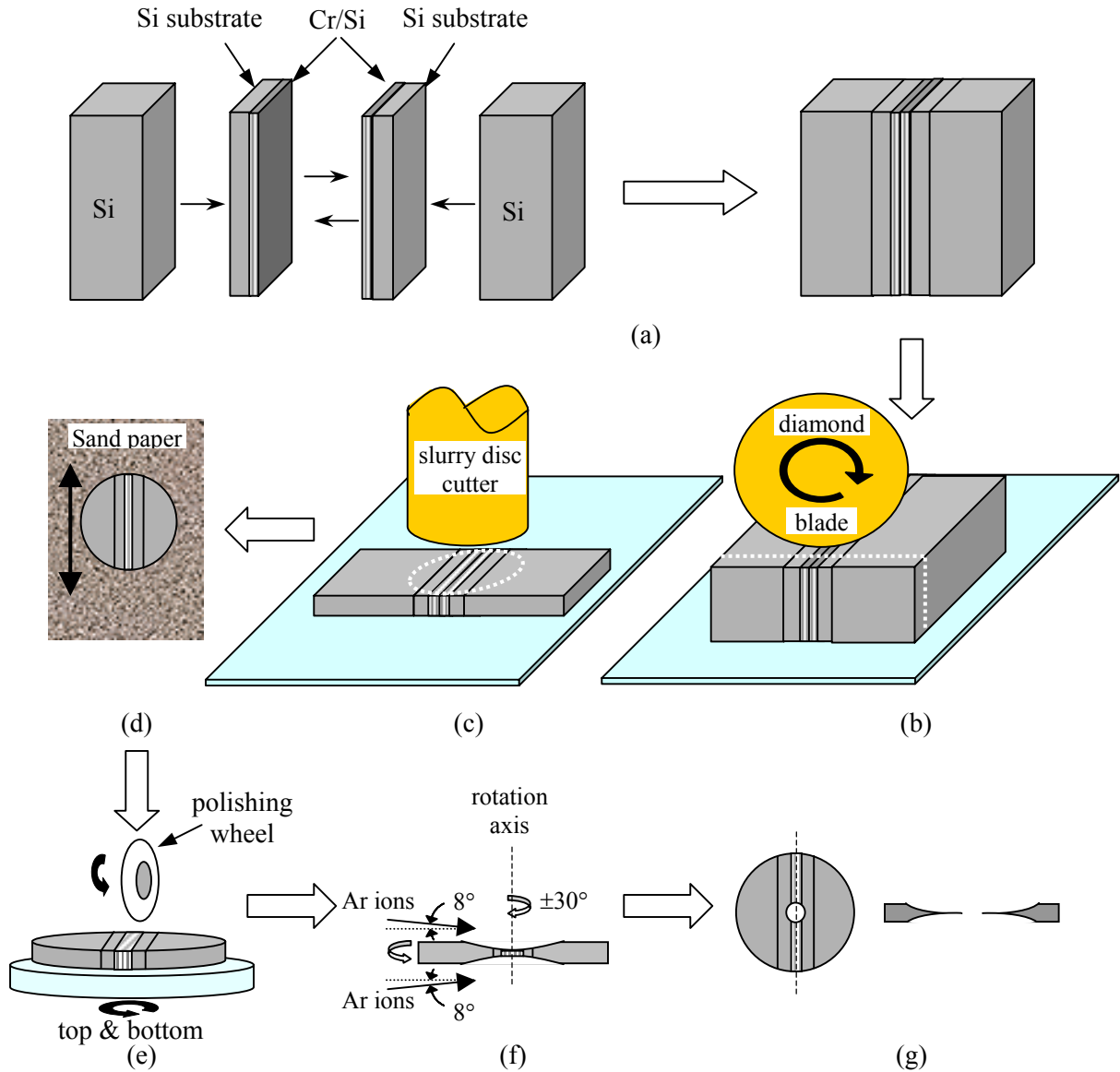


Figure 4-4. Multilayer test objects processed with the TEM sample preparation technique. (a) Two strips of multilayer coating are bonded together, sandwiched between two silicon blocks. (b) A slice of 0.5 mm thick is cut by a diamond blade. (c) A 3 mm diameter disc is extracted from the slice using a slurry disc cutter. (d) The disc is polished with sand paper to 0.2 mm thick. (e) Two concave impressions are formed using a Dimpler[®] on the top and bottom surfaces. The thinnest part, at the impressions' centers is, around 20 μm thick. (f) A shallow wedge thickness profile, with thickness gradually varying from zero to 200 μm , is formed by ion milling. The incidence glancing angle of the argon ions is 8 degrees.

Bay Technology Inc., San Clemente, CA) [Fig. 4-4(c)]. The disk, glued *flat* on a glass slide with Crystalbond™, is polished manually using 400 grit and subsequently 600 grit sand paper, with running water flushing away debris [Fig. 4-4(d)]. The polish motion *must* be parallel to the glue interface, to minimize forces separating the multilayers. The polishing stops when the sample thickness reaches 0.2 mm. The sample is then transferred, and glued with Crystalbond™, to the center of a circular sapphire flat. It is critical for the sample to be mounted parallel to the flat, because otherwise thickness measurement in the next step will be difficult.

The flat is mounted on the turntable of a Dimpler® (Model D500i, South Bay Technology Inc., San Clemente, CA). The sample, covered with a solution of 0.3 mm diamonds, is polished at the center by a rotating Texmat polishing wheel, while the sample is turned [Fig. 4-4(e)]. The polishing wheel rotates at a speed of 300-400 revolutions/min, and applies a 30-gram force on the turning sample, forming a concave impression on the polished surface. The impression typically grows at an average rate of 1 $\mu\text{m}/\text{min}$. The depth of the impression is frequently measured using an optical technique, in which the regions near the edge of the sample, which stays intact in this dimpling process, is viewed through an optical microscope, and the relative focus adjustment required for viewing the lowest point of the impression is used to indicate the impression's depth. Should the unpolished regions have various heights, an average of the heights is used. When the depth reaches a nominal 90 μm , the Crystalbond™ securing the sample is softened by heat, and the sample is turned over, and *re-centered* before being re-secured on the circular sapphire flat. Re-centering the sample is important, as

good alignment of the impressions formed on the two sides ensures that a proper thickness profile will be fabricated. Crystalbond™ should thoroughly occupy the impression on the bottom side, to avoid collapse in this thinnest sample region caused by the pressure of the polishing wheel during the second dimpling step. Residue Crystalbond™ on the top side is removed by manual polishing using 600 grit sand paper. Using the same dimpling condition as described previously, a spherical impression slowly develops on the top side. The depth of impression is frequently measured again using the optical method described above. If this newly formed impression coincides with the one on the bottom side, the sample center has a thickness equal to the difference of the starting sample thickness before dimpling ($\sim 200\text{ }\mu\text{m}$) and the total depth of the two impressions. As the thickness of the thinnest sample region approaches $20\text{ }\mu\text{m}$, the region appears red under a transmission optical microscope. The red color is a characteristic of thinned silicon substrates of the multilayer. The dimpling process stops when the red color is bright and uniform across the sample's center. The sample is removed from the slide, and thoroughly cleaned by submersion in acetone multiple times.

A wedge-shaped thickness profile, with an opening at the sample center, is finally formed by ion milling. Two 5kV argon ion beams, each with a 5 mA current incident sideways on the multilayer interfaces, bombard the top and bottom sample surfaces at a glancing angle of 8 degrees [Fig. 4-4(f)]. The sample oscillates ± 30 degrees in rotation for thickness uniformity. The final test object has a shallow (~ 8 degrees) wedge profile in cross section, with thickness slowly varying from zero to $200\text{ }\mu\text{m}$. The objects are capable of accommodating different transparency needs for imaging and are sufficiently

robust for handling [Fig. 4-4(g)]. For instance, the desired thickness of a Cr/Si multilayer test pattern designed for resolution measurement at 2 nm wavelength is 200 nm, which is well within the thickness range achieved by the sample preparation techniques. The complete thinning sample preparation process, however, is relatively labor intensive and has a low yield. For feature sizes larger than 30 nm, at which high quality patterns can more easily be fabricated using e-beam lithography, the lithographic technique [section 4.3.1] is preferred. Except for difficulties with small feature sizes, the technique is a straightforward fabrication method that provides more flexibility in pattern design (e.g., shape and variation of periods).

4.3.3 A test object possessing a broad, continuous spatial frequency range: Knife edge

A sharp edge contains a large range of spatial frequencies. Such an object allows simple resolution “quantification” based on a single image (as compared to a series of line and space pattern images for varying periods). As discussed in section 3.7.2, the edge sharpness in the image depends on the wavelength divided by the numerical aperture of the objective lens (λ/NA_{MZO}), the degree of partial coherence, and the objective lens’ aberrations. The distance over which the image intensity near the edge varies within a specific range can be used for resolution measurement. However, due to the difference in nature between a knife edge (isolated object) and line and space pattern (periodic object), the dependence of such a distance on the partial coherence factor σ [section 3.6] is different from that of the resolution [section 3.7.2]. For various degrees of partial coherence, different intensity ranges are thus required. Table 4-1 shows the ranges calculated for various σ values. The calculations were obtained by using the computer

program SPLAT⁸⁹, assuming a micro zone plate of 25 nm outer zone widths and a wavelength of 2.4 nm. A condenser central stop of diameter half of that of the condenser zone plate ($\varepsilon = 0.5$) is assumed. For a given σ value, the resolution of an optical system can be characterized by measurement of the distance corresponding to the appropriate intensity range.

$\Delta r_{MZP} = 25 \text{ nm}, \lambda = 2.4 \text{ nm}, \varepsilon = 0.5$		
σ	Intensity range for knife-edge objects	Resolution defined by equal lines and spaces
0.0 [†]	2% to 98%	25 nm
0.63	16% to 84%	17 nm
1.0	30% to 70%	14 nm

Table 4-1. Shown are the intensity variation ranges that give the distances corresponding to the resolution for the same σ value. The intensity ranges are given as the fraction of the intensity far from the edge in the unblocked (bright) region of the image. For instance, for a diffraction-limited system with σ equal to unity, the distance over which the image intensity varies from 30% to 70% is equal to 14 nm, which is the same as the system's resolution as defined by equal lines and spaces [section 3.7]. The results shown above are calculated using the computer program SPLAT. In the calculation, a condenser central stop of diameter half of that of the condenser zone plate ($\varepsilon = 0.5$) is assumed. The intensity ranges for other σ values are listed in Appendix C.

[†] One frequently used resolution definition defines the resolution to be equal to $0.61\lambda/NA_{MZP}$, the Rayleigh resolution, which at high magnification is equal to $1.22\Delta r_{MZP}$. For a 25 nm objective zone plate and σ equal to 0, the intensity range corresponding to this resolution definition for a 25 nm micro zone plate and 2.4 nm wavelength is equal to 1% to 113%. The distance for 10% to 90% intensity variation corresponds to 0.58 of the expected resolution ($1.22\Delta r_{MZP}$), and the distance for 25% to 75% variation corresponds to 0.33 of the expected resolution.

This technique is simple, and is commonly used for resolution characterization of optical systems with various degrees of partially coherent illumination, σ , including the microscope XM-1. The technique, however, demands a well-defined edge on the scale of soft x-ray wavelengths, which is difficult to achieve. In addition, the influence of aberrations on the distance is different from that on the resolution, again due to the different nature of a knife edge and patterns of lines and spaces. Thus this technique is semi-quantitative.

4.3.4 Gold “islands” as test objects

Random gold structures or “islands,” as shown in Fig. 4-5, can also be imaged to acquire the frequency response of the microscope in a single exposure. These structures are formed by annealing a 10 nm thick gold layer, which is evaporated on 100 nm thick silicon nitride membrane windows. After 60 minute annealing in air, the island size with a broad continuous range, from a few to a few tens of nanometers, are yielded. The frequency spectrum of a SEM micrograph of such an object is shown in Fig. 4-6. These test objects are routinely used for calibration of the electron beam lithography tool, Nanowriter, in the Nanofabrication Laboratory [section 2.5].

The ease of fabrication is the advantage of the test object. No lithographic step or low-yield process is required. One drawback, however, is the complexity of the data analysis for obtaining the microscope’s modulation response. Because of the partially coherent nature of the microscope, the power spectrum of a gold island image is a convoluted function of the test object’s transmission function and the microscope’s

transmission cross coefficient. Extraction of the coefficient function is relatively challenging.

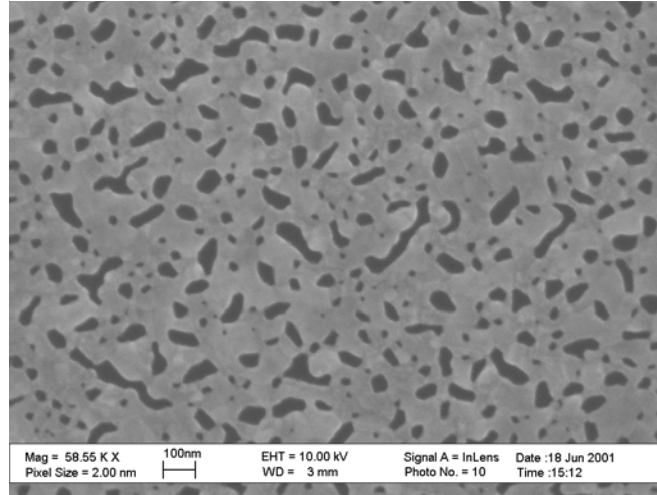


Figure 4-5. A scanning electron micrograph showing gold “islands” structures, which contain a large range of spatial frequencies, down to about 1 nm, but absorb only about 10% of radiation at these small feature sizes.

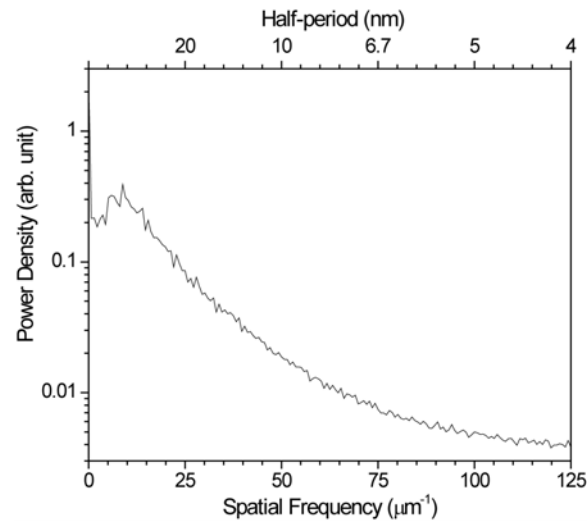


Figure 4-6. The frequency spectrum of a gold “island” test object. For the work here, spatial frequencies from zero to $50 \mu\text{m}^{-1}$ ($\sim 20 \text{ nm}$ period) are of interest. For new state-of-the-art zone plates, fabricated by an overlay technique discussed in chapter 6, small features ($>50 \mu\text{m}^{-1}$) are needed, but would absorb too little in a near-spherical geometry ($< 20 \text{ nm}$ thick).

In addition, the small features in the test object have low material contrast. In the feature sizes of interest, 10-20 nm, depending on the microscope's resolution, the gold islands, which have a sphere-like geometry, also have thickness of about 10 nm. These gold islands typically absorb less than 10% of radiation in the soft x-ray region, yielding an absorption contrast of only 10% at best.

4.4 Conclusion

Desired characteristics and requirements of resolution test objects, and various test object designs used by the microscope have been discussed. The e-beam lithographic test objects provide the desired high-quality lines and spaces for features larger than 30 nm, while the more labor-intensive thinned multilayer test objects are used for pattern features from a few tens of nanometers to a few nanometers. We have used these complementary test objects very successfully for the soft x-ray microscope characterization. In chapter 5, results obtained with these test objects, and the others, are presented.

Chapter 5

XM-1 Microscope Resolution Measurement

5.1 Introduction

In this chapter, resolution characterization of the microscope, with various zone plate designs, is discussed. The test objects described in chapter 4 were selectively used in the characterization, based on the objects' properties and the expected modulation response. Table 5-1 summarizes the strengths and weaknesses of the test objects – e-beam-fabricated dense-pattern, multilayer, “knife-edge”, and “gold-island” test objects. Fabrication of the “knife-edge” and “gold-island” test objects are relatively simple, but they suffer from modest measurement accuracy and difficult data interpretation, respectively. For the dense-patterns and multilayer test objects, fabrication is somewhat sophisticated. However, they allow direct measurement of the modulation response of the microscope.

The expected resolution of the microscope is approximately $0.8 \Delta r_{MZF}$ [chapter 3], from 30 nm to about 20 nm for the zone plates studied in this chapter. As mentioned in the previous two chapters, the spatial resolution here has a specific definition^{*}: it is equal to the half-period of line and space pattern at which the pattern's image exhibits the Rayleigh-like modulation of 26.5%. In the following experiments, the microscope's resolution is measured using this definition.

^{*} The two seemingly different definitions for line patterns and knife-edges are equivalent in incoherent illumination. Readers are encouraged to refer to section 3.1.6 for the detailed discussion of this matter.

Test Objects	Strength	Weakness
E-beam-fabricated dense test objects	<ul style="list-style-type: none"> • High-quality line patterns down to around 25 nm half-periods • Allow flexible pattern design for evaluation of various aberrations, such as astigmatism 	<ul style="list-style-type: none"> • Line quality is compromised for feature sizes smaller than the outer zone widths of MZP, 25 nm here • Negligible line-edge roughness (LER) is difficult to obtain • Limited aspect ratio
Multilayer test objects	<ul style="list-style-type: none"> • High-quality line patterns down to 5 nm half-periods • High aspect-ratio for absorption contrast • Atomic-scaled line-edge roughness • Large material selection 	<ul style="list-style-type: none"> • Labor-intensive and low-yield fabrication • Modulation measurement in one direction, or rotate
“Knife-edge” objects	<ul style="list-style-type: none"> • Simple geometry • Can be fabricated in various ways 	<ul style="list-style-type: none"> • Difficult to obtain straight, sharp edges with low LER • Yield semi-quantitative results
“Gold-island” objects	<ul style="list-style-type: none"> • Contain a broad, continuous spatial frequency range, extending to below the microscope’s resolution cutoff • Frequency response measurement in 2-D • Ease of fabrication 	<ul style="list-style-type: none"> • Low absorption contrast for small, thin features • Difficult to relate these results quantitatively to MTF and a defined resolution.

Table 5.1. Strengths and weaknesses of the four test object types discussed in chapter 4. The test objects were used in the resolution measurement based on their properties and the microscope’s modulation response.

5.2 Resolution measurement of a 35 nm micro zone plates using knife edge test objects

The microscope, installed with a 35 nm micro zone plate and a 54-nm condenser zone plate, was tested with a “knife-edge” test object. This test object was chosen for its apparent ease of realizing the test object and the simplicity of the measurement. The edges of a TEM grid (SPI supplies, Structure Probes, Inc., West Chester, PA) were used as a knife-edge test object. The zone plates[†] studied have these parameters: MZP: $\Delta r_{MZP} =$

[†] Fabrication of these zone plates, as well as the other zone plates discussed in this chapter, is discussed in appendix A.

35 nm, 318 zones, 45 μm in diameter, and 60-nm-thick nickel plating; CZP: $\Delta r_{CZP} = 54$ nm, 41000 zones, 9 mm in diameter, 200-nm-thick nickel. The degree of partial coherence was 0.63, optimal for high resolution imaging for a variety of objects [section 3.7.2].

A portion of the knife-edge image[‡], taken at 2.4-nm wavelength[§] and with a magnification of 2400X, is shown in Fig. 5-1. The projected pixel size, which is the image's pixel size projected back to the image plane, was 10 nm. In the image, the edge is blurred by the limited resolution of the microscope. As discussed in section 4.3.3, the resolution can be found by measurement of the distance corresponding to a σ -dependent intensity range, which is listed in table 4-1 for a few σ values. For the σ value of 0.63 here, the range from 16% to 84% should be used.

In order to quantify the microscope's resolution using the image, the edge profile with low signal noise was determined. This was achieved by first finding the slope of the edge, using linear regression. The intensity profile normal to the edge was then collected along the slope. The result is shown as dots in the graph of Fig. 5-1. In this graph, only data inside the red bracket was used, because in this region the enclosed edge segment was relatively straight and long. One may notice the over-shoot in the profile, which corresponds to the bright band along the edge. The over-shoot is due to coherence effects associated with the illumination. The intensity profile is relatively close to the expected profile, shown by the broken curve in Fig. 5-1, calculated for the optical setup

[‡] A pinhole of 12 μm was used, which was placed 160 μm from the sample plane.

[§] Transmission of the 100-nm-thick silicon nitride membrane and the 5nm-thick Cr/ 12-nm-thick Au plating base is 64% and 70%, respectively, resulting in a total transmission of 50%.

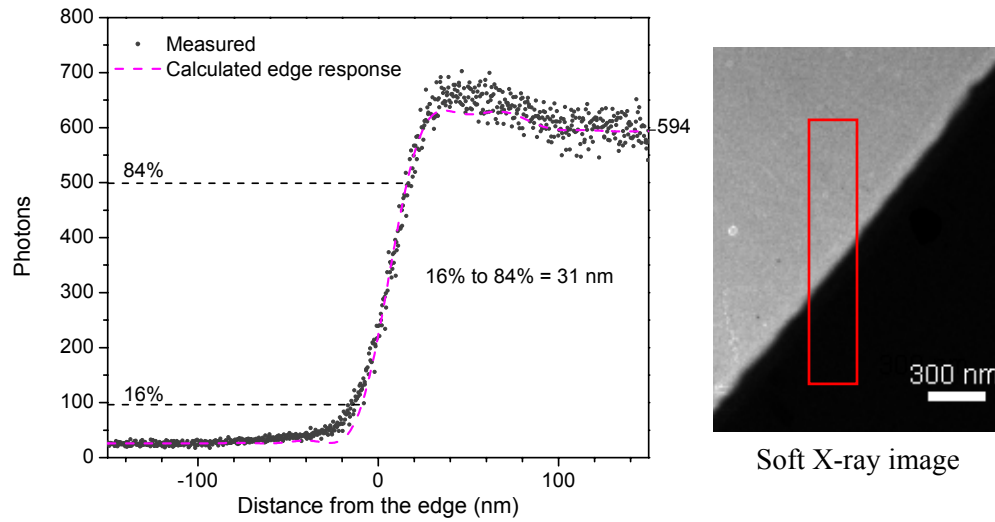


Figure 5-1. Soft x-ray image of the edge of a TEM grid, taken at 2.4-nm wavelength, and the intensity profile (black dots) averaged along the edge section inside the red bracket. A 35 nm micro zone plate ($\Delta r_{MZP} = 35$ nm, $N = 318$, 45 mm in diameter) and a 54-nm condenser zone plate ($\Delta r_{CZP} = 54$ nm, $N = 41000$, 9 mm in diameter) were used. The σ value was equal to 0.63. The theoretical intensity profile for this optical setup was calculated using the SPLAT computer program, and is shown in broken curve above. In this curve the distance between the two points at 16% and 84% of the intensity full value (594 photons here), which is equal to the expected resolution of the microscope, is 24 nm, while the measured intensity profile has a distance of 31 nm for the same intensity variation.

used here. The curve was obtained using the SPLAT computer program⁸⁹, which evaluates the Hopkins theory of partially coherent imaging for desired objects and the microscope's transmission cross coefficient [Eq. (3-31)], using numerical integration (adaptive quadrature). In this case, the object was the sharp edge of a rectangular feature much larger than the expected resolution of the microscope. The calculation assumed monochromatic, hollow-cone radiation, uniformly illuminating the object. In Fig. 5-1, the

calculated line shows that the distance for 14% to 86% intensity variation, equal to the microscope's resolution, was expected to be 24 nm, $0.67 \Delta r_{MZP}$.

To determine the microscope's resolution, the two regions of image's intensity profile near 16% and 84% intensity values (95 photons and 500 photons in Fig. 5-1, respectively) are fitted with two straight lines. The distance corresponding to the 16% to 84% intensity variation was determined to be 31 nm. It is worthy to note that the measurement, however, is sensitive to the quality of the edge profile, including its sharpness, straightness, and roughness. A close examination of the edge used indicated an edge-definition accuracy of a few nanometers. This, combined with the measurements at other edge segments indicated a measurement uncertainty of 31 nm (+3 nm/−6 nm).

Explanations of the discrepancy between the experimental the theoretical intensity profile and resolution are not clear at present. One possible cause is the imperfection of the micro zone plate, including the aberrations. In particular, the zonal roughness, which can induce small-angle scattering, could spread small but noticeable amount of radiation to the surroundings, possibly leading to a small footing at the bottom of the intensity profile [Fig. 5-1]. Moreover, as seen in Fig. 5-1, the edge is not completely perfect. Imperfections such as insufficient sharpness and edge roughness can easily disturb the intensity profile of the image. The quality of the edge, unfortunately, was not possible to be evaluated due to the lack of landmarks in the object.

The experiment here shows the requirement of high quality knife-edge test objects for accurate resolution measurement. In general, the defects should be on the scale of x-ray wavelengths, which is difficult to achieve. Also note that the modulation response of the microscope cannot be extracted easily from the measurement data.

5.3 Qualification of micro zone plates with 25 nm outer zone width using gold-island objects

To improve the microscope's resolution beyond that described in the previous section with 35 nm outer zone widths, zone plates with outer zone widths of 25 nm were successfully fabricated [Appendix B]. Fig. 5-2 shows the scanning electron microscope (SEM) micrograph of one of the 25 nm zone plates.

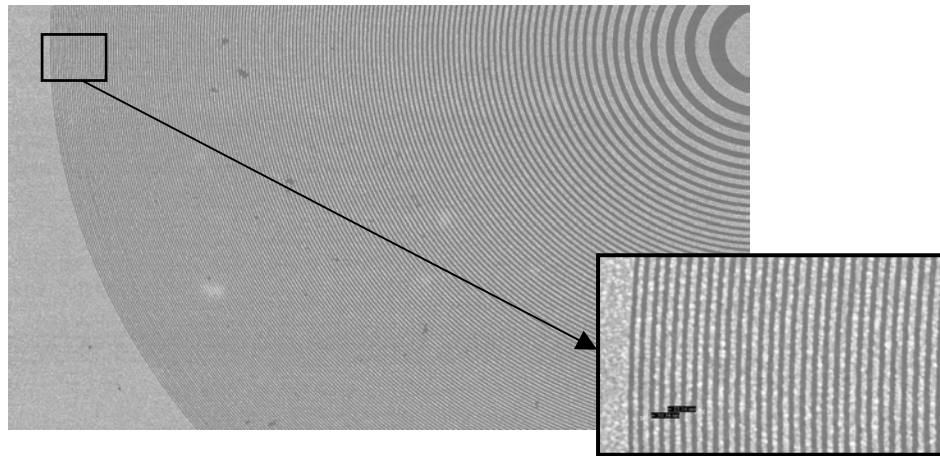


Figure 5-2. A scanning electron micrograph of a 25-nm micro zone plate. The micrograph shows an excellent zone placement, negligible line edge roughness, and a zonal duty cycle of about 50%. In the micrograph, the plating, which is gold, is bright, and the empty zones are gray. The zone plate lens had 628 zones, a diameter of 63 μm , and a gold thickness of 30 nm.

For preliminary characterization, the microscope, installed with one of the 25 nm MZPs and the 54 nm CZP used in the previous experiment, was tested with a “gold-island” test object, composed of agglomerated gold, which was formed on a low-stress silicon nitride membrane window under annealing. The fabrication process details of the test object are discussed in section 4.3.4. Fig. 5-3 shows the soft x-ray image and SEM micrograph of the gold-island object. The x-ray image was taken at a wavelength of 2.4 nm, and a magnification of 3100X. The σ value produced by the optics was equal to 0.45. The SEM image was obtained at 10 keV using a LEO 1560 scanning electron microscope (Carl Zeiss SMT AG, Oberkochen, Germany), with an in-lens secondary electron detector. The electron energy was chosen to obtain good contrast with gold. The typical resolution of the scanning electron microscope with the in-lens detector was about 3 nm, at 10 keV. For both the x-ray and SEM images, the projected pixel sizes were 8 nm. Note that they were taken at different locations. This, however, did not affect the analysis, as the dimensional distribution of the islands was uniform over the object due to the randomness of the gold islands.

To obtain the power spectrum of the two images, the images were first Fourier transformed. Fig. 5-4 shows the two-dimensional power spectrum of the x-ray image. This spectrum is a function of the test object’s transmission profile and the microscope’s transmission cross coefficient (TCC), as described by the partially coherent imaging formula [Eq. (3-14) and Eq. (3-30)]. The spectrum distribution was circularly symmetric, indicating that circularly asymmetric aberrations such as astigmatism were insignificant. The noise spectrum outside the microscope’s cutoff, which was calculated to be 17 nm, is

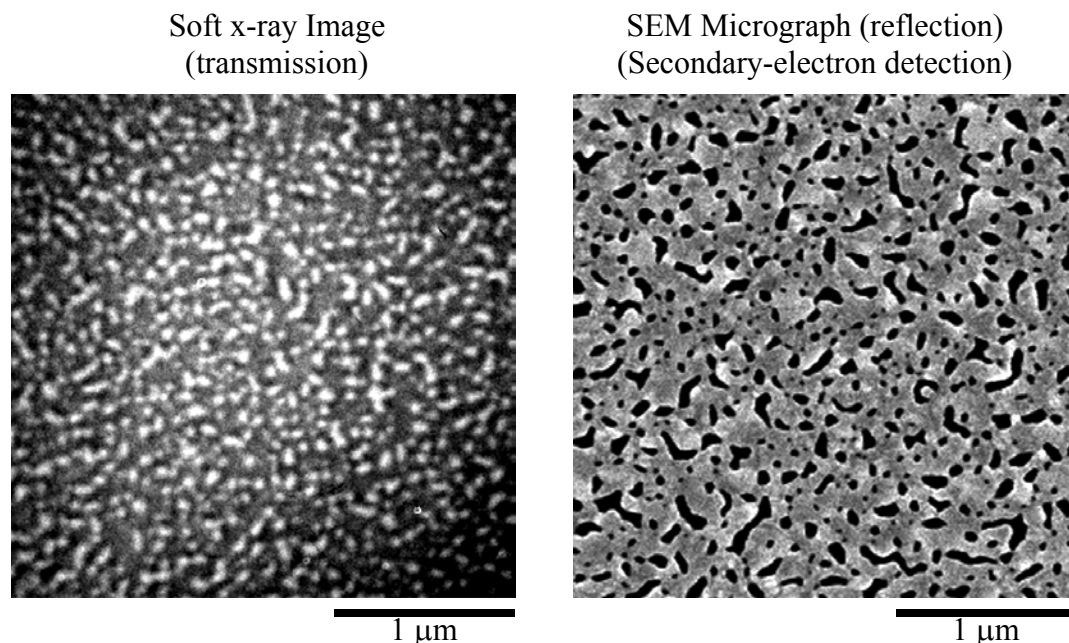


Figure 5-3. The gold “island” pattern was chosen for measurement of the frequency response of the XM-1 microscope. Shown above are the soft x-ray and SEM images of the gold pattern. The images were not taken at the same location. The x-ray image was obtained at 2.4-nm wavelength. The micro zone plate used had a 25 nm outer zone width, 628 zones, a diameter of 63 mm, and the condenser was the same as in the last experiment (section 5.2), yielding σ equal to 0.45. Gold islands of characteristic lateral dimensions of 10 nm to 200 nm are seen in the SEM.

flat, similar to the white noise distribution. To improve the signal to noise, this spectrum was averaged along the circumferences of circles centered at the zero-frequency component. The result is shown in Fig. 5-5 (left). The spectrum has been subtracted by a constant offset, determined by the power densities outside the microscope’s cutoff. For the SEM image, a power spectrum was also obtained by radial averaging, and was fitted with polynomials to eliminate fluctuations in the spectrum. No noise correction was performed at the spectrum.

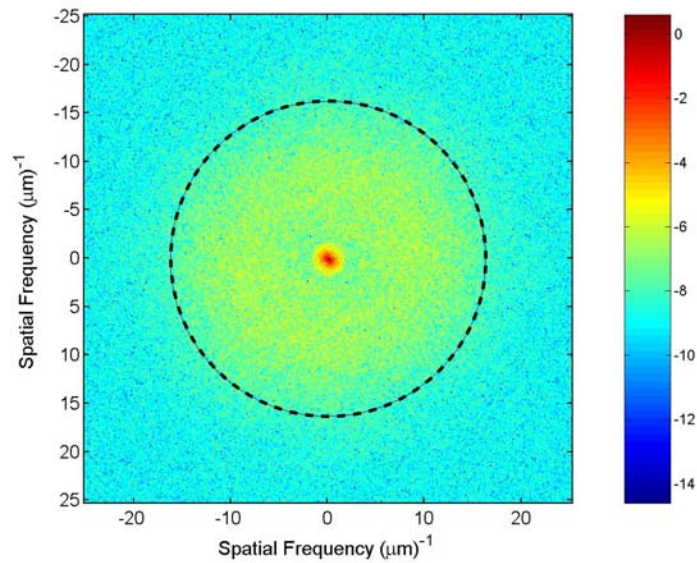


Figure 5-4. Two-dimensional power spectrum of the x-ray image. A circle (black dotted), centered at the zero-frequency (DC) component of the spectrum, is also shown as a reference. The circularly symmetric power distribution indicates insignificant circularly asymmetric aberrations, such as astigmatism in the x-ray microscope. The scale at the color bar is the natural logarithmic values of the power densities.

Assuming the power spectrum of the SEM image to be the true spectrum of the pattern, a normalized frequency response of XM-1 was obtained by dividing the power spectrum of the soft x-ray image by that of the SEM image, as shown in Fig. 5-6. If the microscope is spatially incoherent, i.e., its response is linear in intensity, the frequency response is equal to the microscope's optical transfer function (OTF)^{**}. The normalized response shows that XM-1 had a 10% response to 25-nm half-period features. Note that the actual response might be larger, because the SEM power spectrum used included the noise power in the micrograph.

^{**} For an incoherent imaging system, the image intensity distribution in the Fourier space is the product of the system's optical transfer function and the object's transmission profile in the Fourier space.

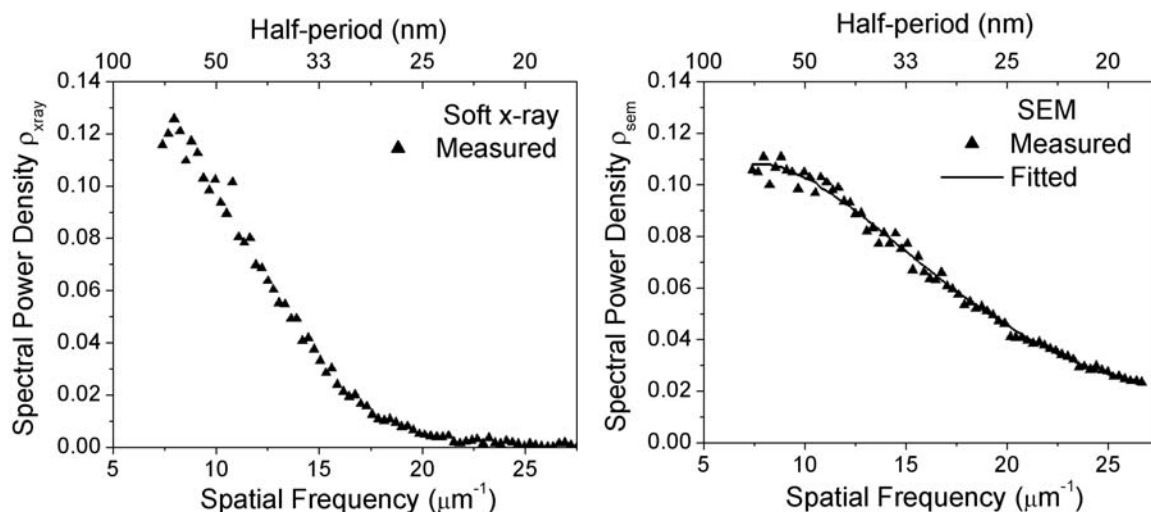


Figure 5-5. The power densities of the x-ray image (left) and the SEM micrograph (right). Both densities were obtained by averaging along the circumferences of circles centered at the zero-frequency component. A white noise distribution has been subtracted from the power densities of the x-ray image. For the SEM micrograph, the densities were fitted with polynomials to eliminate fluctuations in the data.

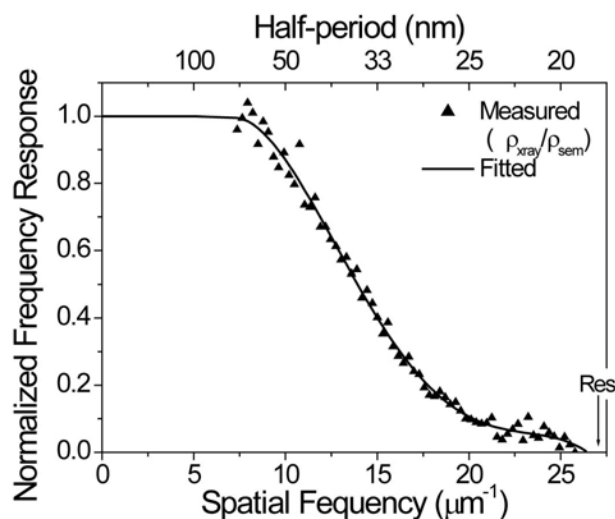


Figure 5-6. The normalized frequency response, obtained by dividing the power density of the soft x-ray image (ρ_{xray}) by that of the SEM image (ρ_{sem}), is plotted as a function of spatial frequency (bottom axis) and half period (top axis). The expected resolution of the microscope, calculated using the computer program SPLAT, is 19 nm, and is marked by an arrow in the figure.

The gold-island technique used here is somewhat qualitative. The normalized response is only an approximation of the microscope's true response function, the transmission cross coefficient. In addition, the in-lens secondary electron detector used for collecting the micrograph, was sensitive to the topography of the gold islands, not their thickness. The different detection mechanism of the detector from the x-ray microscope (absorption) might affect somewhat the result obtained here. Transmission electron microscopy, which relies on scattering of electrons by the imaged object, may be a more accurate reference for this experiment. In the near future, transmission electron micrographs of the gold-island test object will be collected, and the microscope's transmission cross coefficient will be obtained by deconvolution processes of Eq. (3-31) or Eq. (3-14).

5.4 XM-1 Resolution measurement with line test patterns

For more quantitative measurement, the XM-1 microscope with zone plates discussed in the previous section ($\Delta r_{MZP} = 25$ nm, $\sigma = 0.45$) was further characterized, using a test object containing a series of periodic lines and spaces, similar to the XM1TEST3 object [Fig. 4-1]. The test object contained line patterns at different periods and duty cycles, with the smallest dense (1:1 line-to-space) line patterns at a half-period of 20 nm. It was fabricated on a 100-nm-thick low-stress silicon nitride membrane window using the Nanowriter e-beam lithographic tool, the same tool used for all the zone plate fabrication [section 2.5]. To increase the fabrication parameter tolerance (process latitude) for achieving high quality dense features, dense lines of 20 nm, 25 nm and 30 nm half-period were biased – they were drawn as 4 nm – to compensate for the

electron beam broadening due to electron scattering and generation of secondary electrons (proximity effect)^{††}. The final line pattern structures, were made of 40-nm-thick gold plating. The test object fabrication is described in appendix A.

Fig. 5-7 shows the x-ray images of the 25-nm-half-period (15 nm lines/35 nm spaces,) and 30-nm-half-period (15 nm lines/45 nm spaces) line patterns, at 2.4-nm wavelength and with a magnification of 3100X. The test pattern linewidths were quantified by scanning electron microscopy. The images' pixel size, projected back to the object plane, is 8 nm. The micro zone plate used for obtaining these images was a 25-nm-outer-zone-width zone plate lens, from the same batch as for the zone plate lens in the previous “gold-island” measurement experiment. The condenser zone plate used had the similar parameters as in the previous measurement, $\Delta r_{CZP} = 54$ nm, $N = 41000$, 9 mm in diameter, 180-nm-thick nickel. The partial coherence factor of the microscope, σ , achieved with these optics was 0.45.

In Fig. 5-7, the scanning *transmission* electron micrographs of the 25-nm- and 30-nm-half-period test patterns are included for comparison. Transmission mode, rather than secondary electron detection mode, was utilized, because the imaging mechanism involved, based on electron scattering, may be a better approximation to the diffraction/absorption imaging mechanism the XM-1 microscope uses. The pixel size of the micrograph is 8 nm. Note, however, the micrographs and the x-ray images might not be taken from the same locations due to the lack of “landmarks” on the object. For each

^{††} This is the limiting factor in fabrication of dense features. Proximity effect is discussed further in chapter 6.

x-ray image, the line scan was averaged along the patterns to reduce signal's noise, and the result is shown next to the image. Fig. 5-7 also shows the averaged lineout of a large feature, 100 nm lines/100 nm spaces.

The normalized lineouts for the 15 nm lines/35 nm spaces, 15 nm lines/45 nm spaces, and 100 nm lines/100 nm spaces yielded measured modulations of 39%, 70%, and 93%, respectively. All were well above the Rayleigh-like modulation of 26.5%, and thus well within the microscope's resolvability^{††}. Fig. 5-8 shows the experimental modulations as a function of the spatial frequency of the patterns. The theoretical cutoff of the microscope, which was determined by the numerical apertures of the KZP and MZP, was 17 nm in half-period. Along with the assumption that large features would have near-perfect modulation, the data points were fitted with a numerical curve. The curve indicated that the Rayleigh-like modulation was at a half-period of 23 nm, i.e., the microscope with a 25-nm-outer-zone-width lens had a resolution of 23 nm.

For comparison, the calculated MTF of the microscope was obtained using the SPLAT computer program. Here, the objects used were periodic, equal lines and spaces^{§§}, with a rectangular transmission profile. The calculation assumed monochromatic, hollow-cone radiation, uniformly illuminating the object. The calculation result is shown as broken curve in Fig. 5-8. The calculated modulations for 25 nm, 30nm, and 100 nm lines and spaces are 90%, 96%, and 100%, respectively. A

^{††} Line pattern images with some modulation, but less than 26.5%, are not resolved by the microscope, according to the resolution definition.

^{§§} For accurate MTF simulation, the duty cycles of the objects should be used in the calculation. However, the errors due to the use of equal lines and spaces here were within the accuracy of the modulation measurement.

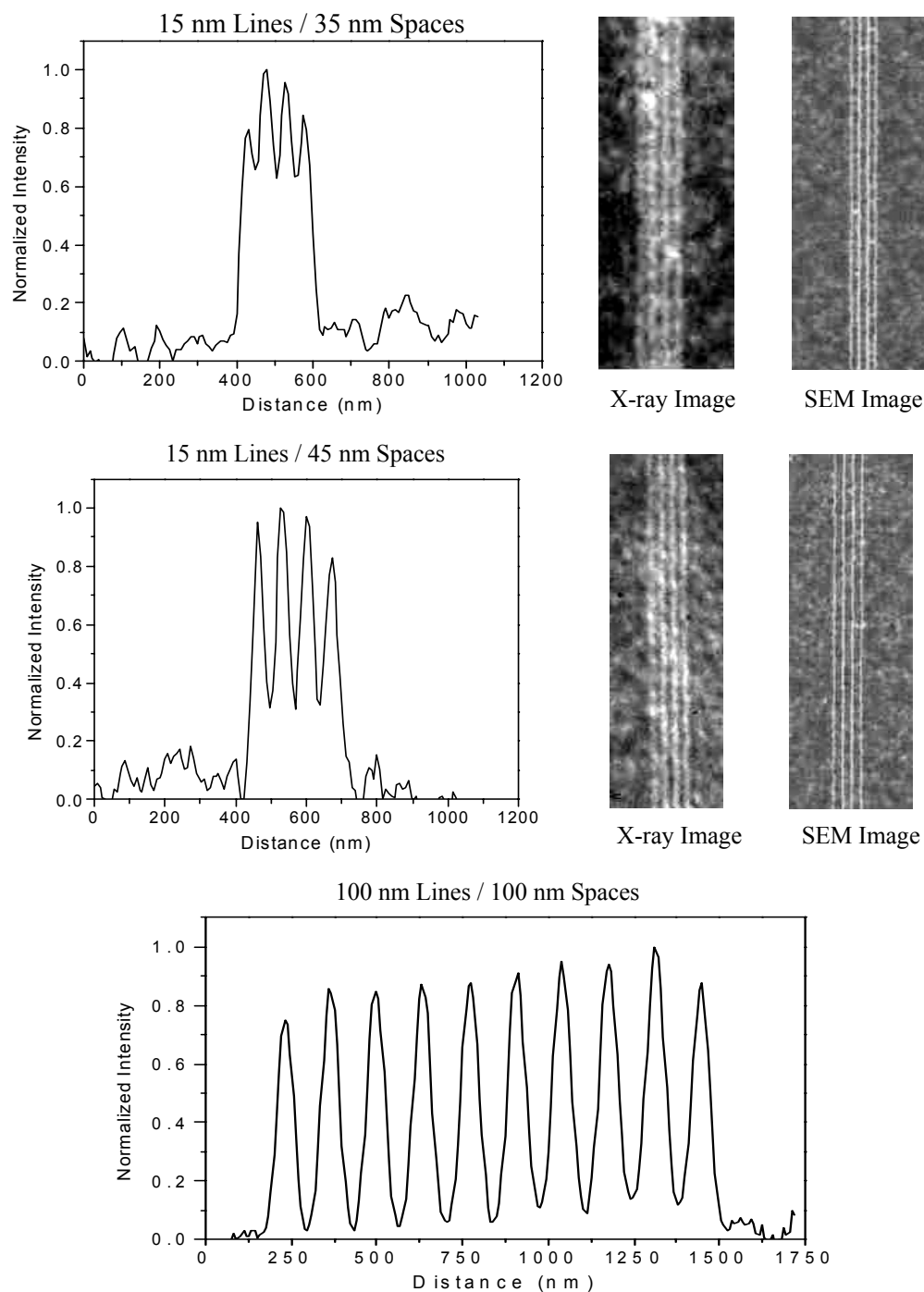


Figure 5-7. X-ray images and scanning transmission electron micrographs of lines and spaces with different periods. The images were obtained at 2.4-nm wavelength, with a 25-nm micro zone plate and a 54-nm condenser zone plate ($\sigma = 0.45$). The pixel sizes of the images, as well as the micrographs, are 8 nm. The test objects were fabricated using the Nanowriter e-beam lithography system, which is also used for the zone plate fabrication. The images and micrographs might not be taken at the same location.

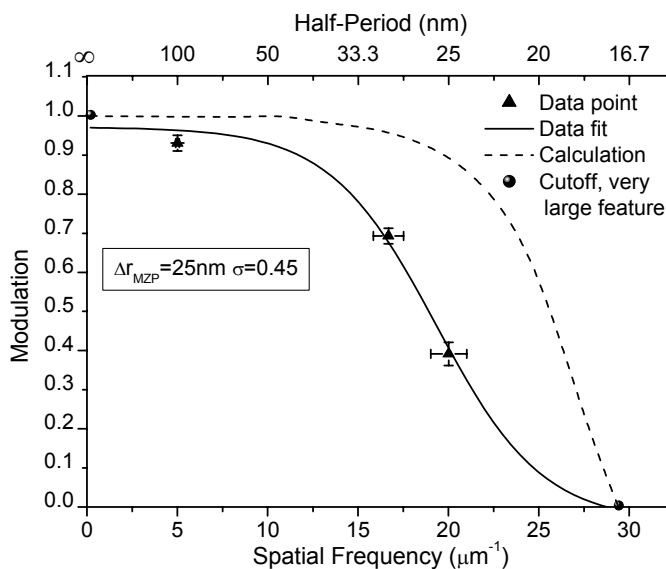


Figure 5-8. Experimental modulation at different periods. Also shown is the calculated cutoff (half-period of 17 nm) of the microscope. The solid line is a least squares fit to the experimental data, the cutoff, and an assumed value of unity at zero spatial frequency. The dashed line is a calculated MTF of the microscope, based on the optics' parameters and the partial coherence factor. The fit and the calculated curve show a measured and expected resolution of 23 nm and 18 nm, respectively.

resolution of 18 nm was expected for the microscope with the 25 nm lens and σ equal to 0.45.

There are a few possible causes for the discrepancy between the expected and measured modulations and resolution. The pinhole used in the monochromator was 18 μm in size, larger the ones normally used in resolution measurements and microscope operations. The large pinhole might reduce illumination control, allowing acceptance of stray light and light at unwanted wavelengths by the micro zone plate. This would result

in faint light patches in the CCD plane, as well as excessive chromatic aberration of the micro zone plate, both of which reduced the image modulation. Furthermore, the test patterns, in particular the 15 nm lines/ 35 nm spaces, had low quality line-definition – severe linewidth fluctuation and line edge roughness, bridges across spaces, and grainy electroplating – as seen in Fig. 5-9. These test pattern defects can be expected to reduce measured modulations, thus underestimating achieved resolution. We thus conclude that the test patterns' quality must be improved near the resolution limit of the microscope. There is room for electron beam lithography to improve. However, dense line patterns from 25 nm to 30 nm half-period are close to the limit of the lithography technology used at that time to fabricate both the lens and the test patterns. Alternate test objects were deemed to be required and are discussed in the next section.

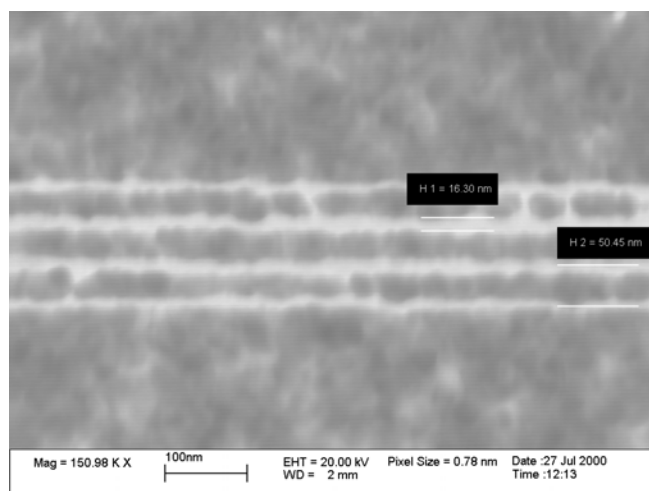


Figure 5-9. Magnified scanning transmission electron micrograph of the 15 nm line/35 nm space pattern. The micrograph shows the relatively poor line definition of the pattern at the feature sizes near the limits of fabrication used for both the zone plates and the test patterns.

5.5 Resolution measurement using multilayer test objects

In section 5.4, due to insufficient test object quality at the critical limits of resolution, the resolution measurement had a significant uncertainty in determining the microscope's optical performance. To more accurately quantify the microscope's resolution, new multilayer test objects [section 4.3.2] were employed. These multilayer test objects were composed of forty chromium/silicon bilayer pairs¹⁹, with half-periods of 15 nm, 20 nm, and 25 nm. They were fabricated using the techniques discussed in section 4.3.2. The coatings were deposited* on 500- μm -thick silicon wafers by an in-house magnetron sputtering system⁹⁹. Using angular reflectivity scan¹⁰⁰ with Cu K_{α} x-rays ($\lambda = 1.54\text{\AA}$) at grazing incidence, their periods were measured to be 30.1 nm, 39.0 nm, and 48.6 nm, respectively, with errors of ± 0.3 nm. Their duty cycles were about 50% (equal thickness). The final test objects, formed after polishing and thinning [section 4.3.2], had a wedge-shaped thickness profile, with thickness varying from zero to 200 μm .

Using these multilayer test objects, the microscope with a 25-nm micro zone plate (300 zones, a diameter of 30 μm , and 80-nm-thick nickel plating) and 60-nm condenser zone plate (41700 zones, 10-mm diameter, and 120-nm-thick nickel plating) was characterized[†]. The degree of partial coherence, σ , was equal to 0.41. A photon energy of 600 eV ($\lambda = 2.07$ nm)[‡], just above the Cr L_2 absorption edge, was selected for good material contrast in testing the microscope with these test objects. The optimal thickness for imaging contrast, modeled by the ratio of differential transmission between Si and Cr

* The sputtering argon pressure was 1.0 mTorr and the wafers were 1.5 inches from the sputtered targets.

† A pinhole of 10 μm was used and placed 300 μm from the sample plane.

‡ Transmission of the 100-nm-thick silicon nitride membrane and the Cr/Au plating base on the micro zone plate was 74% and 70%, resulting in a total transmission of 50% at 600 eV photon energy.

to photon noise as seen in Fig. 5-10, was calculated to be 217 nm[§]. Figure 5-11 (a) shows a soft x-ray image of the 24.3 nm half-period multilayer test pattern, taken with a magnification of 5800X. The image is similar in quality to the SEM micrograph^{**} of the pattern, as shown in Fig. 5-11 (b). Both the x-ray image and micrograph have equivalent 4 nm pixels when projected back to their respective object planes. To obtain a lineout of the x-ray images with minimal noise, multiple x-ray images were combined and averaged along the pattern. The resultant lineout, shown in Fig. 5-11 (c), exhibits a normalized modulation of 75%.

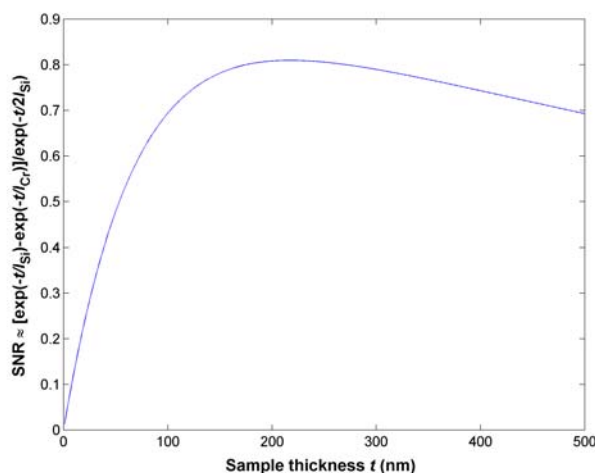


Figure 5-10. The imaging signal-to-noise ratio (SNR), approximated by the differential transmission between Si (absorption length l_{Si}) and Cr (absorption length l_{Cr}) divided by the square root of the transmission of Si, which is more transparent, is calculated for varying sample thickness t , at 600 eV. The optimal thickness for imaging contrast is 217 nm. At this thickness and a 600 eV photon energy, Si has transmission of 72.8%, Cr of 3.70%. Phase effects are negligible (less than 2°). In the calculation here, known refractive indices¹⁰¹ of Si and Cr were used.

[§] At this thickness and a 600 eV photon energy, Si has transmission of 72.8%, Cr of 3.70%. Phase effects are negligible (less than 2°).

^{**} The micrographs in this section were obtained with an in-lens detector, using secondary electrons generated at the sample.

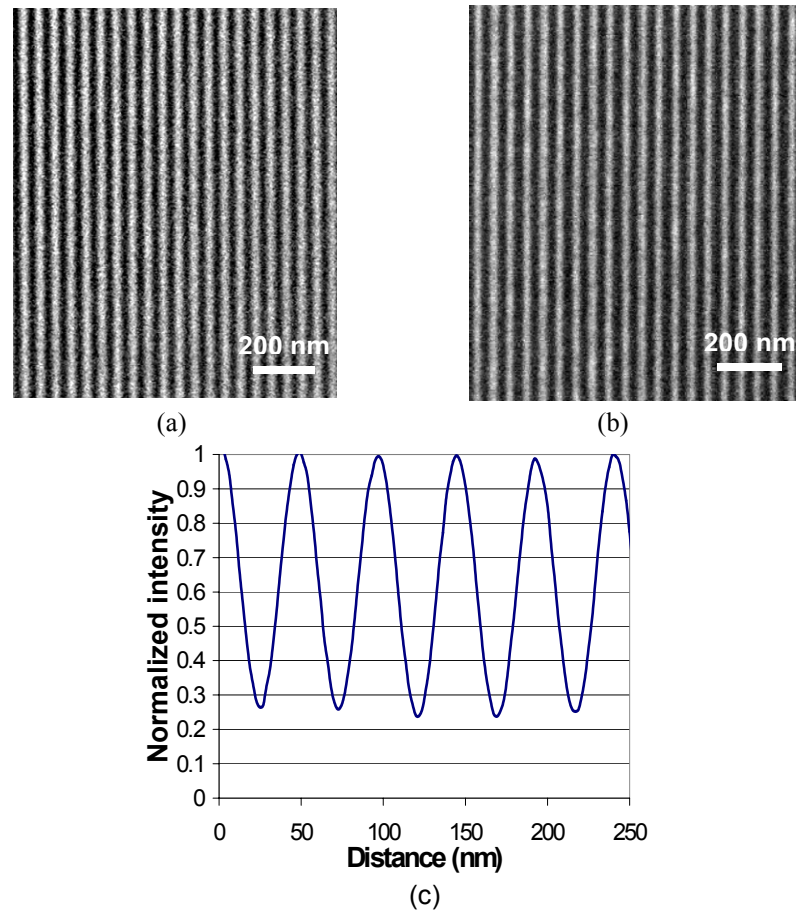


Figure 5-11. (a) A soft x-ray image of the 24.3 nm-half-period multilayer test pattern, taken at 600 eV ($\lambda = 2.07$ nm). A 25-nm micro zone plate fabricated with the bilayer process ($N = 300$, 30 μm diameter), and a 60-nm condenser zone plate ($N = 41700$, 10 mm diameter) were used. The σ value was 0.41. (b) An SEM micrograph of the pattern obtained with an in-lens detector (secondary electron detection). (c) A column averaged lineout of combined soft x-ray images.

Figure 5-12 (a) and (b) shows a soft x-ray image and an SEM micrograph of a test pattern with a measured half-period of 19.5 nm. Again the x-ray image and the micrograph have projected 4 nm pixels. The normalized measured modulation, seen in Fig. 5-12 (c), of the soft x-ray images of the pattern is 20%. Comparing the photon flux measured at the silicon substrates adjacent to the test patterns and the openings at the

samples' centers, the thickness of the 24.3 nm and 19.5 nm half-period patterns was determined to be 200 nm. This is close to the calculated optimal thickness for imaging contrast, 217 nm. A 15.1 nm half-period test pattern was also imaged with the microscope [Fig. 5-13 (a)], but was beyond the system cutoff, 17 nm half-period, for the 25 nm lens at σ equal to 0.41.

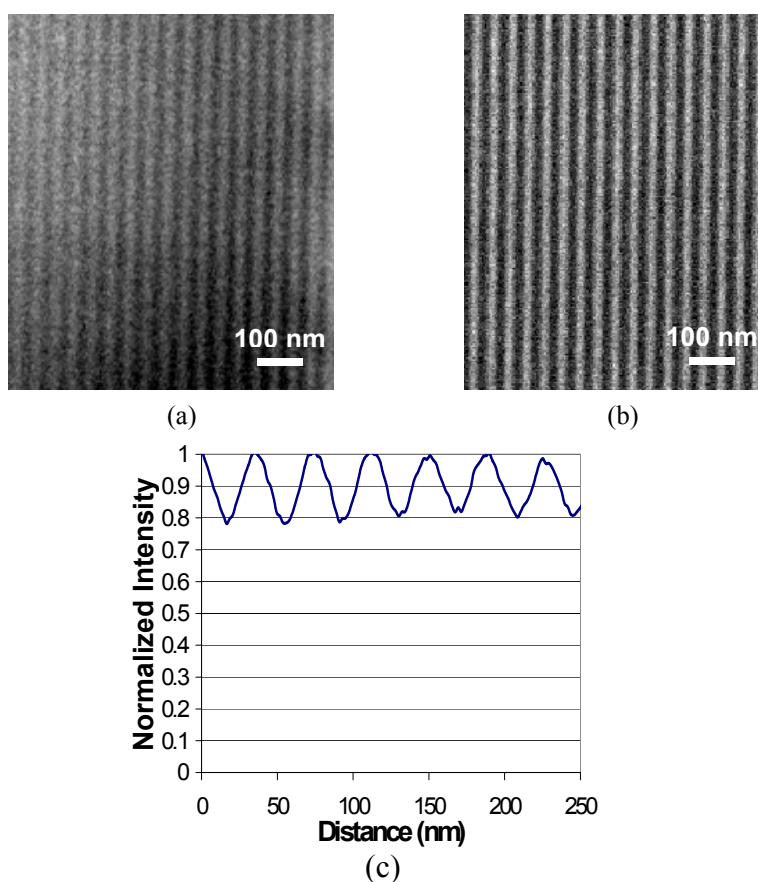


Figure 5-12. (a) A soft x-ray image of the 19.5 nm half-period multilayer test pattern taken at 600 eV ($\lambda = 2.07$ nm). (b) An SEM micrograph of the pattern. (c) A column averaged lineout of the soft x-ray images shows a modulation of 20%.

The three measured data points and a calculated image modulation curve for the microscope are shown in Figure 5-14. The calculation was performed using the SPLAT

computer program⁸⁹. Again, the objects in the calculation were periodic, equal lines and spaces. A rectangular transmission profile was assumed, neglecting interdiffusion between silicon and chromium layers. The calculation assumed monochromatic, hollow-cone radiation, uniformly illuminating the object. Calculated modulations for the 24.3 nm and 19.5 nm half-periods are 89% and 43%, respectively.

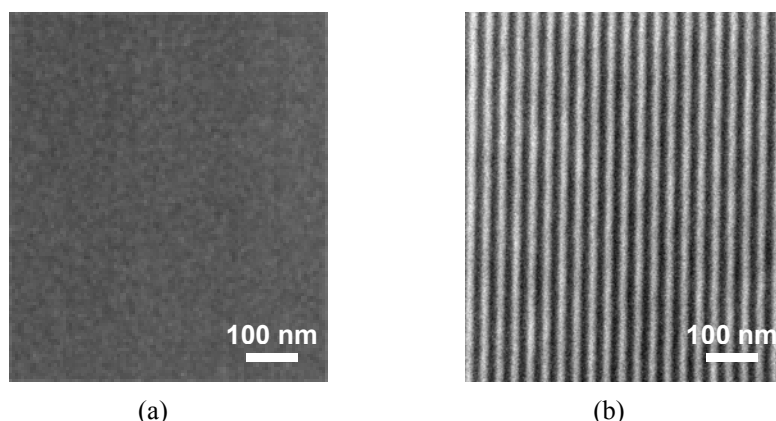


Figure 5-13. (a) A soft x-ray image of the 15.1 nm half-period multilayer test pattern taken at 600 eV ($\lambda = 2.07$ nm) shows no modulation. (b) An SEM micrograph of the pattern.

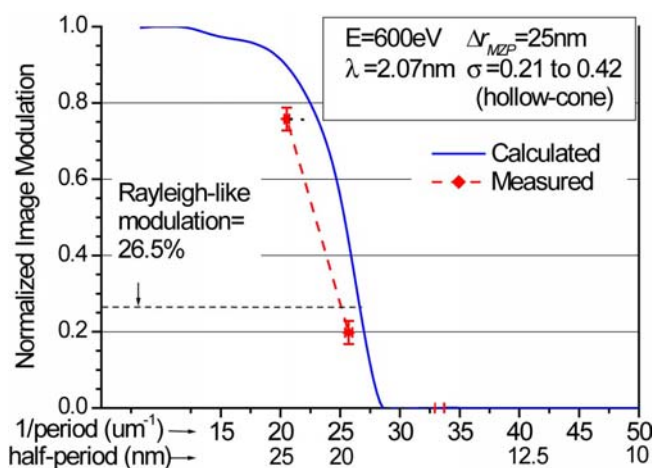


Figure 5-14. Simulated image modulations for XM-1 with a hollow-cone, partially coherent illumination, and measured modulations at half-periods of 24.3 nm, 19.5 nm, and 15.1 nm.

Using a straight-line approximation between the measured points at 19.5 nm and 24.3 nm half-periods, the Rayleigh-like modulation of 26.5% occurs at a half-period of 20 nm, while the calculated curve achieves this modulation at 19 nm. Based on these comparisons, we conclude that the spatial resolution of the microscope is 20 nm, and thus the system is 1.1x diffraction limited at this photon energy.

Possible sources of the discrepancy between the measurement resolution using multilayer test patterns and theory include the imperfection of the micro zone plate, such as aberrations and scattering due to zonal roughness, and finite spectral bandwidth. Further testing (e.g. at-wavelength interferometry) and simulations are anticipated in the future to characterize the effect of each of these factors.

5.6 Conclusion

Fig. 5-15 summarizes the measured modulations of various line test patterns (e-beam fabricated and multilayer-based) obtained with different zone plate configurations, as well as the calculated response of the microscope. The measured resolution is indicated in the figure for each case. Not shown in the figure is the measurement with the “knife-edge” test object, for a 35-nm micro zone plate and a σ value of 0.64, which resulted in a resolution of 31 nm. Significant advances in the microscope’s performance have been achieved, from 31 nm to 20 nm, over a four-year period. The best resolution was obtained with a 25-nm micro zone plate and a 60-nm condenser, a partial coherence factor of 0.41.

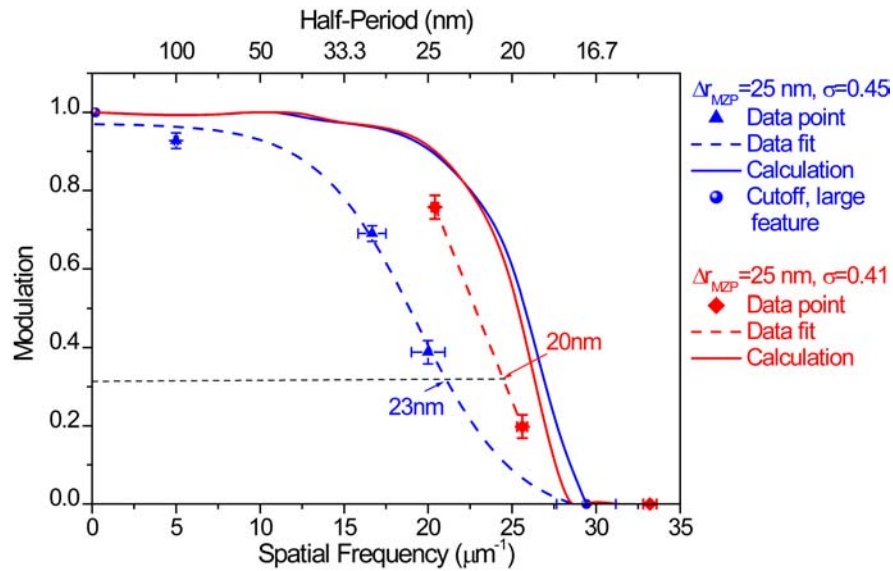


Fig. 5-15. Summary of the experimental measurements with lines and spaces in this chapter. The measured data points, and the data fit (dashed line), as well as the calculated modulation transfer function (solid line) for each experiment are plotted above. The resolution obtained is shown by the number. Not shown is the resolution result, 31 nm, obtained with a knife-edge test object for a 35-nm micro zone plate and a σ value of 0.64. As seen above, the resolution of the microscope has improved from 31 nm to 20 nm, made possible by the advancement of the micro zone plates.

To further improve the resolution, the outer zone widths of the micro zone plates need to be further reduced. The outermost zone width, 25 nm, achieved here was already close to the resist limit in the electron beam lithography and yielded the best resolution reported in the literature at that time. In the next chapter, a new zone plate overlay fabrication process is described, which yields narrower yet zone plates.

Chapter 6

Breakthrough in Resolution using New Overlay Nanofabrication Technique

6.1 Introduction

In the last chapter, a resolution of 20 nm was obtained at the soft x-ray microscope, using a micro zone plate with 25 nm outer zones and a σ value of 0.41. This resolution was nearly diffraction limited (1.1λ). For further resolution improvement, the outermost zone widths of the micro zone plates must be reduced ($\text{Res} = k_1 \Delta r_{\text{MZIP}}^*$). Various fabrication difficulties, however, have made fabrication of sub-25-nm zone plates challenging. Recently, a new fabrication technique has been developed in-house to overcome these difficulties. The technique enables fabrication of zone plates, which have dense zone patterns, by means of overlaying semi-dense patterns. With this technique, micro zone plates with outermost zone widths of 15 nm have been successfully fabricated. Preliminary results show that the microscope, using a 15 nm zone plate lens, has resolved the 15.1 nm Cr/Si multilayer test object, which showed no modulation in its previous image obtained with a 25 nm zone plate [Fig. 5-13]. These new results, which have been long sought by scientists, represent a breakthrough in the microscopy community. The overlay technique demonstrates a clear pathway to sub 10-nm spatial resolution.

* Since the previous optics have delivered near diffraction-limited performance, with a less than optimal σ value, 0.41, the resolution can also be improved by increasing the σ value to the optimal value, 0.7. This can be achieved by the use of a condenser zone plate with a 36 nm outermost zone width. According to Fig. 3-17, at σ equal to 0.7, k_1 is equal to 0.64, or for Δr_{MZIP} equal to 25 nm, the calculated resolution would be 16 nm. However, as compared to the calculated resolution of 19 nm with a σ value of 0.41, this resolution improvement is somewhat limited, e.g. 19 nm to 16 nm.

In order to obtain optimal imaging performance with the new high-resolution micro zone plates, smaller outermost zone widths are also needed for the condensers, to maintain the proper illumination ($\sigma = \Delta r_{MZP} / \Delta r_{CZP}$). For the 15 nm micro zone plates, a 40 nm outermost-zone-width condenser was fabricated, yielding a not too far optimal illumination at $\sigma = 0.37$. Fabrication of the condenser and micro zone plates, as well as the overlay technique, is discussed in this chapter.

6.2 Micro zone plate improvement: challenges for fabrication of high-resolution zone plates

As mentioned in chapter 5, dense line patterns with half-periods smaller than 25 nm are difficult to fabricate using the electron beam lithographic techniques previously used for zone plate fabrication. Several factors contribute to the difficulty, most notably beam broadening due to electron scattering and secondary electron generation in the resist layer, resultant low resist contrast, and mechanical stability due to the resultant narrow but tall zones, and thus higher aspect ratio.

Monte Carlo simulations^{102,103} have shown that energetic electrons incident upon the resist are scattered by the resist particles both elastically and inelastically. Inelastic scattering results in secondary electrons from a few-eV to a few-keV energy, which expose the resist much more readily than the incident high-energy electrons *and* have spatial distribution larger than the beam diameter. Thus, the zones that should not be exposed have unwanted electron exposure due to secondary electrons from adjacent zones (analogous to low, unwanted intensity induced by diffraction in the dark spaces of

a dense line and space pattern's image). This process, which is known as the proximity effect, is intrinsic to the electron-solid interaction. The degree of this effect depends on the resist material, resist thickness, and electron energy. Unlike backscattering, for which empirically determined mathematical expressions for long-distance electron scattering by the substrates has been successfully accounted¹⁰⁴, the intermediate (and short-distance (forward)) scattering requires more research to be fully understood. Currently, no effective compensation has been found to improve lithography's resolution limit due to scattering¹⁰⁵.

Ideally, the small dose variation, between the designed opaque and clear zone regions, can produce the wanted zone structures, if the resist development has an abrupt dose response; the regions which receive dose somewhat higher or lower than a threshold retain the resist, or have the resist removed completely, respectively, and the regions with dose near the threshold have resist partially removed. The abruptness of the dose response for high-resolution e-beam resists, or the contrast, however, is typically modest. This results in small-modulated structures in the resist layer with no clearance of resist in the "clear" zones.

Furthermore, for reasonable zone plate efficiency, the fabricated zone structures require a minimal thickness, about 100 nm for gold or nickel used at soft x-ray wavelengths. Reduction of the zone widths thus necessarily increases the aspect ratios of the zone structures. For outermost zone widths of 10 nm, a 100-nm-thick zone structure has an aspect ratio of 10:1 in the outer zone region. For commonly used polymers and

resists, such as AZPN114 in the bilayer process, an aspect ratio of 4:1 is difficult to achieve. At this aspect ratio, zones made of those materials collapse, possibly due to the surface tension of solutions in the wet processes, including development and electroplating. The aspect ratio limit is one of the major problems which hinder fabrication of high-resolution zone plate lenses with modest to high efficiency. Towards this problem, Weiss et. al. have demonstrated that a specially designed copolymer, MPEDVB, after irradiation at extremely high dose, allows fabrication to an impressive 8:1 aspect ratio zone structure¹⁰⁶. In their technique, the high dose required for complete cross linking of the copolymer is obtained from synchrotron radiation. Another approach, developed by Harteneck et. al.¹⁰⁷, uses bridges between zones to provide additional support to the tall structures. To avoid any adverse effect to the focusing of the zone plates, these “buttresses” are distributed randomly only in the outermost zone region, where the smallest zones have the highest aspect ratios. This method has permitted fabrication of 7:1 aspect ratio zone plates. However, both of these techniques have not yet yielded the needed aspect ratio of 10:1 or larger.

6.3 Solution for the fabrication challenges: overlay nanofabrication technique

As discussed in the last section, several fabrication problems limit the fabrication of dense zone plates, with small outer zones. However, these problems are less critical for semi-dense zone patterns, which have the desired narrow zones with wider separation[†]. A new technique, based on this observation, has been developed. In this technique, a zone plate is divided into two (or more) less dense, complementary patterns, which are

[†] This can be understood in terms of the proximity effect caused by electron scattering, as discussed in Sec. 6.2

fabricated individually and overlaid with high accuracy to yield the desired zone plate pattern. The concept is illustrated in Fig. 6-1.

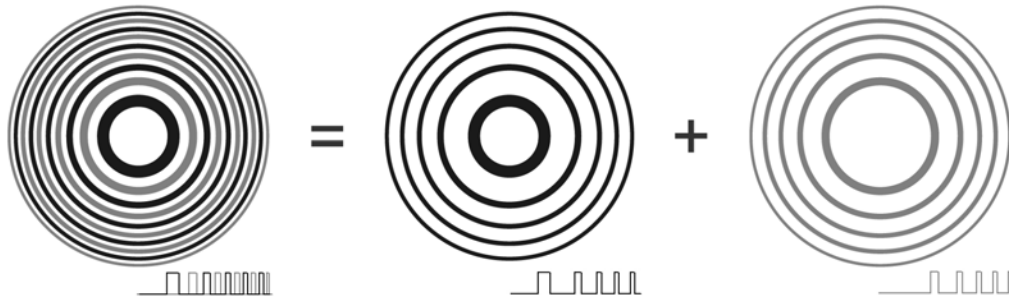


Figure 6-1. Illustration of the new overlay nanofabrication technique for high-resolution zone plates. The technique utilizes the fact that narrow isolated lines are much easier to be fabricated. In the technique, a zone plate is divided into two (or more) less dense, complementary patterns. One of the patterns (black) is first fabricated, and the complementary pattern (gray) is then fabricated on top of the first pattern, with high overlay accuracy, to yield the desired zone plate pattern.

This overlay technique not only reduces the proximity effect on pattern definition, but also relaxes the resist contrast requirement for highly dense line patterns. Furthermore, by stacking identical zone structures, a high-aspect-ratio zone plate can be realized with this technique. Multilevel zone plates¹⁰⁸, with sub-zonal structures, can also be fabricated using this technique. These zone plates, which could approximate the blazed zone plates, will in general yield higher efficiency than the conventional Fresnel zone plates.

One of the keys to the success of this technique is a high overlay accuracy in writing the semi-dense patterns. For planar zone plates (not multilevel), the required zone

placement accuracy for achieving perfect optical performance¹⁷ is typically about one third of the smallest zone width or smaller. Furthermore, to obtain high-quality zone plates, the two zone patterns need to have similar zonal quality. This requires a careful control of the fabrication processes and Nanowriter calibration for the two zone patterns. As described in the next section, a zonal placement accuracy of less than 2 nm has been obtained for zone plates of 15 nm outer zones, using an in-house developed alignment algorithms with pre-fabricated marks on the wafer, thus permitting further advances in the future. The two zone sets have similar quality, as revealed by scanning electron microscopy.

6.4 Fabrication of 15 nm micro zone plates using the overlay nanofabrication technique

Using the overlay technique, micro zone plates with 15 nm outermost zone widths were fabricated in the first attempt. The fabrication processes was composed of three sequential lithographic steps – alignment mark fabrication, first zone set fabrication, and second zone set fabrication, as illustrated in Fig. 6-2. Each step used the single layer process [section 2.4], and the standard micro zone plate wafer was used.

In the first step, four variants of the two-dimensional Barker alignment mark series¹⁰⁹ [Fig. 6-2], each of which was a rotated copy of the other, and a similar set of marks closer to the center, were fabricated outside the zone plate membrane windows on the substrate. Because the marks would be used for overlaying the subsequently fabricated zone patterns, as well as for the fine-calibration of the electron beam deflection, placement of the marks was critical. For this, the electron beam, and the major

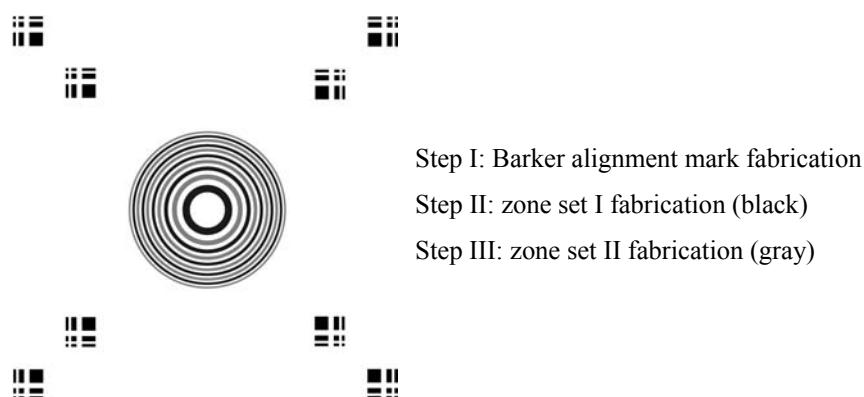


Figure 6-2. Illustration of the fabrication process for 15 nm micro zone plates. The complete process consists of three sequential lithographic steps: fabrication of Barker alignment marks, zone set I (black) fabrication, and zone set II (gray) fabrication. Fabrication of the two zone sets used the alignment marks for placement reference. The marks, $2\ \mu\text{m} \times 2\ \mu\text{m}$ in size, are fabricated outside the membrane window (not shown) on which the zone plate is placed. The final zone plate has a diameter of $30\ \mu\text{m}$.

and minor field deflection of the Nanowriter were carefully calibrated before the alignment mark exposure [section 2.5[‡]]. In addition, to minimize the placement errors, mark sets outside each membrane window were designed to be within the Nanowriter beam deflection field, so that stage movement was not needed during exposure of the marks. The final alignment marks were formed by electroplating in gold (50 nm thick) for good backscatter contrast at the Nanowriter.

After fabrication of the alignment marks, zone set I (black), with alternate zones missing, was exposed at the membrane window center. For best placement accuracy the electron beam position, and the beam deflector's scaling and orthogonality, were fine

[‡] Readers are encouraged to see section 2.5 for more details on the Nanowriter and its operation.

calibrated before each zone pattern exposure, using our special alignment algorithm¹¹⁰. In this algorithm, locations of the inner Barker marks were compared with the desired locations using cross correlation, and necessary beam deflection adjustments were calculated and fed back into the system to correct for the location deviations. This process was repeated twice, achieving a calibration accuracy of better than 2 nm. Exposure of the zone pattern then followed, which took 10 seconds. Following the single layer process, the wafer was processed and the standard gold plating [section 2.5] was used to form the desired zone structure.

After fabrication of the zone set I, zone set II was fabricated, using the same process used for zone set I. By use of the alignment procedure before exposure, zone set II was exposed at the proper position with respect to the alignment marks, and thus also to zone set I, with similar accuracy. The outer alignment marks were used for alignment and fine calibration. The inner mark patterns were filled with gold during electroplating of zone set I, and thus were not available for set II. Zone set II was then formed by gold plating, in the same manner as for the zone set I.

Details of the zone plate fabrication process are outlined in Fig. 6-3. The columns show, respectively, the fabrication steps for alignment marks, zone set I, and zone set II. In each lithographic step, the positive-tone e-beam resist, polymethyl methacrylate (PMMA), which has demonstrated fabrication limit of 5-nm wide isolated line¹¹¹, was

used for recording the pattern. The final zone plate, composed of the two zone sets, was fabricated in gold[§], as described earlier, with a thickness of 80 nm (aspect ratio of 5:1).

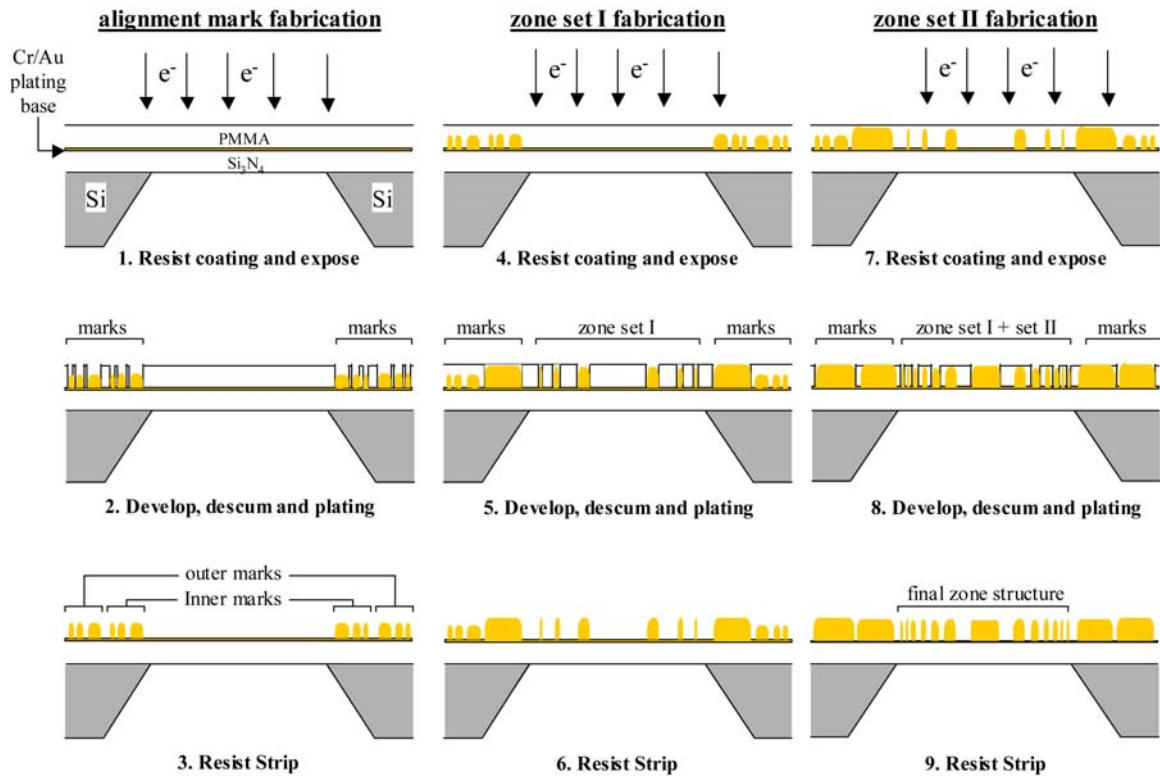


Figure 6-3. Illustration of the overlay nanofabrication process used for the 15-nm micro zone plates. The process has three sequential lithographic steps: alignment mark fabrication (left column), first zone set fabrication (middle column), and second zone set fabrication (right column). The positive-tone e-beam resist, PMMA, was used in all three steps. The process is described in detail in Appendix A.

For those readers who are interested in further fabrication details, a full description of the process can be found in appendix B.

[§], Gold was chosen over nickel for its higher efficiency at this thickness in the microscope's broad operating photon range (0.3 keV to 1.8 keV).

6.5 The first ever 15 nm zone plates

Fig. 6-4 shows an SEM micrograph of one of the micro zone plates fabricated with 15 nm outer zones. The zone plate has 500 zones, and a diameter of 30 μm . The gold zones are bright in the micrograph. The magnified inset reveals a nearly perfect alignment of the opaque zones. Centroid measurement of the gold zones indicates a sub-pixel zone placement accuracy (1σ) of 1.7 nm, typical of the less than 2 nm placement accuracy achieved with the Nanowriter. As discussed before, for diffraction-limited performance, zone placement of less than one third of the smallest zone widths is needed, which is well satisfied in this case. The zone placement accuracy is uniform across the zone plate, as supported by a Moire pattern obtained from the interference of the zones and a scan of the electron microscope. As shown in Fig. 6-4, the zone widths are larger than desired, and have imperfections. This is expected to improve in the near future by better electron dose control. We have observed that zone set II has slightly larger gold grains than zone set I, possibly due to prolonged exposure of the plating bath to air. These

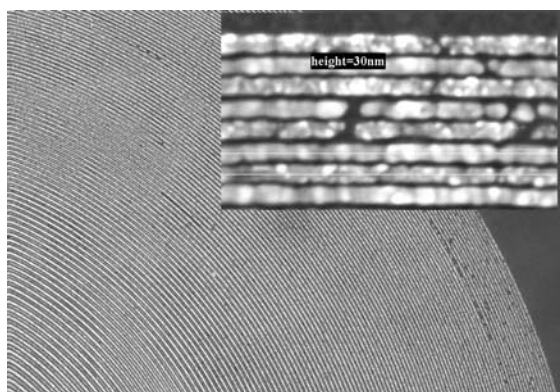


Figure 6-4. Scanning electron micrograph of a zone plate with 15 nm outermost zones. Shown in the inset is a more detailed view of the outermost zones. The zone placement accuracy is measured to be 1.7 nm.

15 nm micro zone plates are a significant improvement over the previous 25 nm zone plate lenses. To fully utilize the new optics, improvement of the condenser zone plates also needs to be made, which is discussed in the next section.

6.6 Condenser zone plate with 40 nm zone widths

In order to maintain nearly optimal illumination for spatial resolution enhancement, and avoidance of speckle effects or ringing at sharp features' edges, a degree of partial coherent factor σ ($= \Delta r_{MYP} / \Delta r_{CZP}$), with values between 0.4 and 0.7, is desired. For an MYP of outermost zone width of 15 nm, this σ range corresponds to Δr_{CZP} values ranging from 38 nm to 22 nm. Fabrication of such small zone widths is, however, a significant challenge for a large condenser zone plate (see below). For our first attempt, a 9-mm-diameter condenser zone plate with 40 nm outer zones was chosen for use with the 15 nm MYP, and was successfully fabricated. The achieved σ value is 0.37.

The main difficulty in fabricating a large (9-10 mm diameter) condenser zone plate with small outer zone widths is, as discussed in section 2.4, the lack of a proper e-beam resist, which must have both high resolution for the small feature sizes, and high sensitivity for reasonable exposure time. For the 40 nm condenser zone plate, a positive-tone e-beam resist, ZEP 520 (Zeon Corporation, Tokyo) was used. The resist provides a compromise to the desired properties; it has a resolution of about 30 nm, and a sensitivity about twice that of the KRS resist, used for the 60 nm condenser zone plate [section 5.5 and appendix A]. For the 9-mm-diameter condenser, the exposure time was about 4

days^{**}. To minimize drift of Nanowriter's writing condition during the course of exposure, the system was automatically re-calibrated every few hours using a Barker mark, prefabricated at a corner of the membrane window (refer to appendix B for further details).

To achieve high efficiency, the ZEP resist had a thickness of 150 nm, and thus an aspect ratio close to 4:1. To avoid resist collapse, which had been a problem at this aspect ratio before, buttresses [section 6.2] were used to support the zone structure. For minimal effects to the condenser's focus profile (point spread function) and efficiency, they were distributed in a random fashion in the outer zone region, where the narrow zones have the highest aspect ratios. The final zone plate structure was plated with nickel to a thickness of about 120 nm.

6.7 Testing with multilayer test objects

With successful fabrication of the new micro zone plate and condenser, the microscope was characterized for resolution, using the multilayer test objects [section 4.3.2] at small feature sizes. The 15.1 nm and 19.5 nm half-period Cr/Si multilayer test objects, used earlier for the 25 nm MZP with $\sigma = 0.41$ [section 5.5], were used in these new experiments.

Fig. 6-5 shows a comparison of x-ray images of test patterns seen previously with a 25 nm zone plate [section 5.5] and now with the new 15 nm zone plate. The two images

^{**} The increase in exposure time was not only due to the reduction of resist sensitivity, but also the use of buttresses, which requires complex on-the-fly computation in the zone plate exposure by the Nanowriter.

on the left, Fig. 6-5 (a) and (c), were obtained with the 25 nm zone plate, at 2.07 nm wavelength (600 eV), just above the Cr absorption edge at 574 eV. The image of the pattern with 19.5 nm lines and spaces [Fig. 6-5 (a)] shows good modulation, while the

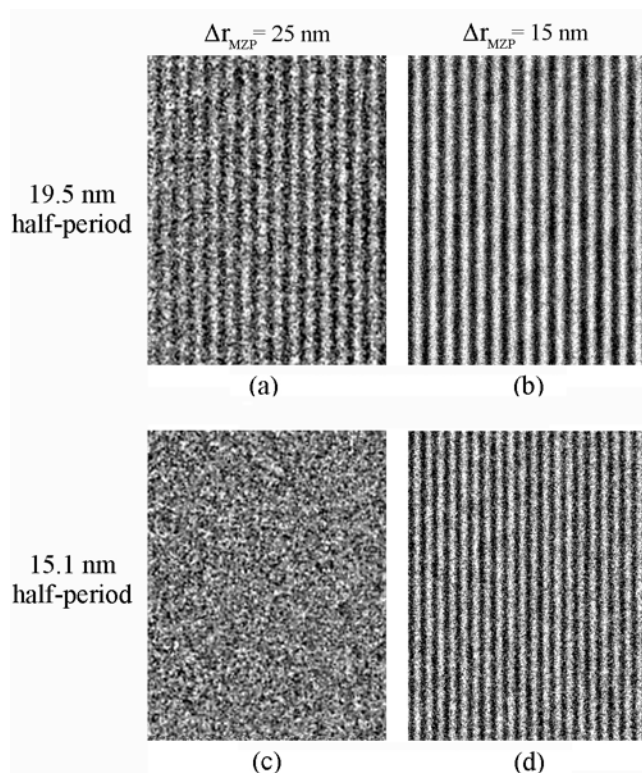


Figure 6-5. Soft x-ray images of 19.5 nm and 15.1 nm half-period test objects, as formed with zone plates having outer zone widths of 25 nm ((a) and (c)) and 15 nm ((b) and (d)). Significant improvements are noted between the images obtained with the new 15 nm zone plate (right column), as compared to earlier results obtained with the 25 nm zone plate (left column). This is particularly evident for the 15 nm half-period images (bottom row), for which the earlier result shows no modulation, whereas the image obtained with the 15 nm zone plate shows excellent modulation. Images (a) and (c) were obtained at a wavelength of 2.07 nm (600 eV photon energy); (b) and (d) were obtained at a wavelength of 1.52 nm (815 eV). The equivalent object plane pixel size for images (a) and (c) is 4.3 nm; the size for (b) and (d) is 1.6 nm.

image of 15.1 nm lines and spaces [Fig. 6-5 (c)] shows no modulation with this lens. As seen below in Fig. 6-6, this data point is beyond cutoff for the 25 nm lens. Returning to Fig. 6-5, the two images on the right side, (b) and (d), were obtained with the new 15 nm zone plate lens, at a wavelength of 1.52 nm (815 eV). The shorter wavelength allowed us to maintain a convenient working distance. Images obtained with the 15 nm outer zone width lens show clear improvements when compared to those with the 25 nm zone plate. The 19.5 nm image in Fig. 6-5(b) displays less noise and better contrast than that in Fig. 6-5(a), which has a modulation of 20% [section 5-5]. The improvement is particularly evident in images of the 15.1 nm lines for which the earlier results with the 25 nm lens showed no modulation [Fig. 6-5(c)], as predicted by calculation, whereas the image obtained with the 15 nm lens [Fig. 6-5(d)] shows excellent modulation.

Modeling of the modulation transfer function (MTF) for the 15 nm lens, as well as for the 25 nm zone plate, is shown by solid lines in Fig. 6-6. Similar to the previous MTF calculations, the computational modeling, obtained by using the SPLAT program, accounts for the partially coherent, hollow cone, soft x-ray illumination employed specifically in each case. With the higher numerical aperture ($NA = \lambda / 2\Delta r$), the MTF curve for the 15 nm zone plate shifts to higher spatial frequencies. The theoretically achievable resolution is 12 nm for the 15 nm zone plate, 19 nm for the 25 nm zone plate. These predictions are consistent with the images in Fig. 6-5, and with the three data points shown in Fig. 6-6 for the 25 nm lens. Data points for the 15 nm lens (images Fig. 6-5(b) and (d)) are not shown in Fig. 6-6 due to the presence of somewhat non-uniform stray light which prevents assignment of an unambiguous modulation. The stray light, unusual

for our zone plate lenses, is largely due to the absence of an absorbing metal coating outside the zone plate pattern, allowing undiffracted radiation to reach the CCD directly. This will be corrected in future experiments. We believe that the improved imaging capability, as illustrated in Fig. 4, and supported by Fig. 5, is the clear demonstration of the breakthrough – resolution improvement to sub 15 nm regime, long sought by x-ray scientists – with the new 15 nm zone plate.

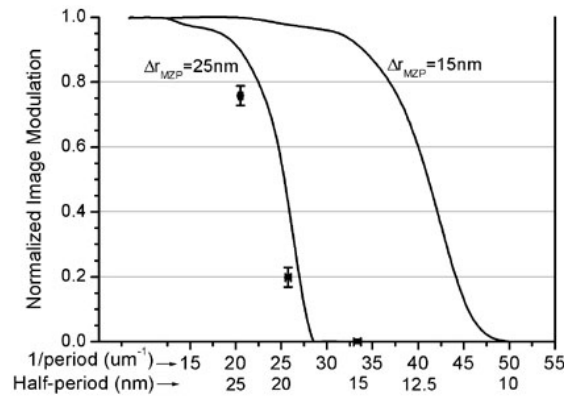


Figure 6-6. The calculated modulation transfer functions of the microscope with two zone plates, one having an outer zone width, Δr_{MZP} , of 25 nm (left line) and one of $\Delta r_{MZP} = 15$ nm (right line). The theoretical resolutions for the two lenses are 19 nm and 12 nm, respectively. Also shown are data indicating the degree of modulation obtained for various test patterns using the $\Delta r_{MZP} = 25$ nm (squares). The $\Delta r_{MZP} = 25$ nm zone plate yielded 75% modulation for a half-period of 24.3 nm, 20% for 19.5 nm, and 0% modulation for a half-period of 15.1 nm [Fig. 6-5(a) and (c)]. Using the $\Delta r_{MZP} = 15$ nm zone plate, image quality is dramatically improved, as seen in Fig. 6-5 (b) and (d), however, due to a high degree of stray light an accurate determination of the modulation was not possible.

6.8 Conclusions

In this chapter, a significant resolution advancement, is described, based on a new zone plate fabrication technique. Using the overlay technique, zone plates with outermost zone widths of 15 nm were successfully fabricated. Such a zone plate, combined with a compatible 40 nm condenser, has enabled the microscope XM-1 to clearly image 15.1 nm half-period test pattern. Sub 15 nm resolution has resulted, as demonstrated by the improved image quality.

The zone plates presented here are our first attempt at using the new overlay nanofabrication technique. With current capabilities for pattern writing, overlay accuracy, and process control, we anticipate fabrication of zone plates with 10 nm outer zones in near future. High aspect-ratio zone plates, fabricated by stacking zone structures, are also expected using this powerful technique. We believe that the advancement presented here will extend the use of x-ray microscopy in the burgeoning fields of nanoscience and nanotechnology.

Chapter 7

Conclusions

Soft x-ray microscopy is a valuable analytic tool for nanoscience and nanotechnology. It offers a *unique* set of *proven* capabilities that complement those of electron and scanning probe microscopy, including high spatial resolution (~ 10 nm), elemental and chemical specificity, spin-orbit sensitivity, large permissible sample thickness, and in-situ studies in many useful sample environments and conditions such as applied magnetic and electric fields and coverage by overcoatings. In particular, with high spatial resolution, the full-field transmission microscope, XM-1, has yielded valuable knowledge in many areas of the physical and life sciences. This thesis describes in details the spatial resolution improvement and characterization of the microscope. Using various measurement techniques, including the novel multilayer test objects which were shown to permit more accurate quantification than the other techniques, the microscope's resolution was carefully characterized, and was shown to be near-diffraction-limited at 20 nm. Such a high quality performance was made possible by the fabrication of micro zone plates using the Nanowriter electron beam lithography tool, which is capable of achieving small outer zone widths and nanometer-scale zone placement accuracy. To obtain better resolution, a powerful overlay nanofabrication technique based on sequential fabrication of alternating zone structures has been developed. Using this technique with the Nanowriter, micro zone plates of 15 nm outer zones have been successfully fabricated. The zone placement accuracy was measured to be 1.7 nm, well within the required accuracy for the 15 nm zone plates. Using the

multilayer test objects, the zone plates have been quantified to achieve sub-15 nm resolution, the highest ever demonstrated with imaging optics. The result obtained is a breakthrough in soft x-ray microscopy, enabling the versatile capabilities of the microscopy to be applied to smaller features. We anticipate that, with the overlay technique, yet higher spatial resolution can be realized by fabrication of zone plates with outer zones of 10 nm or smaller. Zone plate efficiency is also expected to improve through the use of the new overlay technique, with the fabrication of high aspect ratio zone plates, in which zone patterns are written one on top of the other. The experimental results described in chapter 6 show that conventional zone plates provide a direct, reliable, and successful path to nanometer scaled imaging.

With the existence of more than thirty synchrotron facilities worldwide, these advances in soft x-ray microscopy could be readily available to the research community. Furthermore, we anticipate that compact soft x-ray sources will also be available in the not too distant future, using laser-produced plasmas, femtosecond laser high harmonic techniques, or EUV/soft x-ray lasers. With these advances we anticipate a wider use of zone plate based soft x-ray microscopy across the broad range of nanoscience and nanotechnology.

References

1. P. Fischer, G. Denbeaux, T. Ono, T. Okuno, T. Eimuller, D. Goll, and G. Schutz,
"Study of magnetic domains by magnetic soft x-ray transmission microscopy," J. Phys.
D **35**, 2391-2397 (2002).
2. D. T. Attwood, *Soft X-Rays and Extreme Ultraviolet Radiation: Principles and
Applications* (Cambridge University Press, Cambridge, U.K, 2000).
3. G. Schmahl and D. Rudolph Eds. *X-Ray Microscopy* (Springer-Verlag, Berlin, 1984).
4. S. Sayre, M. Howells, J. Kirz and H. Rarback Eds. *X-Ray Microscopy II* (Springer-
Verlag, Berlin, 1988).
5. A. G. Michette, G. Morrison and C. J. Buckley Eds. *X-Ray Microscopy III* (Springer-
Verlag, Berlin, 1992).
6. V. V. Aristov and A. I. Erko Eds. *X-Ray Microscopy IV* (Bogorodskii Press,
Chernogolovka, Russia, 1994).
7. J. Thieme, G. Schmahl, D. Rudolph and E. Umbach Eds. *X-Ray Microscopy and
Spectromicroscopy* (Springer-Verlag, Berlin, 1998).
8. W. Meyer-Ilse, T. Warwick and D. T. Attwood Eds. *X-Ray Microscopy VI* (American
Institute of Physics, Melville, N.Y., 2000).
9. J. Susini, D. Joyeux and P. F. Eds. *X-Ray Microscopy VII* (EDP Sciences, Paris, 2003).
10. Ref. 2, pp. 69-71.
11. J.H. Underwood, "X-Ray Optics," Amer. Sci. **66**, 476-486 (1978). For more in-depth
overview of the optics, see J. H. Underwood, "Imaging Properties and Aberrations of
Spherical Optics and Nonspherical Optics," in *Experimental Methods in the Physical*

- Sciences: Vacuum Ultraviolet Spectroscopy II*, J. A. Samson and D. L. Ederer Eds. (Academic Press, San Diego, 1998), chapter 9.
12. P. Kirkpatrick and A. V. Baez, "Formation of Optical Images by X-Rays," *J. Opt. Soc. Am.* **38**, 766-774 (1948).
 13. P. J. Eng, M. Newville, M. L. Rivers and S. R. Sutton, "Dynamically Figured Kirkpatrick Baez X-Ray Microfocusing Optics," in *X-Ray Microfocusing: Applications and Techniques*, I. McNulty Ed., *Proc. SPIE* **3449**, pp. 145-156.
 14. Lord Rayleigh, "Wave Theory," p. 429 in *Encyclopædia Britannica*, 9th Ed., Vol. 24, (1888); Rayleigh's first entry in his notebook, describing the first successful demonstration, is dated 11 April 1871. According to Woods, the work is never published (Ref. 15, p.37).
 15. J. L. Soret, "Concerning Diffraction by Circular Gratings," *Ann. Phys. Chem.* **156**, 99 (1875).
 16. R. W. Woods, *Physical Optics*, (Macmillan, New York, 1911; Opt. Soc. Amer., Washington, DC, 1988).
 17. A. G. Michette, *Optical systems for soft X rays*. (Plenum Press, New York, 1986)
 18. Takano, S. H and T. Y, A, "Sub-100 nm Hard X-Ray Microbeam Generation with Fresnel Zone Plate Optics," *Jpn. J. Appl. Phys.* **42**, L132-134 (2003).
 19. E. Spiller, *Soft X-Ray Optics* (SPIE, Bellingham, WA, 1994).
 20. T. W. Barbee and D. L. Keith, "Synthesis of Metastable Materials by Sputter Deposition Techniques," in *Synthesis and Properties of Metastable Phases*, M. E. S. and T. J. Rowland Eds. (Metallurgical Society, Amer. Inst. Mech. Eng., Warrendale, PA, 1980), p. 93.

21. J. H. Underwood and T. W. Barbee, "Soft-X-Ray Imaging with a Normal Incidence Mirror," *Nature* **294**, 429-431 (1981).
22. S. Bajt, J. B. Alameda, T. W. Barbee, W. M. Clift, J. A. Folta, B. Kaufmann and E. A. Spiller, "Improved Reflectance and Stability of Mo-Si Multilayers," *Opt. Eng.* **41**, 1797-1804 (2002).
23. P.P. Naulleau (Center for X-ray Optics/LBNL), personal communication.
24. P. P. Naulleau, K. A. Goldberg, E. Anderson, J. P. Cain, P. Denham, K. Jackson, A. S. Morlens, S. Rekawa and F. Salmassi, "Extreme Ultraviolet Microexposures at the Advanced Light Source Using the 0.3 Numerical Aperture Micro-Exposure Tool Optic," *J. Vac. Sci. Technol. B* **22**, 2962-2965 (2004).
25. E. Förster, "Crystal Optics," in *Experimental Methods in the Physical Sciences: Vacuum Ultraviolet Spectroscopy I*, J. A. Samson and D. L. Ederer Eds. (Academic Press, San Diego, 1998), chapter 19.
26. A. Snigirev, V. Kohn, I. Snigireva and B. Lengeler, "A Compound Refractive Lens for Focusing High-Energy X-Rays," *Nature* **384**, 49-51 (1996); For a detailed discussion on the design and principles of compound refractive lenses see A. Snigirev, V. Kohn, I. Snigireva, A. Souvorov and B. Lengeler, "Focusing High-Energy X Rays by Compound Refractive Lenses," *Appl. Opt.* **37**, 653-662 (1998), and B. Lengeler, C. Schroer, J. Tummler, B. Benner, M. Richwin, A. Snigirev, I. Snigireva and M. Drakopoulos, "Imaging by Parabolic Refractive Lenses in the Hard X-Ray Range," *J. Synchrot. Radiat.* **6**, 1153-1167 (1999).
27. Ref. 24, last reference.

28. K. Schwarzschild, "Untersuchungen Zur Geometrischen Optik II: Theorie Der Spiegelteleskope," *Astronomische Mittheilungen der Königlichen Sternwarte zu Göttingen* **10**, 3-28 (1905). Reprinted in SPIE Mileston Series, Vol. MS 73, 1993.
29. Ref. 2, section 4.5.1 to 4.5.3.
30. Ref. 19, p. 50-54. It provides an informative discussion of the design of Schwarzschild objectives.
31. G. Schmahl and D. Rudolph, "High Power Zone Plates as Image Forming Systems for Soft X-Rays," *Optik* **29**, 579-587 (1969); B. Niemann, D. Rudolph and G. Schmahl, "Soft-X-Ray Imaging Zone Plates with Large Zone Numbers for Microscopic and Spectroscopic Applications," *Opt. Commun.* **12**, 160-163 (1974).
32. B. Niemann, D. Rudolph and G. Schmahl, "X-Ray Microscopy with Synchrotron Radiation," *Appl. Optics.* **15**, 1883-1884 (1976).
33. G. Schmahl, D. Rudolph, B. Niemann and O. Christ, "Zone-Plate X-Ray Microscopy," *Q. Rev. Biophys.* **13**, 297-315 (1980).
34. D. Rudolph, B. Niemann, G. Schmahl and O. Christ, "The Göttingen X-Ray Microscope and X-Ray Microscopy Experiments at the Bessy Storage Ring," in Ref. 1, p. 192-202.
35. G. Schmahl, D. Rudolph, B. Niemann, P. Guttman, M. Robert-Nicoud, J. Thieme, G. Schneider, C. David, M. Diehl and T. Wilhein, "Natural Imaging of Biological Specimens with X-Ray Microscopes," in *Synchrotron Radiation in the Biosciences*, B. Chance, D. Deisenhofer, S. Ebashi, et al. Eds. (Oxford University Press, 1994), pp. 538-562.

36. G. Schneider and B. Niemann, "Cryo X-Ray Microscopy Experiments with the X-Ray Microscope at BESSY," in Ref. 7, p. I-25.
37. K.-J. Kim, "Characteristics of synchrotron radiation," in *Physics of Particle Accelerators*, M. Month and M. Dienes, eds., AIP **184** (Amer. Inst. Phys., Melville, New York, 1989), pp. 565-632
38. G. Schmahl, D. Rudolph, G. Schneider, P. Guttman and B. Niemann, "Phase-Contrast X-Ray Microscopy Studies," *Optik* **97**, 181-182 (1994); G. Schmahl, D. Rudolph, P. Guttman, G. Schneider, J. Thieme and B. Niemann, "Phase-Contrast Studies of Biological Specimens with the X-Ray Microscope at BESSY," *Rev. Sci. Instrum.* **66**, 1282-1286 (1995);
39. G. Schneider, "Cryo X-Ray Microscopy with High Spatial Resolution in Amplitude and Phase Contrast," *Ultramicroscopy* **75**, 85-104 (1998).
40. C. Jacobsen, S. Williams, E. Anderson, M. T. Browne, C. J. Buckley, D. Kern, J. Kirz, M. Rivers and X. Zhang, "Diffraction-Limited Imaging in a Scanning-Transmission X-Ray Microscope," *Opt. Commun.* **86**, 351-364 (1991).
41. C. Jacobsen, J. Kirz and S. Williams, "Resolution in Soft-X-Ray Microscopes," *Ultramicroscopy* **47**, 55-79 (1992).
42. H. Rarback, D. Shu, S. C. Feng, H. Ade, J. Kirz, I. McNulty, D. P. Kern, T. H. P. Chang, Y. Vladimirsky, N. Iskander, D. Attwood, K. McQuaid and S. Rothman, "Scanning-X-Ray Microscope with 75-nm Resolution," *Rev. Sci. Instrum.* **59**, 52-59 (1988).
43. J. Kirz, C. Jacobsen, S. Lindaas, S. Williams, X. Zhang, E. Anderson and M. Howells, "Soft X-Ray Microscopy at the National Synchrotron Light Source," in

- Synchrotron Radiation in the Biosciences*, B. Chance, D. Deisenhofer, S. Ebashi, et al. Eds. (Oxford University Press, 1994), pp. 563-571
44. J. Kirz, C. Jacobsen and M. Howells, "Soft-X-Ray Microscopes and Their Biological Applications," *Q. Rev. Biophys.* **28**, 33-130 (1995).
 45. T. Tyliczszak (LBNL), personal communication.
 46. G. R. Morrison and M. T. Browne, "Dark-Field Imaging with the Scanning-Transmission X-Ray Microscope," *Rev. Sci. Instrum.* **63**, 611-614 (1992).
 47. G. Morrison, "Phase Contrast and Darkfield Imaging in X-Ray Microscopy," in *Soft X-Ray Microscopy*, C. J. Jacobsen and J. E. Trebes Eds., *Proc. SPIE* **1741**, pp. 186-193.
 48. C. Jacobsen, S. Lindaas, S. Williams and X. Zhang, "Scanning Luminescence X-Ray Microscopy - Imaging Fluorescence Dyes at Suboptical Resolution," *J. Microsc.* **172**, 121-129 (1993).
 49. H. Ade, "Development of a Scanning Photoemission Microscope," Ph.D. thesis, Physics Department, Stony Brook University (1990).
 50. H. Ade, J. Kirz, S. L. Hulbert, E. D. Johnson, E. Anderson and D. Kern, "X-Ray Spectromicroscopy with a Zone Plate Generated Microprobe," *Appl. Phys. Lett.* **56**, 1841-1844 (1990).
 51. W. Meyer-Ilse, H. Meddecki, L. Jochum, E. Anderson, D. Attwood, C. Magowan, R. Balhorn, M. Moronne, D. Rudolph and G. Schmahl, "New High-Resolution Zone-Plate Microscope at Beamline 6.1 of the Als," *Synchr. Radiat. News*, **8**, (1995), pp. 29-33.

52. W. Meyer-Ilse, G. Denbeaux, L. E. Johnson, W. Bates, A. Lucero and E. H. Anderson, "The High Resolution X-Ray Microscope XM-1," in Ref. 8, pp. 129-134.
53. P. Fischer, G. Denbeaux, T. Ono, T. Okuno, T. Eimuller, D. Goll, and G. Schutz, "Study of Magnetic Domains by Magnetic Soft X-Ray Transmission Microscopy," J. Phys. D **35**, 2391-2397 (2002).
54. W. Meyer-Ilse, D. Hamamoto, A. Nair, S. A. Lelievre, G. Denbeaux, L. Johnson, A. L. Pearson, D. Yager, M. A. Legros, and C. A. Larabell, "High Resolution Protein Localization using Soft X-Ray Microscopy," J. Microsc. **201**, 395-403 (2001).
55. S. C. B. Myneni, J. T. Brown, G. A. Martinez, and W. Meyer-Ilse, "Imaging of Humic Substance Macromolecular Structures in Water and Soils," Science **286**, 1335-1337 (1999).
56. M. C. G. Juenger, V. H. R. Lamour, P. J. M. Monteiro, E. M. Gartner, and G. P. Denbeaux, "Direct Observation of Cement Hydration by Soft X-Ray Transmission Microscopy," J. Mater. Sci. Lett. **22**, 1335-1337 (2003).
57. G. Schneider, E. Anderson, S. Vogt, C. Knochel, D. Weiss, M. Legros and C. Larabell, "Computed Tomography of Cryogenic Cells," Surf. Rev. Lett. **9** 177-183 (2002).
58. C. A. Larabell and M. A. Le Gros, "X-Ray Tomography Generates 3-D Reconstructions of the Yeast, *Saccharomyces Cerevisiae*, at 60-nm Resolution," Mol. Bio. Cell **15** 957-962 (2004).
59. G. Denbeaux, E. Anderson, B. Bates, W. Chao, J. A. Liddle, B. Harteneck, A. Pearson, F. Salmassi, G. Schneider, P. Fischer, T. Eimuller, S. Taylor, H. Chang, and

- G. J. Kusinski, "X-ray Magnetic Microscopy for Correlations between Magnetic Domains and Crystal Structure," *J. de Physique IV* **104**, 477-481 (2003).
60. H. Stoll, A. Puzic, B. van Waeyenberge, P. Fischer, J. Raabe, M. Buess, T. Haug, R. Hollinger, C. Back, D. Weiss, and G. Denbeaux, "High-resolution imaging of fast magnetization dynamics in magnetic nanostructures," *Appl. Phys. Lett.* **84**, 3328-3330 (2004).
61. G. Schneider, M. A. Meyer, G. Denbeaux, E. Anderson, B. Bates, A. Pearson, C. Knochel, D. Hambach, E. A. Stach, and E. Zschech, "Electromigration in Passivated Cu Interconnects Studied by Transmission X-Ray Microscopy," *J. Vac. Sci. Techn. B* **20**, 3089-3094 (2002).
62. G. Denbeaux, E. Anderson, W. Chao, T. Eimuller, L. Johnson, M. Kohler, C. Larabell, M. Legros, P. Fischer, A. Pearson, G. Schultz, D. Yager, and D. Attwood, "Soft X-ray Microscopy to 25 nm with Applications to Biology and Magnetic Materials," *Nucl. Instrum. Meth. A* **467-468**, 841-844 (2001).
63. Ref. 2, pp. 123-135.
64. C. Larabell, D. Yager, and W. Meyer-Ilse, "Localization of Proteins and Nucleic Acids using Soft X-ray Microscopy," in Ref. 8, pp. 107-112.
65. V. H. R. Lamour, P. J. M. Monteiro, K. L. Scrivener, and H. Fryda, "Microscopic Studies of Early Hydration of Calcium Aluminate Cements," in *Proc. Int. Conf. Calcium Aluminate Cements*, R.J. Mangabhai and F.P. Glasser Eds., (2001), pp. 169-180.
66. G. Schneider, G. Denbeaux, E. H. Anderson, B. Bates, A. Pearson, M. A. Meyer, E. Zschech, D. Hambach, and E. A. Stach, "Dynamical X-Ray Microscopy Investigation

- of Electromigration in Passivated Inlaid Cu Interconnect Structures," Appl. Phys. Lett. **81**, 2535-2537 (2002).
67. N. Smith, "Science with soft x rays," Phys. Today **54** (1), pp. 29-34 (2001).; www.als.lbl.gov.
68. G. Schneider, G. Denbeaux, E. Anderson, W. Bates, F. Salmassi, P. Nachimuthu, A. Pearson, D. Richardson, D. Hambach, N. Hoffmann, W. Hasse, and K. Hoffmann, "Electromigration in Integrated Circuit Interconnects Studied by X-Ray Microscopy," Nucl. Instrum. Methods B **199**, 469-474 (2003).
69. G. Denbeaux, L. Johnson and W. Meyer-Ilse, "Spectromicroscopy at the XM-1," in Ref. 8, pp. 478-483.
70. Ref. 2, p. 342-349 and p. 361-363.
71. Ref. 17, p. 167-170.
72. E. Hecht, *Optics*, 3rd edition (Addison-Wesley, Reading, Mass., 1998), pp.476.
73. J. Goodman, *Introduction to Fourier Optics*, (McGraw-Hill, New York, 1996) 2nd edition, section 4.4.3.
74. J. Kirz, "Phase Zone Plates For X-Rays And Extreme UV," J. Opt. Soc. Amer. **64**, 301-309 (1974).
75. E. H. Anderson, D. L. Olynick, B. Harteneck, E. Veklerov, G. Denbeaux, W. L. Chao, A. Lucero, L. Johnson, and D. Attwood, "Nanofabrication and Diffractive Optics for High-Resolution X-Ray Applications," J Vac Sci Technol B **18**, 2970-2975 (2000).

76. B. H. Koek, T. Chisholm, A. J. Vonrun, J. Romijn, and J. P. Davey, " An Electron-Beam Lithography Tool with a Schottky Emitter for Wide-Range Applications," *Microelectron. Eng.* **23**, 81-84 (1994).
77. E. H. Anderson, V. Boegli, and L. P. Muray, " Electron Beam Lithography Digital Pattern Generator and Electronics for Generalized Curvilinear Structures," *J. Vac. Sci. Technol. B* **13**, 2529-2534 (1995).
78. J. A. Liddle, P Naulleau, and G. Schmid, "Probe Shape Measurement in an Electron Beam Lithography System," *J. Vac. Sci. Technol. B* **22**, 2897-2901 (2004).
79. W. H. Press, B. P. Flannery, S. A. Teukolsky, and W. T. Vetterling, *Numerical recipes in C: the art of scientific computing*, 2nd edition. (Cambridge University Press, Cambridge, UK, 1992), pp.59-70.
80. P.A.F. Anastasi and R.E. Burge, "Preparation and characterisation of silicon nitride membranes for soft x-ray microscopy," in ref. 5, pp. 341-343.
81. J. W. Goodman, *Introduction to Fourier Optics* (McGraw-Hill, New York, 1996) 2nd ed. Edition
82. M. Born and E. Wolf, *Principles of Optics: Electromagnetic Theory of Propagation, Interference and Diffraction of Light* (Cambridge University Press, New York, 1999) 7th Edition, chapter 10.
83. J. W. Goodman, *Statistical Optics* (Wiley, New York, 2000), chapter 5.
84. Ref. 83, section 5.5.2.
85. P. H. van Cittert, "Die Wahrscheinliche Schwingungsverteilung in Einer Von Einer Lichtquelle Direkt Oder Mittels Einer Linse Beleuchteten Ebene," *Physica* **1**, 201-210 (1934); P. H. van Cittert, "Kohaerenz-Probleme," *Physica* **6**, 1129-1138 (1939).

86. F. Zernike, "The Concept of Degree of Coherence and Its Application to Optical Problems," *Physica* **5**, 785-795 (1938); F. Zernike, "Diffraction and Optical Image Formation," *Proc. Phys. Soc. Lond.* **61**, 158-164 (1948).
87. M. Born and E. Wolf, *Principles of Optics: Electromagnetic Theory of Propagation, Interference and Diffraction of Light* (Cambridge University Press, New York, 1999) 7th Edition, chapter 9.
88. Ref. 83, section 5.6.2.
89. K. K. H. Toh, "Two-Dimensional Images with Effects of Lens Aberrations in Optical Lithography," M.S. thesis, Department of Electrical Engineering and Computer Sciences, University of California, Berkeley (1988); K. K. H. Toh and A. R. Neureuther, "Identifying and Monitoring Effects of Lens Aberrations in Projection Printing," in *Optical Microlithography VI*, H. L. Stover Ed., *Proc. SPIE* **772**, pp. 202-209 (1987). The program can be assessed at <http://cuervo.eecs.berkeley.edu/Volcano/>
90. L. Rayleigh, *Phil. Mag.* **8**, 261 (1879). For a more contemporary description of the criterion, see E. Hecht, *Optics* (Addison-Wesley, Reading, Mass., 1998) 3rd Edition.
91. E. Hecht, *Optics* (Addison-Wesley, Reading, Mass., 1998) 3rd Edition, chapter 10.
92. M. Born and E. Wolf, *Principles of Optics: Electromagnetic Theory of Propagation, Interference and Diffraction of Light* (Cambridge University Press, New York, 1999) 7th Edition, chapter 8 and 10.
93. H. J. Levinson, *Principles of Lithography* (SPIE Press, Bellingham, WA, 2005), section 8.1.

94. J. M. Heck, D. T. Attwood, W. Meyer-Ilse and E. H. Anderson, "Resolution Determination in X-Ray Microscopy: An Analysis of the Effects of Partial Coherence and Illumination Spectrum," *J. X-Ray Sci. Technol.* **8**, 95-104 (1998).
95. Ref. 2, Chapter 4.
96. Ref. 19 and T. W. Barbee, "Multilayers for X-Ray Optics," *Opt. Eng.* **25**, 898-915 (1986). An excellent illustration of this deposition technique can be found in Ref.95, section 4.4.
97. See www.cxro.lbl.gov/multilayer/survey.html for current half-periods achieved and different multilayer material pairs.
98. J. C. Bravman and R. Sinclair, "The Preparation of Cross-Section Specimens for Transmission Electron-Microscopy," *J. Electron Microsc. Tech.* **1**, 53-61 (1984).
- 99 J. H. Underwood, E. M. Gullikson, and K. Nguyen, "Tarnishing of Mo/Si Multilayer X-ray Mirrors," *Appl. Opt.* **32**, 6985-6990 (1993).
100. Ref. 19, section 10.3. Also see Ref. 2, p. 102.
101. www.cxro.lbl.gov/opotical_contants.
102. D. C. Joy, "The Spatial Resolution Limit of Electron Lithography," *Microelectron. Eng.* **1**, 103-119 (1983).
103. H. Geng, M. Khan, F. Yanghua and F. Cerrina, "Comprehensive Model of Electron Energy Deposition," *J. Vac. Sci. Technol. B* **20**, 2666-2671 (2002).
104. T. H. P. Chang, "Proximity Effect in Electron-Beam Lithography," *J. Vac. Sci. Technol.* **12**, 1271-1275 (1975); S. A. Rishton and D. P. Kern, "Point Exposure Distribution Measurements for Proximity Correction in Electron Beam Lithography on a Sub-100 nm Scale," *J. Vac. Sci. Technol. B* **5**, 135-141 (1987); G. P. Watson,

- S. D. Berger, J. A. Liddle, L. A. Fetter, R. C. Farrow, R. G. Tarascon, M. Mkrtchyan, A. E. Novembre, M. I. Blakey, K. J. Bolan and L. Poli, "Precise Measurement of the Effective Backscatter Coefficient for 100-keV Electron-Beam Lithography on Si," *J. Vac. Sci. Technol. B* **13**, 2535-2538 (1995).
105. M. G. R. Thomson, "Incident Dose Modification for Proximity Effect Correction," **11**, 2768-2772 (1993); G. P. Watson, L. A. Fetter and J. A. Liddle, "Dose Modification Proximity Effect Correction Scheme with Inherent Forward Scattering Corrections," *J. Vac. Sci. Technol. B* **15**, 2309-2312 (1997); E. H. Anderson, D. L. Olynick, W. Chao, B. Harteneck and E. Veklerov, "Influence of Sub-100 nm Scattering on High-Energy Electron Beam Lithography," *J. Vac. Sci. Technol. B* **19**, 2504-2507 (2001).
106. D. Weiss, M. Peuker and G. Schneider, "Radiation-Enhanced Network Formation in Copolymer Galvanoforms for Diffractive Nickel X-Ray Optics with High Aspect Ratios," *Appl. Phys. Lett.* **72**, 1805-1807 (1998).
107. D. L. Olynick, B. D. Harteneck, E. Veklerov, M. Tendulkar, J. A. Liddle, A. L. D. Kilcoyne and T. Tyliczszak, "25 nm Mechanically Buttressed High Aspect Ratio Zone Plates: Fabrication and Performance," *J. Vac. Sci. Technol. B* **22**, 3186-3190 (2004).
108. E. Di Fabrizio, F. Romanato, M. Gentili, S. Cabrini, B. Kaulich, J. Susini and R. Barrett, "High-Efficiency Multilevel Zone Plates for Kev X-Rays," *Nature* **401**, 895-898 (1999).
109. R. H. Barker, "Group Synchronizing of Binary Digital Sequences," in *Communication Theory*, (Butterworth, London, 1953), pp. 273-287.

110. E. H. Anderson, D. Ha, J. A. Liddle, "Sub-Pixel Alignment for Direct-Write Electron Beam Lithography," *Microelectron. Eng.* **73-74**, 74-79 (2004).
111. S. Yasin, D. G. Hasko and H. Ahmed, "Fabrication of < 5 nm Width Lines in Poly(Methylmethacrylate) Resist Using a Water: Isopropyl Alcohol Developer and Ultrasonically-Assisted Development," *Appl. Phys. Lett.* **78**, 2760-2762 (2001).

Appendix A

The Mutual Intensity of Broadband Illumination in the Object Plane

In chapter 3, it was shown that the mutual intensity of the object illumination in the microscope is given by Eq. (3-26). This result was obtained under the assumption that narrowband radiation (quasi-monochromatic condition) is used. However, bending magnet radiation, utilized by the microscope, is polychromatic. To account for this effect, a rigorous derivation of the mutual intensity J_o^- in the object plane using the cross spectral density¹ is required, and is given in this appendix.

Let us introduce a function, called mutual coherence function², which describes both the spatial and temporal coherence of light waves, and is defined as

$$\Gamma_{12}(\tau) \equiv \langle U(P_1, t + \tau) U^*(P_2, t) \rangle \quad (\text{A-1})$$

$U(P_1, t + \tau)$ and $U(P_2, t)$ are the phasor amplitudes at two different positions, P_1 and P_2 , respectively, in a plane perpendicular to the propagation direction, with a time delay τ between them. $\langle \rangle$ and $*$ denotes the time (ensemble) average and complex conjugate, respectively. If τ is equal to zero (the two waves at P_1 and P_2 are measured at the same time), this function is equal to the mutual intensity, J , which measures only the spatial coherence [cf. Eq. (3-4)]:

$$\Gamma_{12}(0) \equiv \langle U(P_1, t) U^*(P_2, t) \rangle = J_{12} \quad (\text{A-2})$$

The Fourier transform of the mutual coherence function, given by

$$G(P_1, P_2; w) = \int_{-\infty}^{\infty} \Gamma_{12}(\tau) e^{-j2\pi w \tau} d\tau \quad (\text{A-3})$$

is commonly referred as the cross spectral density¹. By expressing $U(P_1, t)$ and $U(P_2, t)$ by their Fourier spectral components, the density can be shown to be equal to

$$G(P_1, P_2; w) = \langle V(P_1; w) V^*(P_2; w) \rangle, \quad \text{where} \quad V(P, w) = \int_{-\infty}^{\infty} U(P, t) \exp[-j2\pi w t] dt. \quad \text{For}$$

broadband illumination, such as in XM-1, this function is very useful in determining the coherence.

As radiation propagates, the associated cross spectral density changes. The evolution (or propagation) of the density can be shown^{3,4} to be described by

$$G(Q_1, Q_2; w) = \left(\frac{w}{cz} \right)^2 \iint_{\Sigma_P} \iint_{\Sigma_P} G(P_1, P_2; w) e^{-j \frac{2\pi w}{c} (r_{22} - r_{11})} ds_1 ds_2 \quad (\text{A-4})$$

where $G(P_1, P_2; w)$ is the cross spectral density in the plane Σ_P before propagation [Fig. A-1], and $G(Q_1, Q_2; w)$ is the density in the plane Σ_Q downstream. r_{11} (and likewise r_{22}) is the distance between point P_1 (P_2) and point Q_1 (Q_2) [Fig. A-1]. z , w , and c are the distance between the two planes, the spectral frequency, and the speed of light, respectively. The integral is summed over the area in the Σ_P plane twice, once for P_1 , another for P_2 .

If the radiation in the Σ_P plane is spatially incoherent, correlation only exists for two coincident points, and the cross spectral density is given by

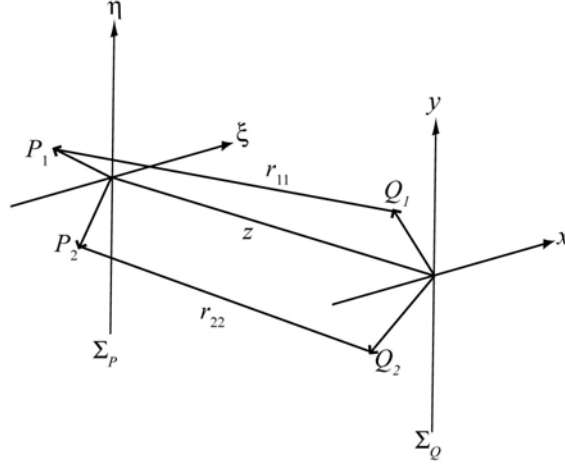


Figure A-1. Geometry for Eq. (A-4).

$$\begin{aligned}
 G(P_1, P_2; w) &= G(P_1, P_2; w) \delta(P_1 - P_2) \\
 &= \langle V(P_1; w) V^*(P_2; w) \rangle \delta(P_1 - P_2) \\
 &= \langle V(P_1; w) V^*(P_1; w) \rangle \delta(P_1 - P_2) \\
 &= \langle |V(P_1; w)|^2 \rangle \delta(P_1 - P_2) = S(P_1; w) \delta(P_1 - P_2)
 \end{aligned} \tag{A-5}$$

where $S(P_1; w)$ is the power spectrum at point P_1 . Substituting Eq. (A-5) into Eq. (A-4) yields

$$G(Q_1, Q_2; w) = \left(\frac{w}{cz} \right)^2 \iint_{\Sigma_P} S(P_1; w) e^{-j \frac{2\pi w}{c} (r_2 - r_1)} ds \tag{A-6}$$

where r_1 is the distance between point P_1 and Q_1 , and r_2 the distance between point P_1 and Q_2 . This is the counterpart of the van Cittert-Zernike theorem for spatially incoherent, broadband light source.

For the XM-1 microscope, which uses spatially incoherent radiation from a bending magnet, the cross spectral density of the illumination on the condenser zone plate can be obtained by use of Eq. (A-6)

$$G_c^-(\xi_1, \eta_1; \xi_2, \eta_2; w) = \left(\frac{w}{cz_{C1}} \right)^2 e^{-j \frac{2\pi w}{cz_{C1}} (\bar{\xi} \Delta \xi + \bar{\eta} \Delta \eta)} \int_{-\infty}^{\infty} \int_{-\infty}^{\infty} S_s(\alpha, \beta) e^{j \frac{2\pi w}{cz_{C1}} (\Delta \xi \alpha + \Delta \eta \beta)} d\alpha d\beta \quad (\text{A-7})$$

where the coordinate naming follows that in the chapter 3 (see Fig. A-2 for details).

$\bar{\xi} = (\xi_1 + \xi_2)/2$, $\bar{\eta} = (\eta_1 + \eta_2)/2$, $\Delta \xi = \xi_2 - \xi_1$, $\Delta \eta = \eta_2 - \eta_1$. $S_s(\alpha, \beta)$ is the power spectrum of the bending magnet.

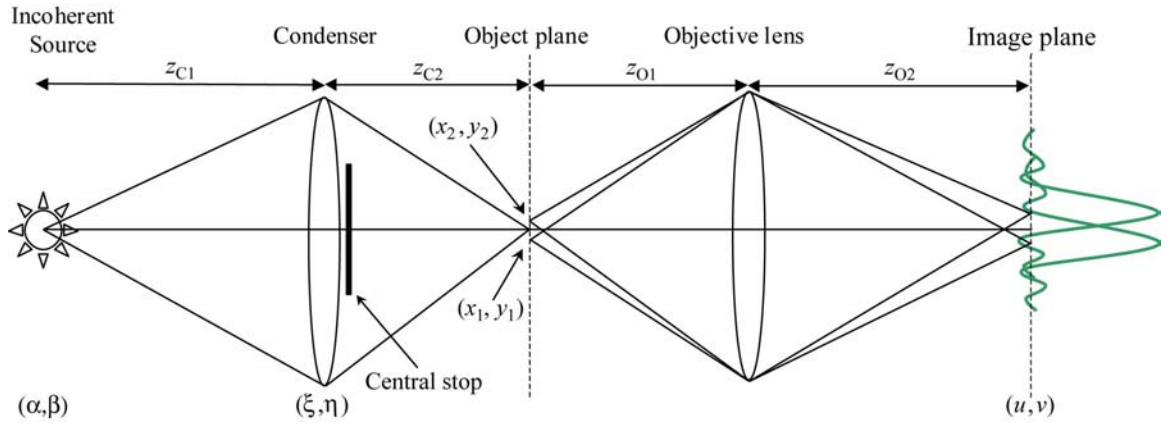


Figure A-2. The coordinate naming used in chapter 3.

The cross spectral density after propagating through the condenser is found to be equal to

$$G_c(\xi_1, \eta_1; \xi_2, \eta_2; w) = \tilde{P}_c(\xi_1, \eta_1; w) \tilde{P}_c^*(\xi_2, \eta_2; w) t_l(\xi_1, \eta_1; w) t_l^*(\xi_2, \eta_2; w) G_c^-(\xi_1, \eta_1; \xi_2, \eta_2; w) \quad (\text{A-8})$$

where $t_l(\xi, \eta; w) = \exp[-j \pi w (\xi^2 + \eta^2) / (cf_{CZP})]$ represents the condenser lens' quadratic phase function, f_{CZP} is the wavelength (or spectral frequency) dependent focal length of the

optic, and $\check{P}_c(\xi, \eta; w) = P_c(\xi, \eta) \exp(-jW(\xi, \eta; w))$ is the complex pupil function of the lens.

To find the cross spectral density in the object plane, Eq. (A-4) is utilized, and yield

$$G_o^-(x_1, y_1; x_2, y_2; w) = \left(\frac{w}{cz_{C2}} \right)^2 \iint_{\Sigma_P} \iint_{\Sigma_P} G_c(\xi_1, \eta_1; \xi_2, \eta_2; w) e^{-j \frac{2\pi w}{c} (r_{22} - r_{11})} ds_1 ds_2 \quad (A-9)$$

where in the paraxial approximation

$$r_{22} - r_{11} \approx \frac{1}{z_{C2}} [\bar{\xi} \Delta \xi + \bar{\eta} \Delta \eta + \bar{x} \Delta x + \bar{y} \Delta y - \bar{x} \Delta \xi - \Delta x \bar{\xi} - \bar{y} \Delta \eta - \Delta y \bar{\eta}]$$

Substituting Eq. (A-8) into Eq. (A-9) gives

$$\begin{aligned} G_o^-(x_1, y_1, x_2, y_2) &= \int_{-\infty}^{\infty} \int_{-\infty}^{\infty} \int_{-\infty}^{\infty} \int_{-\infty}^{\infty} d\xi_1 d\eta_1 d\xi_2 d\eta_2 \left(\frac{w}{cz_{C2}} \right)^2 G_c^-(\xi_1, \eta_1, \xi_2, \eta_2; w) \check{P}_c(\xi_1, \eta_1; w) \check{P}_c^*(\xi_2, \eta_2; w) \\ &\quad \times t_l(\xi_1, \eta_1; w) t_l^*(\xi_2, \eta_2; w) e^{-j 2\pi \frac{w}{cz_{C2}} (\bar{x} \Delta x + \bar{y} \Delta y)} e^{-j 2\pi \frac{w}{cz_{C1}} (\bar{\xi} \Delta \xi + \bar{\eta} \Delta \eta)} \\ &\quad \times e^{j 2\pi \frac{w}{cz_{C2}} [\bar{\xi} \Delta x + \bar{\eta} \Delta y + \bar{x} \Delta \xi + \bar{y} \Delta \eta]} \end{aligned} \quad (A-10)$$

To obtain the mutual intensity J_o^- in the object plane from the cross spectral density G_o^- , one can use the fact that the cross spectral density is the Fourier transform of the mutual coherence function, which in turn is related to the mutual intensity through Eq. (A-2), i.e.,

$$\begin{aligned} \Gamma(P_1, P_2; \tau) &= \int_{-\infty}^{\infty} G(P_1, P_2; w) e^{j 2\pi w \tau} dw \\ J(P_1, P_2) &= \Gamma(P_1, P_2; 0) = \int_{-\infty}^{\infty} G(P_1, P_2; w) dw \end{aligned}$$

Thus, J_o^- is equal to

$$\begin{aligned}
 J_o^-(x_1, y_1, x_2, y_2) = & \int_{-\infty}^{\infty} \int_{-\infty}^{\infty} \int_{-\infty}^{\infty} d\xi_1 d\eta_1 d\xi_2 d\eta_2 \int_{-\infty}^{\infty} \left(\frac{w}{cz_{C2}} \right)^2 G_c^-(\xi_1, \eta_1, \xi_2, \eta_2; w) \bar{P}_c(\xi_1, \eta_1; w) \bar{P}_c^*(\xi_2, \eta_2; w) \\
 & \times t_l(\xi_1, \eta_1; w) t_l^*(\xi_2, \eta_2; w) e^{-j2\pi \frac{w}{cz_{C2}} (\bar{x}\Delta x + \bar{y}\Delta y)} e^{-j2\pi \frac{w}{cz_{C1}} (\bar{\xi}\Delta \xi + \bar{\eta}\Delta \eta)} \\
 & \times e^{j2\pi \frac{w}{cz_{C2}} [\bar{\xi}\Delta x + \bar{\eta}\Delta y + \bar{x}\Delta \xi + \bar{y}\Delta \eta]} dw
 \end{aligned} \tag{A-11}$$

Finally, due to the use of the condenser-pinhole monochromator, the illumination spectrum in the object plane has a relatively small bandwidth (monochromaticity of 700) [section 2.3]. This effect can be approximated in the first order by limiting the spectral integration in Eq. (A-11) to within the range of $\bar{w} - \Delta w/2$ to $\bar{w} + \Delta w/2$, where \bar{w} and Δw are, respectively, the center optical frequency and bandwidth of the monochromization passband. Thus J_o^- is given by

$$\begin{aligned}
 J_o^-(x_1, y_1, x_2, y_2) = & \int_{-\infty}^{\infty} \int_{-\infty}^{\infty} \int_{-\infty}^{\infty} d\xi_1 d\eta_1 d\xi_2 d\eta_2 \int_{\bar{w}-\Delta w/2}^{\bar{w}+\Delta w/2} \left(\frac{w}{cz_{C2}} \right)^2 G_c^-(\xi_1, \eta_1, \xi_2, \eta_2; w) \bar{P}_c(\xi_1, \eta_1; w) \bar{P}_c^*(\xi_2, \eta_2; w) \\
 & \times t_l(\xi_1, \eta_1; w) t_l^*(\xi_2, \eta_2; w) e^{-j2\pi \frac{w}{cz_{C2}} (\bar{x}\Delta x + \bar{y}\Delta y)} e^{-j2\pi \frac{w}{cz_{C1}} (\bar{\xi}\Delta \xi + \bar{\eta}\Delta \eta)} \\
 & \times e^{j2\pi \frac{w}{cz_{C2}} [\bar{\xi}\Delta x + \bar{\eta}\Delta y + \bar{x}\Delta \xi + \bar{y}\Delta \eta]} dw
 \end{aligned}$$

where

$$G_c^-(\xi_1, \eta_1, \xi_2, \eta_2; w) = \left(\frac{w}{cz_{C1}} \right)^2 e^{-j2\pi \frac{w}{cz_{C1}} (\bar{\xi}\Delta \xi + \bar{\eta}\Delta \eta)} \int_{-\infty}^{\infty} \int_{-\infty}^{\infty} S_s(\alpha, \beta) e^{j2\pi \frac{w}{cz_{C1}} (\Delta \xi \alpha + \Delta \eta \beta)} d\alpha d\beta$$

References

1. M. Born and E. Wolf, *Principles of Optics: Electromagnetic Theory of Propagation, Interference and Diffraction of Light* (Cambridge University Press, New York, 1999) 7th expanded Edition, section 10.3.2.
2. J. W. Goodman, *Statistical Optics* (Wiley, New York, 2000), section 5.2.1 and 5.2.2.
M. Born and E. Wolf, *Principles of Optics: Electromagnetic Theory of Propagation, Interference and Diffraction of Light* (Cambridge University Press, New York, 1999) 7th expanded Edition, section 10.3.1. The definition of mutual coherence function can be better appreciated in the context of Young's interference experiment.
3. J. W. Goodman, *Statistical Optics* (Wiley, New York, 2000), section 5.4.3. Goodman shows that the propagation of cross spectral densities obey the same propagation laws as do mutual intensities .
4. Y. Ohtsuka, "Is the Van Cittert-Zernike Theorem Applicable to Spatially Incoherent Broadband Spectral Source?" *Opt. Rev.* **5**, 27-29 (1998).

Appendix B

Zone Plate and Test Object Fabrication Processes

To complete the discussion of resolution measurements in chapter 5 and 6, the details of fabrication processes specific for the zone plates and test objects used are described below. This appendix is divided into three parts: micro zone plate fabrication, condenser zone plate fabrication, and test object fabrication. For easy referencing to the corresponding sections in the dissertation main text, the following lists the various sections in this appendix:

Micro zone plates

B.1.1	35 nm micro zone plates in the knife-edge experiment [section 5.2]	156
B.1.2	25 nm micro zone plates [section 5.3]	157
B.1.3	25 nm, higher aspect-ratio micro zone plates [section 5.5]	159
B.1.4	15 nm micro zone plates using the overlay nanofabrication technique [section 6.4]	161

Condenser zone plates

B.2.1	54 nm condenser zone plate in the knife-edge experiment [section 5.2]	165
B.2.2	60 nm condenser zone plate [section 5.5]	166
B.2.3	40 nm condenser zone plate [section 6.6]	168

Test objects

B.3.1	Test object of line and space patterns [section 5.4]	173
-------	--	-----

B-1 Micro zone plate fabrication

B.1.1 The micro zone plate of 35 nm outermost zone width in knife-edge experiment

The 35 nm micro zone plate, used in the knife-edge experiment [section 5.2], was fabricated using the negative-tone e-beam resist, hexaacetate *p*-methylcalix[6]arene, a calixarene derivative. This non-polymer material, made of cyclic structures with molecular sizes of about 1 nm in diameter, showed very high resolution and exhibited high durability to halide plasma etching¹. The 35 nm micro zone plate was our first attempt for using this resist.

An array of such zone plates, with 35 nm outermost zones, were fabricated using the single-layer resist process. First, a solution of 4% calixarene was prepared by dissolving 1 g of 4-Methyl-1-acetoxycalix[6]arene powder (TCI America, Portland, OR) in 24 g of *o*-dichlorobenzene. However, the powder was not readily dissolved in *o*-dichlorobenzene solution. To solve the problem, 5 g of dichloromethane was added to the solution with for better solubility. A micro zone plate substrate with 100 nm thick silicon nitride membrane windows was coated by evaporation with the 5nm Cr/12 nm Au plating base. The substrate and the plating base are our standard and discussed further in section 2.4. The coated substrate was dehydrated on a hot plate at 110 °C for 5 min. The wafer was then spin-coated with calixarene solution at 3000 rpm for 45 seconds, then baked in oven at 170 °C for 30 minutes, to form a 60 nm thick resist layer on the silicon nitride membrane windows. Using the Nanowriter, the wafer was then exposed with a 35 nm zone plate pattern in high resolution condition at 100 keV, a beam current of 0.5 nA, and a dose around 20 mC/cm². The high resolution exposure condition and the low resist

sensitivity resulted in relatively long exposure, about 5 minutes for each 45- μm -diameter zone plate. After the exposure, the wafer was developed in xylenes for 30 seconds at room temperature, rinsed by isopropanol (IPA) for 30 seconds, and blown dry by dry nitrogen. At times, calixarene residue remained in the unexposed areas, and prevented the areas from being electroplated in the following step. To remove the residue, the wafer was dry-etched with oxygen at low power, for 90 seconds. This step is referred to below as “de-scum,” and is applied in most cases before electroplating. The wafer was next electroplated with nickel to the full resist thickness, to form the final metal zone plate structure. Pulse plating with a 50 ms switching time and 50% duty cycle was used, with our standard nickel sulfate solution (Sulfamex, Enthone-OMI Inc., New Haven, CT) at 35°C and a rms current density of 0.7 mA/cm². The plating condition, which was used in all the nickel electroplating in this dissertation, resulted in a plating rate of about 10 nm/min, and produced a low stress film and small grains. Because only one electric contact point was used in the plating, the wafer was rotated four times in the process to ensure uniform plating across the wafer. After the plating, the fabrication process was completed by stripping of the unexposed resist using oxygen dry etching for 20 minutes. The final zone plates had 318 zones, 45 μm diameter, and a focal length of 650 μm at 2.4 nm wavelength.

B.1.2 The micro zone plates with 25 nm outermost zone width used in section 5.3

For further improvement of the microscope’s resolution, zone plates with outer zone widths of 25 nm were fabricated with thinner calixarene layers [section B.1.1]. Reduction of resist thickness was determined in general to permit fabrication of smaller

features at 100keV. This we believe is because the small thickness reduces degradation of the resolution caused by electron scattering and secondary electron generation in the resist layer².

Micro zone plates with 25 nm outermost zone width, 628 zones, and a diameter of 63 μm were designed, giving a focal length of 650 μm at 2.4 nm wavelength, the same focal length as the 35 nm MZP above. The 25 nm micro zone plates were fabricated using a similar process to that used for the 35 nm zone plates [section B.1.1]. A solution of 2.5% wt. calixarene was prepared by dissolution of 4-Methyl-1-acetoxycalix[6]arene powder in o-dichlorobenzene solvent. Again 5 g of dichloromethane was added to the solution for better solubility. A standard micro zone plate wafer with the evaporated standard plating base was spin-coated with the calixarene solution at 2000 rpm for 45 seconds, yielding a resist thickness of 30 nm after baking. The Nanowriter was then used to write 25 nm zone plate patterns, using high resolution beam conditions at 100 keV and 0.5 nA beam current, at a dose of about 27 mC/cm². Exposure of each zone plate was about 10 minutes. The wafer was developed and dry-etched after the exposure. The final zone plate patterns were formed by electroplating in our standard gold bath, BDT 510, (Enthone-OMI Inc., West Haven, CT), at 40 °C, to the resist full thickness. The pulse plating used for the nickel plating [section B.1.1] was also used here for low stress and small grains. The rms current density was 1mA/cm², resulting in a plating rate of 100 nm/min. In the process of plating, the wafer was rotated, as done for the 35 nm zone plates, to acquire uniform plating across the wafer. To complete the zone plate fabrication, the resist structure was removed by an acetone wet etch of 10 min, followed

by a 3 minute oxygen dry etch. The aspect ratio of the resultant gold zone structure was about 1:1.

B.1.3 The higher aspect-ratio micro zone plate with 25 nm zone width used in section 5.5

For higher efficiency zone plates, we have fabricated 25-nm-outer-zone-width micro zone plates (300 zones, 30 μm diameter) using a bilayer process [section 2.4]. The deep ultraviolet (DUV) resist AZPN114 (Sumitomo Chemical America, Inc., New York) is used for the underlying polymer layer. For the pattern recording, hydrogen silsesquioxane ($\text{HSiO}_{3/2}$), referred to in this dissertation as HSQ (Fox-15, Dow Corning, Midland, MI), is used. The HSQ, designed as a low dielectric-constant material, was reported^{3,4} to behave as a negative-tone e-beam resist, and exhibit resolution about the same as calixarene [B.1.1] but a 20 times improvement in sensitivity⁵. It also showed small linewidth fluctuation and roughness^{3,4}.

To start the fabrication process, the standard plating base (5nm Cr/12 nm Au) was evaporated on our standard micro zone plate substrate [section 2.4]. The wafer was then coated with 70 nm thick cross-linked polymer (30% wt. AZPN114 spin-coated at 6000 rpm for 45 seconds), and baked on an at-temperature copper plate in a 170 °C oven for 15 min for cross-linking the resist. Use of the copper plate improves thermal conduction to the wafer. Next, the wafer is coated with 30 nm thick HSQ (1.8% wt. HSQ spin-coated at 4000 rpm, followed by 5 min oven bake at 170C, also on copper plate). The wafer was then exposed at 100 keV with 0.5 nA beam current. The exposure dose used ranged from 2800 $\mu\text{C}/\text{cm}^2$ to 4000 $\mu\text{C}/\text{cm}^2$, to ensure inclusion of the proper exposure dose. After the

exposure, the wafer was developed with 2.38% wt. tetramethyl ammonium hydroxide (LDD-26W, Rohm and Haas Electronic Materials, Marlborough, MA) at room temperature for 1 minute, rinsed by ultra pure de-ionized water, and blown dry using dry nitrogen. The exposed pattern is then transferred from the HSQ layer to the underlying AZPN114 layer, using cryogenic plasma etch. The etch was performed using the Oxford Plasmalab 100 ICP 380 etcher. The etching recipe for the cryogenic etch used 1.5 mTorr chamber pressure, 10 sccm O₂, 20 W RF power, 350 W ICP power, 15 Torr He on the backside of the wafer, and -100 °C for the platen. Etching rate of AZPN114 was approximately 100 nm/min, with approximately 60:1 selectivity over HSQ. Here, etching of 1 minutes and 20 seconds was used, to insure thorough removal of the polymer in the clear zones and good electrical contact of the underlying plating base to the plating bath in the next step.

After the etching, the wafer was electroplated in nickel to a thickness of about 80 nm, using the standard plating process [section B.1.1]. The outer zone width aspect ratio achieved was slightly more than 3:1. As the final step, the bilayer resist structure was removed to obtain the desired zone plates (HSQ strip in 40:1 buffered hydrofluoric acid solution for 5 seconds, followed by AZPN114 oxygen plasma strip).

B.1.4 Micro zone plates of 15 nm outer zones fabricated using the overlay nanofabrication technique [section 6.4]

The fabrication has three lithographic steps: alignment mark fabrication, zone set I fabrication, and zone set II fabrication [Fig. B-1]. To start the alignment mark fabrication, a plating base bilayer, 12 nm Au on top of 5 nm Cr (Cr/Au), was evaporated on the front side of a standard micro zone plate wafer [section 2.4]. The wafer was then spin-coated with 2 wt.% polymethyl methacrylate, or PMMA (950 PMMA C2, Nano™ Micro Chem, Newton, MA) at 4000 rpm for 45 seconds, then baked on an at-temperature copper plate in 170 °C oven for 15 minutes, to form a 100 nm thick resist layer on the silicon nitride membrane windows.

For accurate feature placement, the electron beam deflection of the Nanowriter was calibrated with gold “islands” [section 2.4] before the alignment mark exposure. A deflection accuracy of less than 2 nm, one beam step in this experiment, was achieved. Four variants of Barker marks [FigB-2], each of which were the rotated copies of the another, and a similar set closer to the center, were then exposed just outside the windows with 100 keV electrons. The marks were exposed to a 5 by 5 array of windows on the micro zone plate wafer. Stage movement was required for traversing between the windows, but not for the exposure of the (Barker) alignment mark sets at individual windows, which were smaller than the beam deflection field (131.072 μm). The avoidance of stage movement is significant, as it minimizes the inaccuracy of relative mark positions within the sets. After exposure was completed, the wafer was developed in 3:1 ratio of isopropanol (IPA) and methyl isobutyl ketone (MIBK) at 21°C for 40

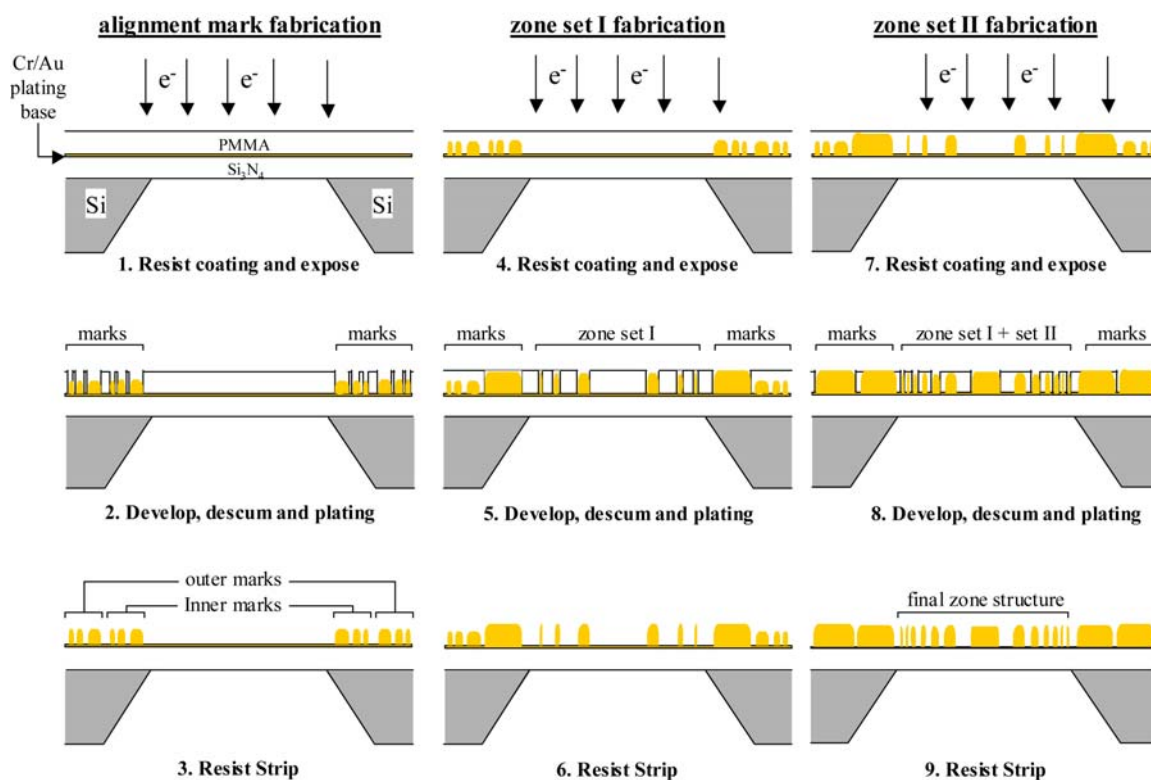


Figure B-1. Illustration of the overlay nanofabrication process used for the 15-nm micro zone plates. The process has three sequential lithographic steps: alignment mark fabrication (left column), first zone set fabrication (middle column), and second zone set fabrication (right column).

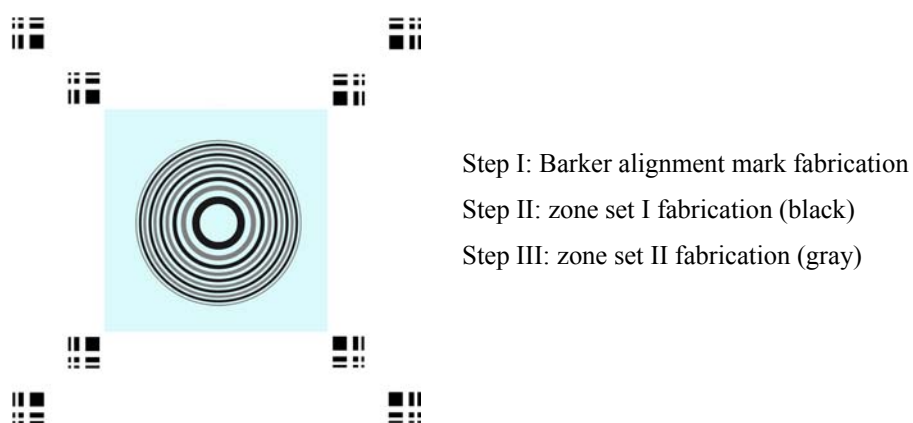


Figure B-2. Pattern layout in the overlay fabrication process. In the first lithographic step, two Barker alignment mark sets are fabricated outside the membrane window (light blue). Zone set I and set II are then fabricated, using the Barker marks for fine alignment calibration.

seconds, rinsed with IPA, and carefully blown dry using nitrogen. The wafer was subsequently etched in oxygen plasma at low (RF) power for 15 seconds to remove the minute partially developed resist residue (“scum”) in the exposed regions. After the resist development and scum removal, the wafer was then electroplated with 50 nm thick gold, which yields good contrast in the backscatter mode at the Nanowriter. The standard plating process [section B.1.2] was used for the electroplating. To complete the alignment mark fabrication, the resist was subsequently removed using the solvent, dichloromethane, and low power oxygen plasma etch.

Next, the zone set I was fabricated. To this end, a fresh 100 nm thick PMMA layer was spin-coated on the wafer, using the same process steps as in the alignment mark fabrication. As before, the wafer was then mounted on a wafer holder and loaded in the Nanowriter. To account for any slight rotation and shift of the wafer introduced during the mounting, the stage movement was calibrated with respect to the wafer orientation. This was accomplished using an automatic mark detection algorithm^{*}, which was used to measure the positions of the alignment marks outside the four corner (furthest separated) windows of the (5 x 5) window array. Using the positions, the Nanowriter subsequently computed the rotation, scaling, and shift of the wafer, and applied the results to the stage coordinate correction polynomial. With the stage subsystem calibrated, zone set I was then exposed at individual windows. To achieve high placement accuracy, before the pattern exposure at *each* window, the beam deflection positioning was further refined, by

^{*} The algorithm uses the same principle employed by the automatic alignment algorithm. For details on the automatic alignment algorithm, please see Ref. 6.

application of an internally developed, automatic alignment algorithm⁶ to the inner alignment marks outside the window. In this algorithm, images of the four inner alignment marks were first obtained, and the displacement of the marks from their ideal positions due to small beam deflection inaccuracy was calculated using auto/cross-correlation methods⁶. Based on the displacement, the proper correction to the beam deflection was then determined. For the best result, this process was iterated twice, and achieved a *sub-pixel* beam deflection accuracy of less than 2 nm. Utilizing such a beam deflection control, zone set I was then written to the window. The exposure took 10 seconds. Similar to the mark fabrication, after exposure, the wafer was developed, “descumed”, and electroplated using our standard process, forming an 80-90 nm thick gold structure. Again, the resist was removed using dichloromethane solvent and low power oxygen plasma etch.

A fresh 100 nm thick PMMA resist was then coated again on the wafer, using the same process as in the last two process steps, for preparation of zone set II exposure. Following the exact fabrication processes for zone set I, the stage of the Nanowriter was calibrated. Through the use of the automatic alignment algorithm, the beam deflection was fine-calibrated before the pattern exposure at each window, in order to achieve high position accuracy for zone set II with respect to the marks, and thus to the previously exposed even ring patterns. The unused outer alignment marks were used in the stage calibration and deflection fine-calibration, as the inner marks used for zone set I were filled with gold during electroplating of zone set I, and thus were not available for set II. After development and “descum”, the wafer was electroplated again with 80-90 nm thick

gold. Zone set I could not be plated, as they were covered by the resist. Using dichloromethane and oxygen plasma etch, the resist was removed, forming the desired zone plate structure.

B.2 Condenser zone plate fabrication

B.2.1 Condenser zone plate of a 54 nm outer zone used in knife-edge experiment

The condenser zone plate, used in the knife-edge experiment [section 5.2], was fabricated using the single-layer resist process [section 2.4], with polymethyl methacrylate (PMMA), a commonly used e-beam resist. The fabrication process started with evaporation of a thin plating base of 5 nm chromium and 12 nm gold onto the standard condenser wafer [section 2.4]. The wafer was then cleaned by immersion of the wafer in RCA solution (5:1:1 di-onized water:30% hydrogen peroxide:29% ammonium hydroxide) at 70 °C for 10 minutes. The wafer was then rinsed with ultra pure de-ionized water and blown dry with dry nitrogen. The wafer was further dehydrated by heating on a hot plate at 110 °C for 5 minutes. The wafer was then cooled and 2.7% wt.% PMMA (950 PMMA C2, Nano™ Micro Chem, Newton, MA) was spin-coated onto the plating base. To drive off the resist solvent, the wafer was baked at 170 °C for 90 minutes, yielding a resist thickness of 230 nm. The wafer was then loaded into the Nanowriter, where 100 keV electrons at about 2.3 nA beam current were used to write the zone plate pattern. The exposure time for this large, 9 mm diameter structure was approximately 48 hours. After the exposure, the wafer was developed at 21 °C in 3:1 ratio of isopropanol (IPA) and methyl isobutyl ketone (MIBK) for 40 seconds, rinsed with IPA, and carefully blown dry. Because the PMMA is positive tone, the whole wafer front side except the

exposed areas was covered with the resist. In order to electroplate the wafer, a circular band of about 1 inch in width along the wafer's edge was cleared of resist for electric contact by reactive ion etching. In the process, the wafer center was covered to protect the zone plate. The etching used oxygen gas and took 16 minutes. The cover was then removed and the whole wafer was etched at low power with oxygen plasma for 90 seconds to remove any resist residue remained in the exposed area. The wafer was then electroplated with nickel, using the plating annulus for electric contact. The plating procedure was the same as for the micro zone plates, and a thickness of about 200 nm was obtained. After the formation of the metal zone plate structure, the resist mold structure was removed by acetone and reactive ion etching. The final condenser zone plate had an aspect ratio of 4:1.

B.2.2 Condenser zone plate used in section 5.5

The condenser zone plate used in section 5.5, which had 41700 zones and 10 mm diameter, was fabricated using a single-layer-resist process. First, a titanium layer of 5 nm, instead of chromium, was formed by evaporation on our standard condenser zone plate substrate. The replacement was due to the use of the condenser in some microscope's applications at the chromium L edge (around 570 eV). A 12 nm gold layer was then evaporated on the substrate to form the plating base. Transmission of the plating base at 600 eV photon energy used in the experiment below was 90%, which combined with the 100 nm thick silicon nitride membrane yielded a transmission of 80%. Next, a gold layer of 200 nm was evaporated on the backside of the wafer. The gold layer provided a thermal conduction path from the silicon nitride membrane windows to the

neighboring silicon backing substrate, allowing even resist coating across the entire wafer[†]. This step is important for obtaining uniform resist coating on condenser zone plates because of the large size of the thin membrane windows (5 mm) [see Fig. 2-6].

After forming the needed metal layers, the wafer was spin-coated with 5% KRS-XE, a positive-tone chemically amplified resist⁷ developed by IBM, Yorktown Heights, NY. This sensitive resist had a resolution of about 50 nm. The spin speed was 1000 rpm. The wafer was subsequently baked on a hot plate at 110 °C for 5 min, resulting in a resist layer of about 170 nm in thickness. The backside gold layer was then removed, using a gold etch solution, potassium iodide (GE-8148, Transene Co. Inc., Danvers, MA), to eliminate the proximity effect in zone plate exposure caused by this gold layer.

The wafer was then mounted on a transmission wafer holder of the Nanowriter system. Calibration of the beam deflection and stage movement were carefully performed, to ensure accurate zone placement throughout the large zone plate. Following the calibration, the zone plate pattern was exposed at 100 keV and 0.5 nA beam current. The exposure dose used was 53.5 $\mu\text{C}/\text{cm}^2$, and the exposure took about 2 days. After the exposure, the wafer was hydrated in ambient air for 30 minutes to allow the chemical reactions of the resist to complete. The wafer was subsequently developed in 2.38% wt. tetramethyl ammonium hydroxide solution (LDD-26W, Rohm and Haas Electronic Materials, Marlborough, MA) for 30 seconds, rinsed with ultra pure de-ionized water, and blown dry carefully. The resist was measured to be 170 nm thick using a

[†] Resist coating thickness depends on the evaporation rate of the resist solvent, which is a function of the temperature of the substrate. Poor thermal conductivity of the thin silicon nitride windows allows different evaporation rate of the solvent at various membrane locations, which results in non-uniform resist coating.

profilometer. Because the resist tone was positive, the whole wafer front side except the exposed areas was covered with the resist. In order to electroplate the wafer, a circular band of about 1 inch in width along the edge of the wafer was cleared of resist by application of acetone to the region while the wafer was spinning in a spinner. It is critical that the plating annulus is thoroughly clear of resist, since for a given electric current, the plating rate depends on the area exposed to the plating solution. Thus, following the acetone etch, the wafer was dry etched for 45 seconds at low power with oxygen plasma to remove any resist residue in the annular area. After the formation of annulus, the wafer was then electroplated with nickel. The standard plating process [section B.1.1] was utilized here. A nickel thickness of 140 nm was achieved by the electroplating. The wafer was then dry etched in oxygen for 6 minutes to remove the resist structure. Measurement with the profilometer after the plasma etch revealed that the metal zone structure had a thickness of 120 nm.

B.2.3 Fabrication of condenser zone plate of 40 nm outer zones

The 40 nm condenser zone plate, discussed in section 6.6, was fabricated using a positive-tone e-beam resist, ZEP 520 (Zeon Corporation, Tokyo). It has a relatively good resolution, about 30 nm, and exposure dose between 80 mC/cm² and 110 mC/cm² at 100 keV, approximately twice of that of the KRS-XE resist used for the previous condenser zone plate [section B.2.2 and 5.5]. In order to obtain modest efficiency from the zone plate, the “opaque” zones were designed to be formed by electroplating gold, with a thickness of about 150 nm, which can yield a first order diffraction efficiency of 11% at 516 eV. Such a structure, with outer zone widths of 40 nm, required an aspect ratio close

to 4:1 at the outer zones. To realize this, a resist structure of the same (or slightly larger) aspect ratio was needed. This, based on our experience, however, is difficult to be fabricated with no resist collapse. To mitigate resist collapse, bridges supporting the neighboring resist zones [section 6.2] were designed⁸ and utilized in the outer zone region of this zone plate. For the positive tone resist ZEP, where after the development the resist in the exposed region is removed and unexposed resist remains, use of the buttresses technique requires the exposed patterns to be made of broken zone segments, rather than of full zones as in the typical zone plates [Fig. B-3]. With such patterns, resist “buttresses” is formed between the resist (unexposed zones) after development for the mechanical support. Note that due to the broken segments in the exposed patterns, the outer zone region of the final zone plate structure, formed by electroplating, was composed of broken segments. This, however, does not affect the imaging performance of the zone plates, as the buttressed region is small compared to the whole zone plate. For this zone plate, the interspersed buttress pattern, which has an alternating buttress distribution between neighboring zones [Fig. B-3], was used. This pattern has experimentally shown to provide the maximum support with minimum buttress numbers.

The gaps in the exposed pattern, however, increased the computation time during the zone plate exposure, making the exposure longer. For this zone plate, with a diameter of 9 mm, the exposure time took 4 days. Zone placement could be compromised by any drift in the Nanowriter settings, such as the beam positioning, in the course of 4 days. To minimize the system drift, a scheme of automatic system calibration during the exposure

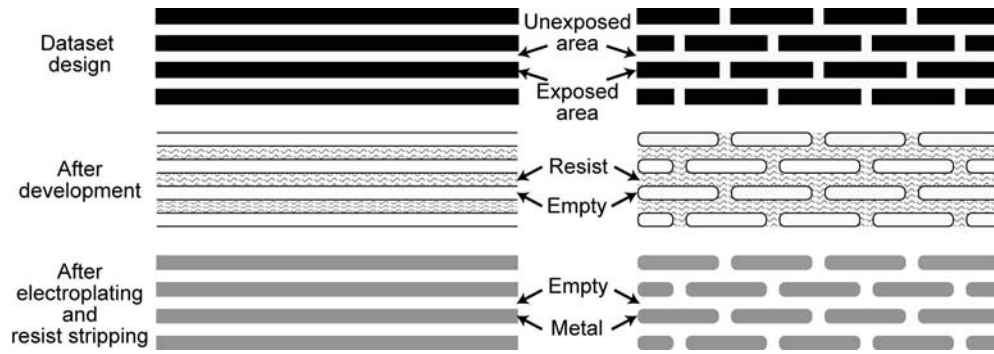


Figure B-3. Comparison of the typical zone plate patterns (left) and the buttressed zone plate patterns designed for positive-tone resist (right). Because of the positive-tone resist, the exposed pattern (shown by the dataset design) in the buttress case contains intermittent gaps (top right) in order to form the desired buttresses (middle right). The final zone structure after electroplating is composed of broken zone segments (bottom right). For this zone plate, the buttress pattern is only utilized in the outer zone region, where the aspect ratio is the highest (4:1). Thus, the buttresses have minimal effects to the zone plate imaging performance. Note that the interspersed buttress pattern shown here, which was utilized in the 40 nm condenser zone plate fabrication, has shown experimentally to provide the maximum support with minimum buttress numbers.

was developed. In this scheme, before the zone plate exposure, a Barker mark was fabricated at the upper left corner of the second quadrant window. During the zone plate exposure, the Nanowriter would in every few hours scan the mark, compare the mark position in the image against the designed position, and calibrate the displacement, scaling and orthogonality of the beam deflectors, which are the main contribution of the system drift.

Here are the details of the fabrication process. As discussed above, the process is divided into two parts: mark fabrication and zone plate fabrication. The mask fabrication started with evaporation of a thin plating base of 5 nm chromium and 12 nm gold onto the standard condenser wafer [section 2.4]. A gold layer of 200 nm was then evaporated on the backside of the wafer. The gold layer provided a thermal conduction path from the

silicon nitride membrane windows to the neighboring silicon backing substrate, allowing even resist coating across the entire wafer[‡]. Because of the large size of the thin membrane windows (5 mm) [see Fig. 2-6], this step is important for obtaining uniform resist coating on condenser zone plates.

After forming the needed metal layers, the wafer was spin-coated with 15% wt. AZPN114 (Sumitomo Chemical America, Inc., New York) at 4000 rpm for 45 seconds to form a polymer layer of less than 50 nm. This layer was served as the adhesion layer of the ZEP 520 resist. The polymer was then cross-linked by ultraviolet exposure in air for 10 minutes. The wafer was then spin-coated with 33% wt. ZEP 520 resist at 1000 rpm, and baked on an at-temperature copper plate in an 170 °C oven for 5 min, to form a 150 nm thick ZEP resist layer.

The wafer was then mounted on a transmission wafer holder of the Nanowriter system. Using the Nanowriter, the Barker mark pattern was exposed at 100 keV and 0.5 nA beam current, with an exposure dose of 80 $\mu\text{C}/\text{cm}^2$. After the exposure, the wafer was developed in xylenes for 3 minutes. The wafer was then submersed in 9:1 methyl isobutyl ketone (MIBK): isopropanol (IPA) solution for 10 seconds, followed by rinse in ultra pure de-ionized water. The use of the MIBK and IPA mixture is to clear the xylenes off the wafer. After the water rinse, the wafer was blown dry carefully with nitrogen.

[‡] Resist coating thickness depends on the evaporation rate of the resist solvent, which is a function of the temperature of the substrate. Poor thermal conductivity of the thin silicon nitride windows allows different evaporation rate of the solvent at various membrane locations, which results in non-uniform resist coating.

In order to form the mark pattern in metal, the exposed pattern needed to be transferred into the underlying AZPN layer for electric contact with the plating base. For this, the wafer was then processed using cryogenic plasma etch. The recipe used was the same for the high aspect ratio micro zone plate [section B.1.3]: 1.5 mTorr chamber pressure, 10 sccm O₂, 20 W RF power, 350 W ICP power, 15 Torr He on the backside of the wafer, and –100 °C for the platen. The etch was performed for 30 seconds, using the Oxford Plasmalab 100 ICP 380 etcher. Because the resist tone was positive, the whole wafer front side except the exposed areas was covered with the resist. In order to electroplate the wafer, a circular band of about 1 inch in width along the edge of the wafer was cleared of resist by etching the wafer using the cryogenic etch recipe, with the wafer center covered. The etch of 90 seconds was performed. Following the fabrication of the contact annulus, the wafer was electroplated in gold bath, using the standard gold plating process [section B.1.2], to form the mark. Since the mark was for system calibration, a gold layer of 50 nm was formed, which was sufficiently for good image contrast in the Nanowriter. To complete the mark fabrication and prepare for the zone plate exposure, the resist structure was removed using low power oxygen plasma etch. The low power was critical, as high RF power can sputter the deposited gold.

To start the zone plate fabrication, the wafer was spin-coated with AZPN114 and ZEP 520 solutions, using the same process steps as in the above mark fabrication. A ZEP layer of 150 nm thick on top of less than 50 nm thick AZ layer was formed above the plating base. To eliminate the proximity effect in the zone plate exposure caused by the backside gold layer, the gold material was then removed, using a gold etch solution,

potassium iodide (GE-8148, Transene Co. Inc., Danvers, MA). The wafer was then mounted on a transmission wafer holder of the Nanowriter system. Calibration of the beam deflection and stage movement were carefully performed, to ensure accurate zone placement throughout the large zone plate. Following the calibration, the zone plate pattern was exposed at 100 keV and 0.5 nA beam current, with an exposure dose of 80 $\mu\text{C}/\text{cm}^2$. For consistency, the exposure began with calibration of the beam deflectors using the fabricated Barker mark. With the new deflector parameters, the zone plate was then exposed. As mentioned above, the deflector calibration was performed every five to six hours, to ensure stable writing performance. In addition, to obtain the highest quality zone plate, the outer region of the condenser, which required higher beam quality for the smallest zones, was written first, and the larger zones near the center were exposed later.

After the exposure, the wafer was developed and etched using the same process steps as in the above mark fabrication. After the formation of the plating annulus, the wafer was electroplated in gold, using the standard plating process, until the full resist thickness was reached. To complete the whole fabrication process, the resist structure was removed using low power oxygen plasma etch.

B.3 Test object fabrication

B.3.1 Fabrication of line test objects discussed in section 5.4

Using the HSQ [B.1.3], the test pattern was fabricated by the following process: the standard Cr/Au plating base (section 2.4) was evaporated on a 500 μm thick window substrate with a 100 nm thick low stress silicon nitride membrane. The window was 5

mm in square. The HSQ of 3.6% wt., made by diluting the manufacturer's 18% wt. HSQ with semiconductor grade MIBK from Dow Corning (Midland, MI), was spin-coated on the wafer at a speed of 4500 rpm for 45 seconds. The wafer was baked in oven at 170 °C for 30 minutes, yielding a 40 nm thick HSQ layer. The line patterns were written to the wafer using 100 keV electrons and a beam current of 0.5 nA. After the exposure, the wafer was developed in 2.38% wt. tetramethyl ammonia hydroxide (LDD-26W from Rohm and Haas Electronic Materials, Marlborough, MA) for 2 minutes at room temperature. The wafer was rinsed in ultra pure de-ionized water and blow-dried. The final patterns were formed by electroplating in gold to the resist full thickness, using the standard plating process [section B.1.2]. The HSQ resist was then removed by wet etching in 40:1 buffered hydrofluoric acid for a few seconds.

References

1. J. Fujita, Y. Ohnishi, Y. Ochiai and S. Matsui, "Ultrahigh Resolution of Calixarene Negative Resist in Electron Beam Lithography," *Appl. Phys. Lett.* **68** 1297-1299 (1996).
2. D. C. Joy, "The spatial resolution limit of electron lithography," *Microelectron. Eng.* **1**, 103-119 (1983).
3. H. Namatsu, T. Yamaguchi, M. Nagase, K. Yamazaki and K. Kurihara, "Nano-Patterning of a Hydrogen Silsesquioxane Resist with Reduced Linewidth Fluctuations," *Microelectron. Eng.* **42** 331-334 (1998).
4. H. Namatsu, Y. Takahashi, K. Yamazaki, T. Yamaguchi, M. Nagase and K. Kurihara, "Three-Dimensional Siloxane Resist for the Formation of Nanopatterns with Minimum Linewidth Fluctuations," *J VAC SCI TECHNOL B* **16** 69-76 (1998).
5. B. E. Maile, W. Henschel, H. Kurz, B. Rienks, R. Polman and P. Kaars, "Sub-10 nm Linewidth and Overlay Performance Achieved with a Fine-Tuned EBPg-5000 TFE Electron Beam Lithography System," *Jpn. J. Appl. Phys* **39** 6836-6842 (2000).
6. E. H. Anderson, D. Ha, J. A. Liddle, *Microelectron. Eng.* **73-74**, 74 (2004).
7. D. R. Medeiros, A. Aviram, C. R. Guarnieri, W. S. Huang, R. Kwong, C. K. Magg, A. P. Mahorowala, W. M. Moreau, K. E. Petrillo and M. Angelopoulos, "Recent Progress in Electron-Beam Resists for Advanced Mask-Making," *IBM J. Res. Dev.* **45**, 639-650 (2001).
8. D. L. Olynick, B. D. Harteneck, E. Veklerov, M. Tendulkar, J. A. Liddle, A. L. D. Kilcoyne and T. Tyliczszak, "25 Nm Mechanically Buttressed High Aspect Ratio Zone Plates: Fabrication and Performance," *J. Vac. Sci. Technol. B* **22**, 3186-3190 (2004).

Appendix C

Knife Edge Intensity Ranges for Resolution Measurement

Table C-1 lists the intensity variation ranges that give the distances corresponding to the resolution for the same σ value. Similar to table 4-1, the calculation was obtained for a 25 nm micro zone plate and 2.4 nm wavelength, using the computer program SPLAT¹. The calculation assumes a condenser central stop of diameter half of that of the condenser zone plate ($\varepsilon = 0.5$).

$\Delta r_{MZP} = 25 \text{ nm}, \lambda = 2.4 \text{ nm}, \varepsilon = 0.5$		
σ	Intensity range for knife edge object	Resolution defined by equal lines and spaces (nm)
0.0	2% to 98%	25
0.1	4% to 96%	23
0.2	6% to 94%	21
0.3	7% to 93%	20
0.4	10% to 90%	19
0.5	12% to 88%	18
0.6	15% to 85%	17
0.7	18% to 82%	16
0.8	21% to 79%	15
0.9	25% to 75%	15
1.0	30% to 70%	14

References

1. K. K. H. Toh and A. R. Neureuther, "Identifying and Monitoring Effects of Lens Aberrations in Projection Printing," in *Optical Microlithography VI*, H. L. Stover Ed., Proc. SPIE **772**, pp. 202-209.